Hybrid Interface Conditions for Partitioned Fluid–Structure Interaction Simulations

Tao He

Department of Civil Engineering
University of Birmingham

This dissertation is submitted for the degree of
Doctor of Philosophy

01/03/2018

Dedicate to My Parents,

Whose Bounties Are as Boundless as Sea,

and to My Wife, Y. Ren, and My Daughter, Irene,

for the Love and Support They Gave to Me.

Acknowledgements

The author would like to express his most sincere gratitude to both Prof. C. Baniotopoulos and Dr. J. Yang who supervised this study for their patient guidance and valuable time. It has been a great privilege to work under tutelage of such accomplished academics and kind gentlemen.

The author is highly grateful to the funding of the PGTA studentship and the support from the staff at School of Engineering, University of Birmingham. He also acknowledges his friends across the UK and China for their friendship and support. A special thanks are given to Prof. Zhihong Zhang, Prof. Yuxin Zhang and Dr. Tong Wang for their constant encouragement and support.

Finally, the deepest gratitude goes to his family. Their permanent love and trust have been the sustenance throughout. God bless you!

Abstract

This thesis proposes new hybrid interface conditions, based upon the combined interface boundary condition (CIBC) method, to calculate fluid–structure interaction (FSI) within arbitrary Lagrangian–Eulerian finite element framework. Firstly, theoretical bases of physical media and moving mesh scheme are described in Chapters $2 \sim 4$, respectively. The interface coupling conditions, which constitute the key ingredient of FSI, are deliberately analyzed in Chapter 5.

The CIBC method transforms the traditional interface conditions to the incremental corrections for both velocity and traction. To this end, a coupling parameter is employed to adjust such interfacial corrections. The method is hence deemed to better represent the continual reciprocity among different media. Nevertheless, the constrained applications of the CIBC method are realized after recalling its recent development. The derivation of relevant CIBC formulae are thoroughly presented then, providing the foundation of two improved schemes. The resulting improvements and extensions are established below: (i) the method is re-formulated for the general situation based upon the full-form fluid stress tensor; (ii) the rate of structural traction, which incurs the inconsistency in interfacial traction and possibly engenders the accuracy loss, is completely eliminated by a simple treatment; (iii) the instability source is analyzed because of the CIBC compensation and a new approach is proposed to retrieve the interface corrections for different variables; (iv) the method is generalized to a rigid body motion experiencing both translation and rotation. In addition, more details of the improved CIBC method, such as the computational sequence, weak enforcement and arrange of the free parameter, are discussed for the sake of better understanding and easier implementation.

Subsequently, the two improved CIBC methods are introduced into different partitioned solution schemes involving explicit, implicit and semi-implicit coupling strategies. Detail of these coupling algorithms are thoroughly interpret in Chapter 6. After illustrating all ingredients of the coupled FSI system, I have tested massive FSI problems so as to highlight the robustness, efficiency and feasibility of the developed methodologies in Chapter 7.

Both rigid and flexible bodies with various geometries and different degrees of freedom are investigated. The well-known vortex-induced oscillation phenomena are accurately captured, such as beating, lock-on, galloping and flutter. In particular, two important indicators, Reynolds number and mass ratio, are analyzed in detail for several problems to reveal the mechanism of flow-induced dynamics. Some conclusions and perspectives are provided in the final chapter.

Table of contents

List of figures

List of tables

Chapter 1

Introduction

1.1 Background

Fluid–structure interaction (abbr. FSI) depicts the everlasting interplay of a fluid and a body immersed within the fluid through their interface. FSI is frequently encountered in the majority of practical applications such as mechanical, civil, biomedical ocean and aerospace engineering [1, 2]. For example, civil engineering has witnessed the strong wind over a suspension bridge or a high-rise building while the marine risers are invariably stimulated by ocean currents to dramatically vibrate in ocean engineering. The action of "blowing up a balloon" is another such FSI example. Once one of natural frequencies of an engineering structure approaches to the vortex-shedding counterpart, strongly self-excited structural oscillations may be triggered under the action of FSI. Ignoring the FSI effect could be catastrophic, especially to those structures built upon the materials susceptible to fatigue. In the 1940s, the collapse of Tacoma Narrows Bridge seems the most notorious large-scale failure. Turbine blades and aircraft wings can break thanks to severe flow-induced oscillations. FSI must be considered to analyze the aneurysms in artificial heart valves and large arteries. Therefore, the FSI effect is probably a crucial consideration in designing these engineering systems experiencing violent flow-induced vibrations. Accurately predicting FSI probably helps us to find the working mechanism, and then to alleviate or suppress these adverse effects through some special countermeasures. Given its practical significance, FSI nowadays have received growing interests from the research community.

As one of representative branches of multiphysical phenomena, FSI characterizes the continuous interplay between a moving body and a surrounding fluid. This mixed interaction involves that the fluctuating fluid force acts on the structure whose movement in turn

alters the flow patterns nearby. That is to say, any changes of one physical field will stimulate the response of the other and *vice verse*. The data exchanges among all interacting fields take place along the fluid–structure interface continuously. For this reason, the strong nonlinearity, as well as the high uncertainty, is recognized from both the fluid and global systems. To be specific, the governing equations for two completely different media have distinctive natures, and, most importantly, additional boundary conditions are introduced into each individual field. The complexity will be further aggravated if structural nonlinearities are considered. Generally, the analytical solution of FSI remains nearly unavailable except for some extremely simplified situations. The development of individual disciplines and computer technology since last decades makes possible the numerical solution of realistic FSI. Accordingly, FSI researches have long promoted improvements and interchanges across different disciplines.

1.2 Classification of coupling algorithms

For years, FSI has been the challenging topic in multi-physical simulation because FSI involves both complicated mathematical principles and rich physical essences. From perspective of fundamentals, CFD (computational fluid dynamics), structural mechanics and mesh deformation are the three ingredients of FSI [3]; that is to say, FSI is governed via the three-field nonlinear formulation [4]. A number of articles comprehensively review FSI solution techniques [5–11]. This thesis will exclusively focuses on the numerical methods using the arbitrary Lagrangian–Eulerian (ALE) description [12].

Numerical methodologies for solving an FSI problem are largely grouped into two categories: *monolithic methods* [13–15] and *partitioned methods* [16–18]. The former approaches assemble the governing equations of individual fields into a single block, and then iterates the monolithic system until convergent. The excellent energy conservation is thus achieved in the monolithic methods. On the other hand, remarkable efforts are demanded to revise the existing codes, which loses program modularity and entangles mathematical management. It turns out that, numerical expense is a major issue to a monolithic method. By contrast, the partitioned strategics settle all disciplines sequentially. Accordingly, these methods require minimal changes in existing programs and facilitate the combination of different solvers. The above-mentioned merits make the approach an attractive option in practice.

The partitioned coupling methods could date back to the pioneering work [19]. They may be further classified into *explicit* [20–22] and *implicit* schemes [17, 23, 24]. The par-

titioned explicit coupling schemes work in a iteration-free manner, hence achieving both conceptual clarity and computational efficiency. Nevertheless, explicit schemes do not satisfy the physical equilibrium on the interface. Cumulated numerical errors probably lead to a spurious or even divergent solution. As we know, partitioned explicit coupling techniques suffer from the instability initiated from strong added-mass effect [25–27]. Even reducing a time step size cannot cure this trouble. In contrast, partitioned implicit coupling methods are stable because they preserve the energy through inner-iterating all individual fields per time step. These techniques are physically rigorous, and normally do not deteriorate the accuracy of the overall FSI solution. The time consumption is still at a high level, although the efficiency is not affected in aeroelasticity where the oscillating body is much heavier than the fluid [28].

Apart from explicit and implicit coupling algorithms, a third category of solution algorithms, known as the *semi-implicit algorithm*, has been presented over the past decade. A projection semi-implicit coupling scheme is first developed by Fernández *et al.* [18] for simulating strong added-mass FSI problems. The semi-implicit coupling lies in the Chorin–Témam projection [29, 30] which provides a natural treatment for FSI. Particularly, the dynamic mesh is predicted together with the advection-diffusion fluid step, while on the frozen ALE mesh the subiterations are performed between the projection step and structural movement. Theoretical analysis indicated that, the semi-implicit approach achieves the better efficiency and maintains the stability [18]. Many semi-implicit methods have been proposed, following the idea in [18]. On the basis of the algebraic fractional step method, Quaini and Quarteroni [31] proposed another semi-implicit scheme. This method never requires intermediate boundary conditions for each differential subsystem. Then the block-LU factorization was introduced to semi-implicit schemes [32]. The Nitsche- and Robin-based semi-implicit algorithms were proposed for the incompressible fluid interacting with the thin-walled solid [33]. The better stability was achieved therein based on these conditions. In [34] a convergence analysis was carried out for the projection-based scheme [18] using a simplified FSI problems. In the scheme, the error of time discretization was shown as at least $\sqrt{\Delta t}$ which is the time step. A thorough review was presented in [35] for blood flows in large arteries using different schemes. Later, a semi-implicit algorithm was carried out on the ground of a fluid dynamics solver [36, 22, 37]. Extra ordinary differential equations (ODEs) are handled along the predicted interface [36]. Only traditional interface conditions were imposed in [22, 37]. Our research was briefly reviewed in [22], after comparing different coupling schemes. More details are provided in [37] about how to perform the smoothed finite element method (SFEM) within structural component. To secure the fraction-step type, the pressure Poisson equation (PPE) considers the implanted mass

source term (MST) [38] in the interface elements [22, 37, 39, 40] via characteristic-based split (CBS) scheme [41–43]. Note that the MST is calculated from three-node triangular (T3) element.

Other semi-implicit schemes cope with the fluid momentum equation monolithically, rather than employing the classical Chorin–Témam projection splitting [29, 30]. A least squares problem is solved to guaranteed the velocity and stress continuity on the interface, semi-implicitly [44, 45]. The explicit stage only moves the dynamic mesh whereas the fluid and solid solutions are placed in the subiterations. A partitioned predictor-corrector scheme was independently proposed by Breuer *et al.* [46] in order to investigate an FSI benchmark problem. Different from [44, 45], the implicit step repeats the mesh adaptation. Recently, the author [47, 48] made use of the artificial compressibility (AC) method [49] aiming to repair existing shortcomings of semi-implicit scheme. As a result of that, the incompressibility condition is not strictly respected any more.

1.3 Purpose of hybrid interface conditions

The most intractable root of FSI stems from the sophisticated and permanent interplay between distinctly physical fields. Clearly, a sequential partitioned coupling scheme introduces an explicit flavor into FSI computation even through all subsystems are iteratively solved. Therefore, the restriction on time step size has to be anticipated. Nevertheless, previous observations indicate that decreasing the time step will never cure to the increased instability at all. This instability is innate in the partitioned scheme and is known as added mass effect [25–27], because the major contribution of a fluid behaves as the redundant mass onto the structure via the interface. See [50] for example, where the adverse added-mass effect takes place in the flow-induced oscillations of rigid foils. As a matter of course, exploring an effective partitioned algorithm is central for FSI theory.

Jaiman and his co-workers have developed a partitioned solution procedure for simulating FSI since 2007 [51–53]. The method is originally developed for a linearized FSI model [54] considering the characteristic boundary conditions [55] and the transformed interface conditions. Subsequently, this procedure is formally named the combined interface boundary condition (CIBC) method that improves stability and accuracy in certain simple cases via higher-order increments [51, 52]. At two continuous time instants, these corrections are sequentially constructed for velocity and momentum flux for minimizing the instability and damping out the interfacial energy residuals. These corrections are controlled via a constant that plays a central part in the CIBC method. The corrective increments, which combine

the Dirichlet-type conditions with the Neumann-type ones, constitute the hybrid interface conditions. The impetus of the approach lies in inventing a compensation mechanism on the interface while separately computing different fields; in other words, the method is intended to rectify or alleviate the time lag arising from the staggered FSI computation. Furthermore, a potential bonus may be gained from the acceleration for inner-iterations.

1.4 Historical review of the CIBC method

As mentioned earlier, the CIBC method was presented in 2007 [51] where considerable improvements are made to the one-dimensional (1D) piston. The good adaptability is realized via combining the staggered partitioned procedure [16] and the subcycling [56, 57]. Subsequently, the CIBC method was applied into the conjugate heat-transfer process [58], demonstrating that the method results in more accurate and stable results for the explicit method. The optimal parameter is suggested for a wider stability area via the well-known Godunov–Ryabenkii method. One may improve partitioned computation further by furnishing the CIBC method with the simple averaging method [59, 60]. A multi-iterative coupling (MIC) approach was devised in [61] for the CIBC method to estimate the flexible baffle problem and to predict the interaction between turbulent flows and marine riser. The considerably low mass ratio is realized for practical scenarios. However, the numerical details seems very limited. Later on, the Robin transmission conditions were designed for FSI problems [62]. The relevant formulae take on the similarity between the methods in [55, 62] and the CIBC method. Howbeit, the former employs two coupling parameters whereas the latter only one. In short, the application the CIBC method to a simple FSI model reveals the desirable superiority. Despite that, careful considerations are required for 2/3D problems [52]. Recently, the nonlinear iterative force correction (NIFC) method [63] was proposed to extend the above MIC scheme, where the CIBC method works as the predictor. Real-world computations of marine risers are handled at low mass ratios. Then the NIFC method is described in [64] according to the Aitken extrapolation [65–67] to stabilize the coupled system. The mass ratio has been studied for a flexible cylinder to highlight the merits. For the time being, the CIBC method has found itself in incomplete FSI problems. A few defects are summarized below

- The CIBC method is established by the fluid stress $\boldsymbol{\sigma}^{\mathrm{F}} = p\mathbf{I}$ where p is the pressure and $\mathbf{I}$ represents the identity tensor;
- The rate of structural traction is not eliminated prior to updating the traction;
- The fluid–rigid body computation is impossible;

- The displacement continuity is not preserved.

To date, several studies have been conducted to boost the CIBC method. To be specific, the method has been extended to a rigid or flexible body interacting with an incompressible fluid. The improvements are briefly recalled in the following. A new CIBC formulation is proposed in [68] in which the uncorrected traction was dropped. For this reason, the improved method succeeds in rescuing the fluid–rigid body simulation. As a matter of course, the CIBC method is used for partitioned subiterative coupling schemes in areoelastic simulations [36]. However, the displacement predictor [57] incurs lagged variables [69]. Instead, the force predictor [70, 71] may be considered. The latest subdomains are hence generated for the method [69]. The methodologies have been justified by oscillating bluff bodies under laminar flow region [68, 36, 69]. It is emphasized that, the improved CIBC corrections [68, 36, 69] have been recently introduced into the NIFC procedure [72] for freely vibrating cylinders at subcritical Reynolds number, as the first effort devoted to the complex simulation. Therefore, the proposed scheme takes into consideration the turbulence where light offshore structures oscillate violently. Inspired by [18], a new semi-implicit coupling technique has been presented where the CBS subsolver is responsible for the global system as well [40]. The CIBC method is totally re-derived in order to interpret the reciprocity between both physical media. No additional equations to rectify the traction appear on the interface. Only the interface displacement is corrected for stability, in a weak manner. The correction for traction is introduced into the finite element weak formulation whereas the velocity correction is simplified properly, when dealing with the elastic solid. The improved method is suitable to both fluid–rigid/–flexible structure interaction, and fixes those limitations of its original counterpart. The CIBC method is recoined in consideration of the complete fluid stress [39]. The instability source is well analyzed for the CIBC compensation, meanwhile an approach is proposed to restore two-sided corrections. Particularly, the present CIBC method implicitly corrects the pitching moment for rigid–body torsion. The generalized inverse matrix theory is used to support the current proof. The reader is referred to the review article concerning the enhanced hybrid interface condition [1].

1.5 Scopes and objectives

According to [73], the coupled FSI system is mainly classified into two categories

- Class I contains the problems where the interplay occurs on interfaces via the imposed coupling conditions.

- Class II comprises the problems where the interplay emanates from different physical media within (partially or totally) overlapping domains.

The major concern will be to propose partitioned coupling algorithms for Class I and to study the resulting flow-induced phenomena, in particular for the oscillating single bluff body. In addition, only planar, laminar cases are take into account.

Numerical methods applied to the first class of FSI problems need to resolve a group of discretized partial differential equations (PDEs) which involve nodal variables located within different domains. To this end, the present thesis is devoted to the following aspects

- The solutions to all interacting fields may be improved to facilitate the partitioned FSI algorithms.
- Efficient and stable partitioned coupling algorithms are developed based upon the hybrid interface conditions.
- Numerical examples with increasing difficulty are addressed to demonstrate the performance of the present methodologies.
- In-house FORTRAN codes are developed for the current topic as well as potential extension.

The research findings are expected to be beneficial to various disciplines such as mechanical, civil, ocean and aerospace engineering, and are of academic significance to progress knowledge and solution in FSI as well. Basically, no conceptual difficulties exist in applying the developed strategies into three-dimensional problems, though the current applications are restricted to the two-dimensional configurations.

Chapter 2

Fluid subproblem

2.1 Governing equations

$\Omega^{\mathrm{f}} \subset \mathbb{R}^2$ is the fluid domain and $(0,\ T)$ the temporal one. Γ^{f} represents the boundary of Ω^{f}, indicating that the Dirichlet segment $\Gamma^{\mathrm{f}}_{\mathrm{d}}$, the Neumann segment $\Gamma^{\mathrm{f}}_{\mathrm{n}}$ and the interface Σ are complementary subsets. t and $\mathbf{x}$ denote temporal and spatial coordinates, respectively. The incompressible Navier–Stokes (NS) equations with deforming boundaries may be written under the ALE description [1]

$$\nabla \cdot \mathbf{u} = 0 \quad \text{on} \quad \Omega^{\mathrm{f}} \times (0,\ T), \tag{2.1}$$

$$\rho^{\mathrm{f}} \left(\frac{\partial \mathbf{u}}{\partial t} + \mathbf{c} \cdot \nabla \mathbf{u} - \mathbf{f}^{\mathrm{f}} \right) - \nabla \cdot \boldsymbol{\sigma}^{\mathrm{f}} = \mathbf{0} \quad \text{on} \quad \Omega^{\mathrm{f}} \times (0,\ T), \tag{2.2}$$

where ρ^{f} means the fluid density, $\mathbf{u}$ denotes the fluid velocity, p designates the pressure, the convective velocity $\mathbf{c} = \mathbf{u} - \mathbf{w}$, $\mathbf{w}$ designates the mesh velocity, $\mathbf{f}^{\mathrm{f}}$ means the body force, $\boldsymbol{\sigma}^{\mathrm{f}}$ represents the fluid stress and ∇ is the gradient operator.

The constitutive model describing a Newtonian fluid reads

$$\boldsymbol{\sigma}^{\mathrm{f}} = -p\mathbf{I} + 2\mu\boldsymbol{\varepsilon} \quad \text{and} \quad \boldsymbol{\varepsilon} = \frac{1}{2}\left(\nabla \mathbf{u} + (\nabla \mathbf{u})^{\mathrm{T}}\right), \tag{2.3}$$

where μ represents the fluid viscosity, $\boldsymbol{\varepsilon}$ is the strain rate, superscript T denotes transpose and $\mathbf{I}$ stands for identity tensor.

Necessary conditions are prescribed to the boundaries and initial state

$$\mathbf{u} = \mathbf{g}^{\mathrm{f}} \quad \text{on} \quad \Gamma_{\mathrm{d}}^{\mathrm{f}}, \tag{2.4a}$$

$$\mathbf{t}^{\mathrm{f}} = \boldsymbol{\sigma}^{\mathrm{f}} \cdot \mathbf{n}^{\mathrm{f}} = \mathbf{h}^{\mathrm{f}} \quad \text{on} \quad \Gamma_{\mathrm{n}}^{\mathrm{f}}, \tag{2.4b}$$

$$\mathbf{u}(\mathbf{x},\, 0) = \mathbf{u}^0,\; p(\mathbf{x},\, 0) = p^0 \quad \text{on} \quad \Omega_0^{\mathrm{f}}, \tag{2.4c}$$

where $\mathbf{t}^{\mathrm{f}}$ is the traction while $\mathbf{n}^{\mathrm{f}}$ denotes the outward normal.

The dimensionless scales

$$\hat{\mathbf{x}} = \frac{\mathbf{x}}{D},\; \hat{t} = \frac{tU}{D},\; \hat{\mathbf{u}} = \frac{\mathbf{u}}{U},\; \hat{\mathbf{c}} = \frac{\mathbf{c}}{U},\; \hat{p} = \frac{p}{\rho^{\mathrm{f}} U^2},\; \hat{\mathbf{f}}^{\mathrm{f}} = \frac{\mathbf{f}^{\mathrm{f}} D}{U^2}$$

are defined in association with the characteristic length D and characteristic velocity U. Dropping all hats over these scales, the dimensionless NS equations is written below

$$\nabla \cdot \mathbf{u} = 0 \quad \text{on} \quad \Omega^{\mathrm{f}} \times (0,\, T), \tag{2.5}$$

$$\frac{\partial \mathbf{u}}{\partial t} + \mathbf{c} \cdot \nabla \mathbf{u} - \nabla \cdot \boldsymbol{\sigma}^{\mathrm{f}} - \mathbf{f}^{\mathrm{f}} = \mathbf{0} \quad \text{on} \quad \Omega^{\mathrm{f}} \times (0,\, T), \tag{2.6}$$

in tandem with the constitutive relation

$$\boldsymbol{\sigma}^{\mathrm{f}} = -p\mathbf{I} + \frac{1}{Re}\left(\nabla \mathbf{u} + (\nabla \mathbf{u})^{\mathrm{T}}\right), \tag{2.7}$$

where the Reynolds number $Re = \rho^{\mathrm{f}} UD/\mu$. Eqs. (2.4a)–(2.4c) are nondimensionalized as well [74].

2.2 CBS scheme

2.2.1 CBS scheme for moving-mesh problems

A general fluid mechanics algorithm has been developed by Zienkiewicz *et al.* [41–43] since 1995. This method was called the CBS scheme [75] formally in 1999. The CBS scheme relates the characteristic Galerkin technique [76] to the projection method [29, 30]. The former will suppress the spurious oscillations through a higher-order time stepping for convection-dominated cases, whereas the latter is about to stabilize the pressure [77].

In the past decade, the CBS scheme has succeeded in addressing moving mesh problems. Nithiarasu [78] first solved free-surface flow using the ALE finite element formulation. Later, numerous studies have emerged in consideration of various coupling schemes. For example, the CBS scheme was adopted for the in-line forced-motion simulation of a circular cylinder [79], the free-surface computation [80], and analysis of the flow–airfoil interaction [81]. The difference between [78] and [79–81] mainly lies in the AC scheme [78] and the incompressible scheme [79–81]. For the moment, the incompressible CBS scheme enjoys the major popularity in FSI.

A series of researches have been performed with the help of the incompressible CBS scheme [36, 22, 37, 68, 82–84]. In general, computed results agree with existing data well and flow-induced phenomena are successfully captured. The explicit and subiterative schemes [68, 36, 82] are implemented to analyze vortex-induced vibrations (VIV) of a vibrating cylinder, where displacement or force of the body can be predicted. The dual time steps [85] are also discussed on FSI in [36]. Unfortunately, this technique would degenerate the results in aeroelasticity. Preliminary simulations were performed for an elastic solid excited by an incompressible fluid [22, 82, 83]. The MST [38] was embedded into the CBS method so as to respect geometric conservation law (GCL) which is hardly met by the so-called fractional-step approaches. An improved CBS scheme [86] was proposed to tackle four flexible cylinders excited by incompressible fluid flows [84].

The CBS scheme can also work together with other methods. The iterative CBS scheme [87] formulated in the finite element method (FEM) is proposed for simulating non-Newtonian fluid flows incorporating element-free Galerkin method. The latter may be combined with the CBS technique for simulating free-surface flows [88]. Later, the immersed smoothed FEM adopts the CBS scheme to handle the incompressible fluid–deformable solid interaction in 2D [89].

2.2.2 Solution procedure

Eqs. (2.6)–(2.7) are solved with the aid of the CBS scheme below. The imposition of boundary conditions is equal to [90].

Step 1: Predict the velocity

$$\mathbf{u}^* - \mathbf{u}^n = \Delta t \left(-\mathbf{c}^n \cdot \nabla \mathbf{u}^n + \frac{1}{Re} \nabla^2 \mathbf{u}^n + \frac{\Delta t}{2} \mathbf{c}^n \cdot \nabla (\mathbf{c}^n \cdot \nabla \mathbf{u}^n) \right), \tag{2.8}$$

Step 2: Update the pressure

$$\nabla^2 p^{n+1} = \frac{1}{\Delta t}\nabla \cdot \mathbf{u}^*, \tag{2.9}$$

Step 3: Correct the velocity

$$\mathbf{u}^{n+1} - \mathbf{u}^* = -\Delta t \left(\nabla p^{n+1} - \frac{\Delta t}{2}\mathbf{c}^n \cdot \nabla^2 p^n \right), \tag{2.10}$$

where $\mathbf{f}^{\mathrm{f}}$ is ignored.

In the scheme, computational savings can be gained on a moving mesh since $(\Delta t)^2/2$ has nothing to do with the local element size as the stabilizing parameter. Codina et al. [91] interpreted the time step as the stabilizing parameter. Moreover, Nithiarasu and Zienkiewicz [85, 92] implied that dual time steps might be good for FSI calculations. The impact of dual time steps on an oscillating bluff body will be discussed in the future section. The comprehensive derivation of the scheme, as well as its versatile applications, are provided in the textbook [93] in reference to the CBS scheme. The latest CBS review is probably presented by Nithiarasu et al. [94], whereas a comparative study is found in [95] to discuss different versions of the CBS scheme as well as their performance in incompressible flows. In addition, the CBS scheme is able to work in a matrix-free manner if the AC method is embodied [96, 92].

2.2.3 Stability condition

Since the CBS scheme is of conditional stability [93], the stability limitations for the permissible time step are stated as [93]

$$\Delta t \leqslant \min(\Delta t_{\mathrm{conv}},\ \Delta t_{\mathrm{diff}}), \tag{2.11}$$

$$\Delta t_{\mathrm{conv}} = \frac{h}{|\mathbf{u}|} \quad \text{and} \quad \Delta t_{\mathrm{diff}} = \frac{1}{2} Re h^2, \tag{2.12}$$

where Δt_{conv} denotes the convective time step while Δt_{diff} the diffusive one, and h is the local element size.

2.3 Spatial discretization

The FE discretization is conducted for the fluid problem [97]. Since within the scheme velocity and pressure admits equal- and low-order interpolation, the two quantities are represented by the shape function **N**

$$\mathbf{u} = \mathbf{N}\underline{\mathbf{u}},\ p = \mathbf{N}\underline{\mathbf{p}}. \tag{2.13}$$

Substitution of this approximation into Eqs. (2.8)–(2.10) leads to the final matrix form

$$\mathbf{M}^{\mathrm{f}}(\underline{\mathbf{u}}^{*} - \underline{\mathbf{u}}^{n}) = -\Delta t \left(\mathbf{C}_{\mathrm{u}}^{n}\underline{\mathbf{u}}^{n} + \widetilde{\mathbf{K}}_{\tau}\underline{\mathbf{u}}^{n} + \frac{\Delta t}{2}\mathbf{K}_{\mathrm{u}}^{n}\underline{\mathbf{u}}^{n} - \mathbf{f}_{\mathrm{u}}^{n} \right), \tag{2.14}$$

$$\widetilde{\mathbf{H}}\underline{\mathbf{p}}^{n+1} = -\frac{1}{\Delta t}\mathbf{G}\underline{\mathbf{u}}^{*} + \mathbf{f}_{\mathrm{p}}^{n+1}, \tag{2.15}$$

$$\mathbf{M}^{\mathrm{f}}(\underline{\mathbf{u}}^{n+1} - \underline{\mathbf{u}}^{*}) = -\Delta t \left(\mathbf{G}^{\mathrm{T}}\underline{\mathbf{p}}^{n+1} + \frac{\Delta t}{2}\mathbf{Q}^{n}\underline{\mathbf{p}}^{n} + \check{\mathbf{f}}_{\mathrm{p}}^{n} \right), \tag{2.16}$$

where the matrices and vectors are given by

$$\mathbf{M}^{\mathrm{f}} = \int_{\Omega^{\mathrm{f}}} \mathbf{N}^{\mathrm{T}}\mathbf{N}\mathrm{d}\Omega,\ \mathbf{C}_{\mathrm{u}}^{n} = \int_{\Omega^{\mathrm{f}}} \mathbf{N}^{\mathrm{T}}(\nabla^{\mathrm{T}}\mathbf{c}^{n}\mathbf{N})\mathrm{d}\Omega,\ \mathbf{K}_{\mathrm{u}}^{n} = \int_{\Omega^{\mathrm{f}}} (\nabla^{\mathrm{T}}\mathbf{c}^{n}\mathbf{N})^{\mathrm{T}}(\nabla^{\mathrm{T}}\mathbf{c}^{n}\mathbf{N})\mathrm{d}\Omega,$$

$$\mathbf{G} = \int_{\Omega^{\mathrm{f}}} (\nabla\mathbf{N})^{\mathrm{T}}\mathbf{N}\mathrm{d}\Omega,\ \mathbf{Q}^{n} = \int_{\Omega^{\mathrm{f}}} (\nabla^{\mathrm{T}}\mathbf{c}^{n}\mathbf{N})^{\mathrm{T}}(\nabla\mathbf{N})\mathrm{d}\Omega,\ \check{\mathbf{f}}_{\mathrm{p}}^{n} = \int_{\Gamma^{\mathrm{f}}} \mathbf{N}^{\mathrm{T}}(\mathbf{n}^{\mathrm{T}}\mathbf{c}^{n})\nabla p^{n}\mathrm{d}\Gamma,$$

$$\mathbf{f}_{\mathrm{u}}^{n} = \frac{1}{Re}\int_{\Gamma^{\mathrm{f}}} \mathbf{N}^{\mathrm{T}}\mathbf{n}^{\mathrm{T}}(\nabla^{\mathrm{T}}\mathbf{u}^{n})\mathrm{d}\Gamma + \int_{\Gamma^{\mathrm{f}}} \mathbf{N}^{\mathrm{T}}(\mathbf{n}^{\mathrm{T}}\mathbf{c}^{n})(\nabla^{\mathrm{T}}\mathbf{c}^{n}\mathbf{u}^{n})\mathrm{d}\Gamma,\ \mathbf{f}_{\mathrm{p}}^{n+1} = \int_{\Gamma^{\mathrm{f}}} \mathbf{N}^{\mathrm{T}}(\mathbf{n}^{\mathrm{T}}\nabla p^{n+1})\mathrm{d}\Gamma,$$

$$\mathbf{K}_{\tau} = \frac{1}{Re}\int_{\Omega^{\mathrm{f}}} (\nabla\mathbf{N})^{\mathrm{T}}(\nabla\mathbf{N})\mathrm{d}\Omega,\ \mathbf{H} = \int_{\Omega^{\mathrm{f}}} (\nabla\mathbf{N})^{\mathrm{T}}(\nabla\mathbf{N})\mathrm{d}\Omega.$$

The lumped mass matrix achieves a good compromise between accuracy and efficiency, thus causing no significant errors [75]. Either linear T3 element or bilinear four-node quadrilateral (Q4) element is adopted to discretize the above equations in space [97].

2.4 Validation

2.4.1 Flows past a circular cylinder

The problem settings are given by Fig. 2.1. In Fig. 2.2 the mesh resolution is assessed via M1 (4213 points and 8216 T3 elements), M2 (8144 points and 16058 T3 elements) and M3 (16341 points and 32343 T3 elements) [68]. The time step is chosen through computer experiments according to [36].

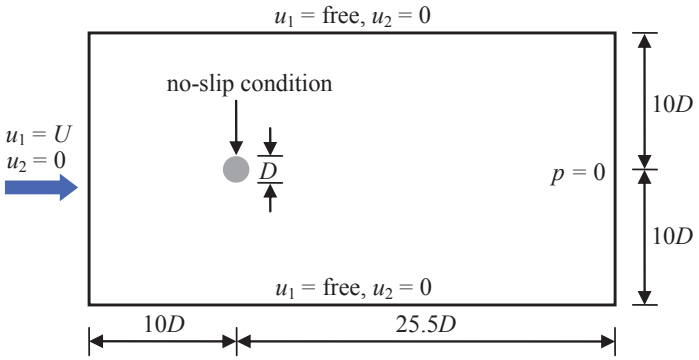

Fig. 2.1 Problem description of flow past a circular cylinder

Fig. 2.3 displays the *St*–*Re* function under laminar flows. Here $St = f_v D/U$ is obtained based upon the vortex-shedding frequency f_v. In this figure other *St*–*Re* functions [98–103] and experimental data [104] are displayed for comparison. In Fig. 2.3 the three sets of data agree with those existing ones.

Table 2.1 lists the calculated parameters at $Re = 100$ containing $C_{d,mean}$, $C_{d,rms}$, $C_{l,max}$, $C_{l,rms}$ and St. In Table 2.1, the difference between this thesis and previous papers [105, 103, 106–110] are reasonably small and the present fluid solver is insensitive to the mesh resolution.

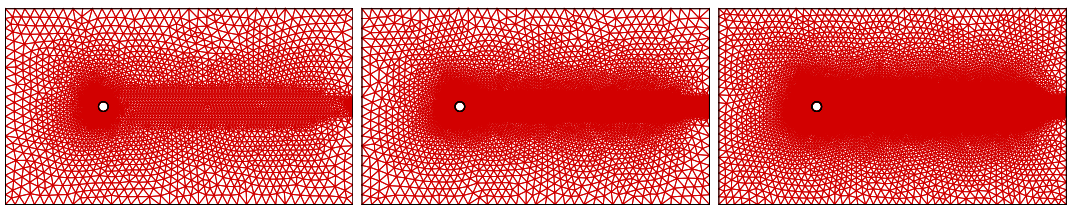

(a) Mesh 1 **(b)** Mesh 2 **(c)** Mesh 3

Fig. 2.2 Finite element meshes

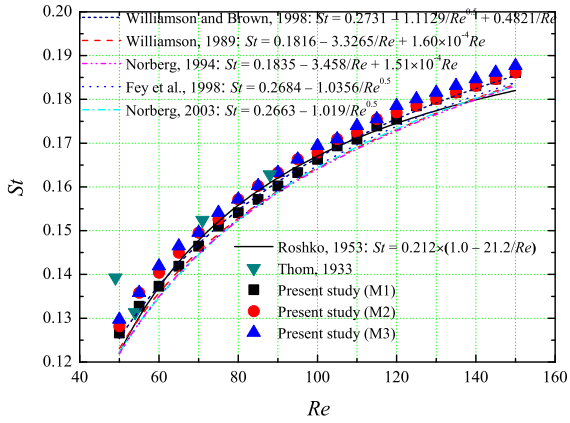

Fig. 2.3 *St*–*Re* relationship for the circular cylinder

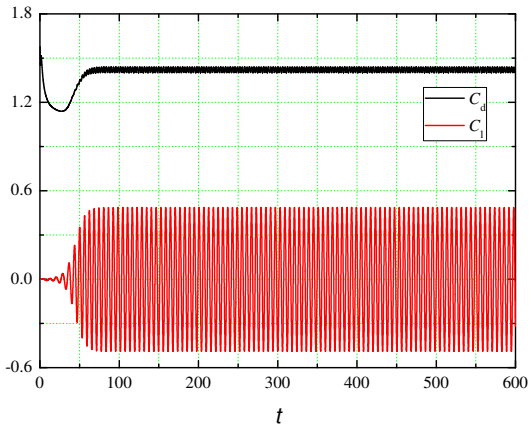

Fig. 2.4 Time history of force coefficients at $Re = 100$

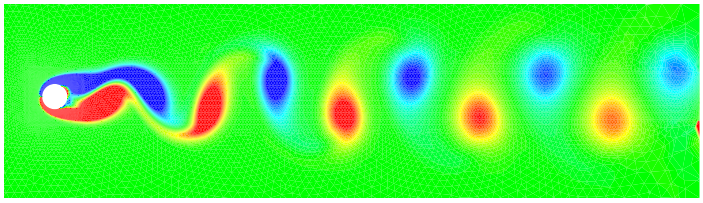

Fig. 2.5 Vorticity contour at $Re = 100$

Table 2.1 Comparison between published and present data

Reference	$C_{d,mean}$	$C_{d,rms}$	$C_{l,max}$	$C_{l,rms}$	St
Wieselsberger [105]	1.44	–	–	–	–
Norberg [103]	–	–	0.32	–	0.164
Gushchin [106, 107]	1.38	0.04038	–	–	–
Arkell and Graham [106, 107]	1.33	0.01514	–	0.17	–
Karniadakis [106, 107]	1.42	0.00504	–	0.26	–
Chaplin [106, 107]	1.29	0.00379	–	0.20	–
Anagnostopoulos [108]	1.20	–	0.27	–	0.167
Zhou et al. [109]	1.476	–	0.31	0.219	0.162
Bahmani and Akbari [110]	1.33	–	0.33	–	0.165
Present study (M1)	1.421	0.01368	0.489	0.344	0.166
Present study (M2)	1.373	0.00829	0.375	0.265	0.168
Present study (M3)	1.377	0.00757	0.355	0.251	0.169

The current simulations indicate that the developed code is quite adequate. The time history is displayed in Fig. 2.4 for drag and lift coefficients at $Re = 100$. The stable and periodic curves imply the regulate vortex shedding behind the wake. Fig. 2.5 plots the vorticity contour at $Re = 100$, representing the repeating swirling vortices. The Kármán vortex street is clearly seen in the wake.

2.4.2 Flows past a square cylinder

Low Re flows over a square cylinder in Fig. 2.6 are numerically calculated. The mesh independence is evaluated via M1 (4204 points and 8218 T3 elements), M2 (8365 points and 16520 T3 elements) and M3 (16741 points and 33120 T3 elements) [68] in Fig. 2.7.

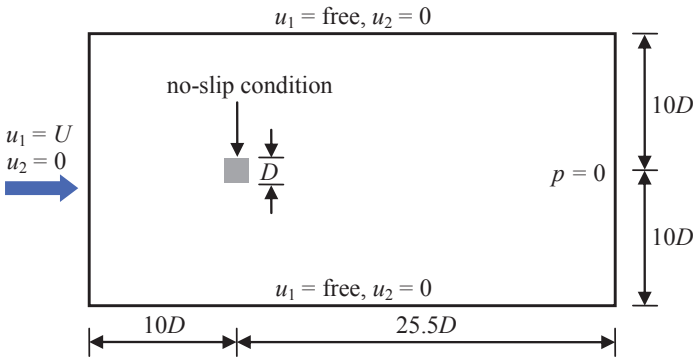

Fig. 2.6 Problem description of flow past a square cylinder

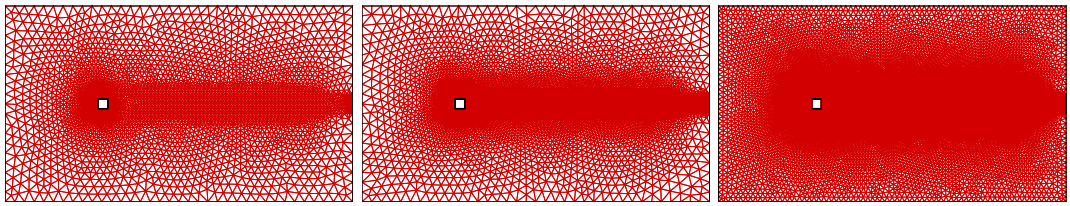

(a) Mesh 1 **(b)** Mesh 2 **(c)** Mesh 3

Fig. 2.7 Finite element meshes

Fig. 2.8 describes the *St*–*Re* function for the cylinder. The previous results [111–115] and the fitting graph [116] are also contained in the figure for comparison. The results obtained from all three meshes agree with both the data [112] and the fitted relation [116]. However, the magnitude of [115] is slightly larger while the rest are smaller. Given different approach and meshes people have adopted, the present data seem reasonable and the developed code is reasonably accurate.

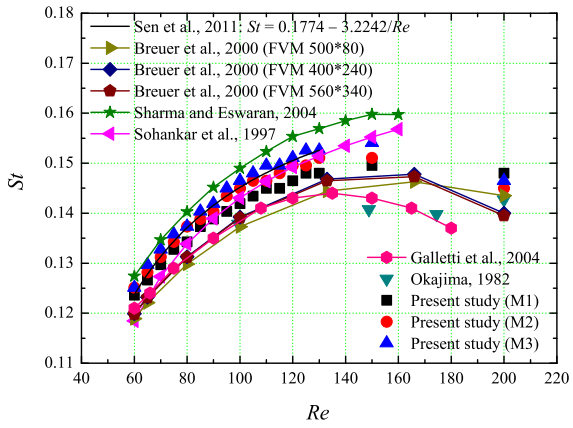

Fig. 2.8 *St*–*Re* relationship for the square cylinder

Table 2.2 summaries the parameters at $Re = 100$. The obtained data exhibit a reasonable agreement with the available results [111–113, 115, 116] in the table. Therefore, the code is accurate for further simulations.

Fig. 2.9 plots the stable time evolution of force coefficients at $Re = 100$. The vorticity contour at $Re = 100$ is displayed in Fig. 2.10. It is observed that behind the wake is the 2S mode [117]. Hence M1 may be a good choice for FSI calculations presented later.

Table 2.2 Comparison between published and present data

Reference	$C_{\mathrm{d,mean}}$	$C_{\mathrm{d,rms}}$	$C_{\mathrm{l,max}}$	$C_{\mathrm{l,rms}}$	St
Okajima [111]	1.60	–	–	–	0.135–0.140
Sohankar et al. [112]	1.464–1.477	–	–	0.138–0.156	0.146–0.147
Breuer et al. [113]	1.351–1.381	–	–	–	0.137–0.139
Sharma and Eswaran [115]	1.4936	0.0054	–	0.1922	0.1488
Sen et al. [116]	1.5287	0.0055	–	0.1928	0.1452
Present study (M1)	1.620	0.01112	0.377	0.266	0.14191
Present study (M2)	1.586	0.00732	0.306	0.215	0.14496
Present study (M3)	1.566	0.00675	0.294	0.207	0.14648

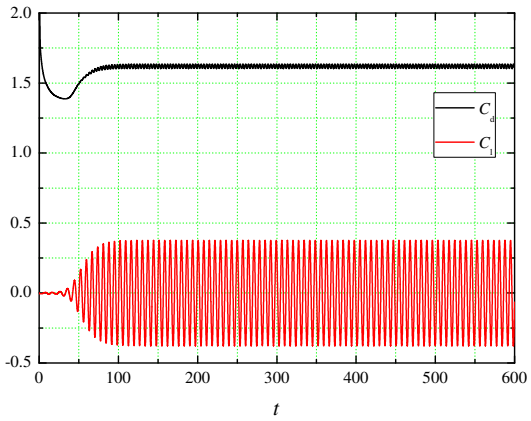

Fig. 2.9 Time history of force coefficients at $Re = 100$

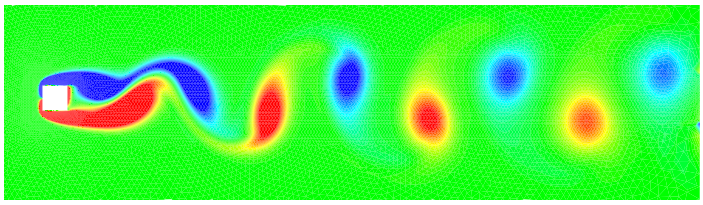

Fig. 2.10 Vorticity contour at $Re = 100$

Chapter 3

Structural subproblem

A structural domain is denoted by $\Omega^{\mathrm{s}} \subset \mathbb{R}^2$ and the domain boundary $\Gamma^{\mathrm{s}} = \Gamma^{\mathrm{s}}_{\mathrm{d}} \cup \Gamma^{\mathrm{s}}_{\mathrm{n}} \cup \Sigma$. The structural equations are formulated under the Lagrangian description.

3.1 Rigid–body motions

A rigid structure immerged into an incompressible fluid can be viewed to be a system of mass-spring-damper. The body goes through translation and rotation in Fig. 3.1. Its displacement in horizontal, vertical and rotational directions is represented by $\mathbf{d} = \{d_1,\ d_2,\ \theta\}^{\mathrm{T}}$. The equation of such a rigid–body motion reads [1]

$$\begin{bmatrix} m_1 & & \\ & m_2 & \\ & & m_\theta \end{bmatrix} \ddot{\mathbf{d}} + \begin{bmatrix} c_1 & & \\ & c_2 & \\ & & c_\theta \end{bmatrix} \dot{\mathbf{d}} + \begin{bmatrix} k_1 & & \\ & k_2 & \\ & & k_\theta \end{bmatrix} \mathbf{d} = \mathbf{R}, \tag{3.1}$$

where m_i, c_i and k_i illuminates the mass, damping and stiffness, the dot means the temporal derivative, $\mathbf{R} = \{F_{\mathrm{d}},\ F_{\mathrm{l}},\ F_{\mathrm{m}}\}^{\mathrm{T}}$ represents the fluid force and all components are evaluated below

$$F_{\mathrm{d}} = \int_\Sigma \left(\boldsymbol{\sigma}^{\mathrm{f}}_1 \cdot \mathbf{n}^{\mathrm{s}}_1\right) \mathrm{d}\Gamma,\ F_{\mathrm{l}} = \int_\Sigma \left(\boldsymbol{\sigma}^{\mathrm{f}}_2 \cdot \mathbf{n}^{\mathrm{s}}_2\right) \mathrm{d}\Gamma,\ F_{\mathrm{m}} = \int_\Sigma (\Delta\mathbf{x} \times \mathbf{t}^{\mathrm{s}})\, \mathrm{d}\Gamma, \tag{3.2}$$

where $\mathbf{n}^{\mathrm{s}}$ denotes the outward normal of Γ^{s}, $\Delta\mathbf{x}$ designates the distance between P and G, and $\mathbf{t}^{\mathrm{s}}$ is the structural traction.

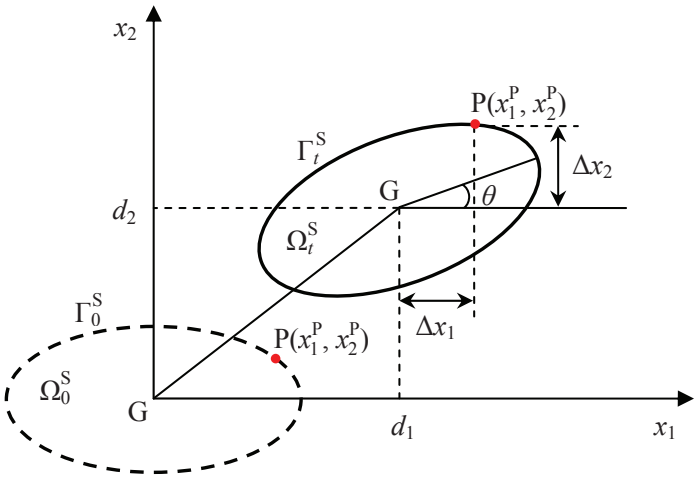

Fig. 3.1 Diagrammatic sketch of the rigid–body motion

In Fig. 3.1 the geometrical relation between $\mathbf{d}^{\mathrm{P}}$ and $\mathbf{d}$ is expressed below [118, 20, 119]

$$\begin{Bmatrix} d_1^{\mathrm{P}} \\ d_2^{\mathrm{P}} \end{Bmatrix} = \begin{Bmatrix} d_1 \\ d_2 \end{Bmatrix} + \begin{bmatrix} \cos\theta - 1 & -\sin\theta \\ \sin\theta & \cos\theta - 1 \end{bmatrix} \begin{Bmatrix} x_1^{\mathrm{P}} \\ x_2^{\mathrm{P}} \end{Bmatrix}, \tag{3.3}$$

where $\mathbf{d}^{\mathrm{P}} = \{d_1^{\mathrm{P}},\ d_2^{\mathrm{P}}\}^{\mathrm{T}}$ and $\mathbf{x}^{\mathrm{P}} = \{x_1^{\mathrm{P}},\ x_2^{\mathrm{P}}\}^{\mathrm{T}}$ means the displacement and coordinates of P, respectively.

The velocity equation is demonstrated via differentiating Eq. (3.3) in regard to t

$$\begin{Bmatrix} \dot{d}_1^{\mathrm{P}} \\ \dot{d}_2^{\mathrm{P}} \end{Bmatrix} = \begin{Bmatrix} \dot{d}_1 \\ \dot{d}_2 \end{Bmatrix} + \dot{\theta} \begin{bmatrix} -\sin\theta & -\cos\theta \\ \cos\theta & -\sin\theta \end{bmatrix} \begin{Bmatrix} x_1^{\mathrm{P}} \\ x_2^{\mathrm{P}} \end{Bmatrix} = \begin{bmatrix} 1 & 0 & -L_2^{\mathrm{P}} \\ 0 & 1 & L_1^{\mathrm{P}} \end{bmatrix} \begin{Bmatrix} \dot{d}_1 \\ \dot{d}_2 \\ \dot{\theta} \end{Bmatrix}, \tag{3.4}$$

where $L_1^{\mathrm{P}} = x_1^{\mathrm{P}}\cos\theta - x_2^{\mathrm{P}}\sin\theta$ and $L_2^{\mathrm{P}} = x_1^{\mathrm{P}}\sin\theta + x_2^{\mathrm{P}}\cos\theta$ are the angle-dependent coefficients. Likewise, the acceleration is gained by differentiating Eq. (3.4) in terms of time

$$\begin{aligned} \begin{Bmatrix} \ddot{d}_1^{\mathrm{P}} \\ \ddot{d}_2^{\mathrm{P}} \end{Bmatrix} &= \begin{Bmatrix} \ddot{d}_1 \\ \ddot{d}_2 \end{Bmatrix} + \ddot{\theta} \begin{bmatrix} -\sin\theta & -\cos\theta \\ \cos\theta & -\sin\theta \end{bmatrix} \begin{Bmatrix} x_1^{\mathrm{P}} \\ x_2^{\mathrm{P}} \end{Bmatrix} + \dot{\theta}^2 \begin{bmatrix} -\cos\theta & \sin\theta \\ -\sin\theta & -\cos\theta \end{bmatrix} \begin{Bmatrix} x_1^{\mathrm{P}} \\ x_2^{\mathrm{P}} \end{Bmatrix} \\ &= \begin{bmatrix} 1 & 0 & -L_2^{\mathrm{P}} \\ 0 & 1 & L_1^{\mathrm{P}} \end{bmatrix} \begin{Bmatrix} \dot{d}_1 \\ \dot{d}_2 \\ \dot{\theta} \end{Bmatrix} - \begin{bmatrix} L_1^{\mathrm{P}} \\ L_2^{\mathrm{P}} \end{bmatrix} \dot{\theta}^2. \end{aligned} \tag{3.5}$$

The dimensionless scales, force coefficients and mass ratio

$$\hat{\mathbf{x}} = \frac{\mathbf{x}}{D},\ \hat{t} = \frac{tU}{D},\ \hat{d}_1 = \frac{d_1}{D},\ \hat{d}_2 = \frac{d_2}{D},$$

$$C_\mathrm{d} = \frac{2F_\mathrm{d}}{\rho^\mathrm{f} U^2 D},\ C_\mathrm{l} = \frac{2F_\mathrm{l}}{\rho^\mathrm{f} U^2 D},\ C_\mathrm{m} = \frac{2F_\mathrm{m}}{\rho^\mathrm{f} U^2 D^2},$$

$$\hat{m}_1 = \frac{m_1}{\rho^\mathrm{f} D^2},\ \hat{m}_2 = \frac{m_2}{\rho^\mathrm{f} D^2},\ \hat{m}_\theta = \frac{m_\theta}{\rho^\mathrm{f} D^4}$$

and the damping ratio and reduced frequency

$$\xi_1 = \frac{c_1}{2\sqrt{m_1 k_1}},\ \xi_2 = \frac{c_2}{2\sqrt{m_2 k_2}},\ \xi_\theta = \frac{c_\theta}{2\sqrt{m_\theta k_\theta}},$$

$$f_{\mathrm{r}1} = \frac{f_{\mathrm{n}1} D}{U},\ f_{\mathrm{r}2} = \frac{f_{\mathrm{n}2} D}{U},\ f_{\mathrm{r}\theta} = \frac{f_{\mathrm{n}\theta} D}{U},$$

$$f_{\mathrm{n}1} = \frac{1}{2\pi}\sqrt{\frac{k_1}{m_1}},\ f_{\mathrm{n}2} = \frac{1}{2\pi}\sqrt{\frac{k_2}{m_2}},\ f_{\mathrm{n}\theta} = \frac{1}{2\pi}\sqrt{\frac{k_\theta}{m_\theta}}$$

are used to nondimensionalize Eq. (3.1), where $f_{\mathrm{n}i}$ designates the natural frequency. As a result, the dimensionless form of the structural equation is described below

$$\ddot{\mathbf{d}} + 4\pi \begin{bmatrix} f_{\mathrm{r}1}\xi_1 & & \\ & f_{\mathrm{r}2}\xi_2 & \\ & & f_{\mathrm{r}\theta}\xi_\theta \end{bmatrix} \dot{\mathbf{d}} + 4\pi^2 \begin{bmatrix} (f_{\mathrm{r}1})^2 & & \\ & (f_{\mathrm{r}2})^2 & \\ & & (f_{\mathrm{r}\theta})^2 \end{bmatrix} \mathbf{d} = \begin{Bmatrix} \dfrac{C_\mathrm{d}}{2\hat{m}_1} \\ \dfrac{C_\mathrm{l}}{2\hat{m}_2} \\ \dfrac{C_\mathrm{m}}{2\hat{m}_\theta} \end{Bmatrix}. \tag{3.6}$$

3.2 Flexible–body dynamics

3.2.1 Equation of structural movement

The elastodynamics equation of a solid is given below [1]

$$\rho^\mathrm{s}\left(\ddot{\mathbf{d}} - \mathbf{f}^\mathrm{s}\right) - \nabla\cdot\boldsymbol{\sigma}^\mathrm{s} = \mathbf{0}, \tag{3.7}$$

in which ρ^s denotes the density, $\mathbf{f}^\mathrm{s}$ represents the body force and $\boldsymbol{\sigma}^\mathrm{s}$ stands for the Cauchy stress. The St. Venant–Kirchhoff material is defined

$$\mathbf{S} = \mathbf{D} : \mathbf{E} \quad \text{and} \quad \mathbf{E} = \frac{1}{2}(\mathbf{F}^\mathrm{T}\cdot\mathbf{F} - \mathbf{I}), \tag{3.8}$$

in which $\mathbf{S}$ means the 2nd Piola–Kirchhoff stress, $\mathbf{D}$ designates the elasticity property and the Green strain $\mathbf{E}$ is calculated from the deformation gradient $\mathbf{F}$. Between $\mathbf{S}$ and $\boldsymbol{\sigma}^{\mathrm{s}}$ is the transformation specified by

$$\mathbf{S} = J\mathbf{F}^{-1}\boldsymbol{\sigma}^{\mathrm{s}}\mathbf{F}^{-\mathrm{T}}, \tag{3.9}$$

in which $J = \det(\mathbf{F})$. Below are boundary/initial conditions specified for the problem

$$\mathbf{d} = \mathbf{g}^{\mathrm{s}} \quad \text{on} \quad \Gamma^{\mathrm{s}}_{\mathrm{d}}, \tag{3.10a}$$

$$\mathbf{t}^{\mathrm{s}} = \boldsymbol{\sigma}^{\mathrm{s}} \cdot \mathbf{n}^{\mathrm{s}} = \mathbf{h}^{\mathrm{s}} \quad \text{on} \quad \Gamma^{\mathrm{s}}_{\mathrm{n}}, \tag{3.10b}$$

$$\mathbf{d}(\mathbf{x},\, 0) = \mathbf{d}^0,\ \dot{\mathbf{d}}(\mathbf{x},\, 0) = \dot{\mathbf{d}}^0,\ \ddot{\mathbf{d}}(\mathbf{x},\, 0) = \ddot{\mathbf{d}}^0 \quad \text{on} \quad \Omega^{\mathrm{s}}_0. \tag{3.10c}$$

Likewise, the following scales

$$\hat{\mathbf{x}} = \frac{\mathbf{x}}{D},\ \hat{t} = \frac{tU}{D},\ \hat{\mathbf{d}} = \frac{\mathbf{d}}{D},\ \hat{E} = \frac{E}{\rho^{\mathrm{f}}U^2},\ \hat{\mathbf{f}}^{\mathrm{s}} = \frac{\mathbf{f}^{\mathrm{s}}D}{U^2},\ \hat{m} = \frac{\rho^{\mathrm{s}}}{\rho^{\mathrm{f}}}$$

are employed to nondimensionalize Eq. (3.7)

$$\ddot{\mathbf{d}} - \frac{1}{\hat{m}}\nabla \cdot \boldsymbol{\sigma}^{\mathrm{s}} - \mathbf{f}^{\mathrm{s}} = \mathbf{0}. \tag{3.11}$$

The dimensionless Young's modulus is the inverse of Cauchy number [120]. Eq. (3.11) accounts for the elastic solid's finite deformation. The linearization of the resulting equilibrium equation is addressed by means of the Newton–Raphson method in total Lagrangian (TL) scheme [121, 22].

3.2.2 Finite element discretization

Here the solid is discretized with FEM. As usual, the Galerkin approximation [97] is applied to the structural variables

$$\mathbf{d} = \mathbf{N}\bar{\mathbf{d}},\ \dot{\mathbf{d}} = \mathbf{N}\dot{\bar{\mathbf{d}}},\ \ddot{\mathbf{d}} = \mathbf{N}\ddot{\bar{\mathbf{d}}}, \tag{3.12}$$

which leads to the incremental dynamic equation

$$\mathbf{K}^n\Delta\bar{\mathbf{d}} = \mathbf{R}^{n+1} - \mathbf{P}^n - \mathbf{M}^{\mathrm{s}}\ddot{\bar{\mathbf{d}}}^{n+1}, \tag{3.13}$$

where $\mathbf{N}$ signifies the element's shape function, $\mathbf{K}$ is the tangent stiffness, $\mathbf{M}^{\mathrm{s}}$ represents the mass, $\mathbf{R}$ represents the applied force, $\mathbf{P}$ denotes the internal force and the increment displacement $\Delta\bar{\mathbf{d}} = \bar{\mathbf{d}}^{n+1} - \bar{\mathbf{d}}^n$.

Finite deformation requires to iterate Eq. (3.13) per loading step via the Newton method [121]. The equilibrium iteration equation may be formulated below

$$\widetilde{\mathbf{K}}^{n}\delta\bar{\mathbf{d}}^{(k)} = \mathbf{R}^{n+1} - \widetilde{\mathbf{P}}^{n+1(k-1)} - \mathbf{M}^{\mathrm{s}}\ddot{\bar{\mathbf{d}}}^{n+1(k)}, \tag{3.14}$$

where $\delta\bar{\mathbf{d}}^{(k)}$ denotes the k-th incremental displacement and the tangent stiffness $\widetilde{\mathbf{K}} = \widetilde{\mathbf{K}}_{\mathrm{l}} + \widetilde{\mathbf{K}}_{\mathrm{nl}}$ admits the representation

$$\Delta\bar{\mathbf{d}}^{(k)} = \Delta\bar{\mathbf{d}}^{(k-1)} + \delta\bar{\mathbf{d}}^{(k)},\ \mathbf{M}^{\mathrm{s}} = \hat{m}\int_{\Omega_0^{\mathrm{s}}}\mathbf{N}^{\mathrm{T}}\mathbf{N}\mathrm{d}\Omega,\ \mathbf{R} = \hat{m}\int_{\Omega^{\mathrm{s}}}\mathbf{N}^{\mathrm{T}}\mathbf{f}^{\mathrm{s}}\mathrm{d}\Omega + \int_{\Gamma_{\mathrm{n}}^{\mathrm{s}}}\mathbf{N}^{\mathrm{T}}\mathbf{h}^{\mathrm{s}}\mathrm{d}\Gamma,$$

$$\widetilde{\mathbf{K}}_{\mathrm{l}} = \int_{\Omega_0^{\mathrm{s}}}\widetilde{\mathbf{B}}_{\mathrm{l}}^{\mathrm{T}}\mathbf{D}\widetilde{\mathbf{B}}_{\mathrm{l}}\mathrm{d}\Omega,\ \widetilde{\mathbf{K}}_{\mathrm{nl}} = \int_{\Omega_0^{\mathrm{s}}}\widetilde{\mathbf{B}}_{\mathrm{nl}}^{\mathrm{T}}\widetilde{\mathbf{S}}\widetilde{\mathbf{B}}_{\mathrm{nl}}\mathrm{d}\Omega,\ \widetilde{\mathbf{P}} = \int_{\Omega^{\mathrm{s}}}\widetilde{\mathbf{B}}_{\mathrm{l}}^{\mathrm{T}}\widetilde{\boldsymbol{\sigma}}^{\mathrm{s}}\mathrm{d}\Omega.$$

These smoothed quantities rest with $\widetilde{\mathbf{F}} = \mathbf{I} + \widetilde{\nabla}\mathbf{d}$, see [122, 123]. Details of the Newton method can be found in [121, 124].

3.3 Smoothed FEM

3.3.1 Overview

In meshless methods *Gradient smoothing* is useful to stabilize the nodal integration [125, 126]. Liu and his colleagues found it a valuable alliance of meshless and finite element methods. Their finding brings about the so-called SFEM that resolves various mechanics problems [127].

The SFEM modifies the compatible strain field, where superior properties may be delivered to a Galerkin model. The SFEM is featured by the so-called "softened" stiffness that results in more accurate solution to discrete PDEs, accompanied with easy implementation and low cost. After over ten years of development, research community has already fostered a group of SFEM models in consideration of different smoothing domains. The textbook co-authored by Liu and Nguyen [128] inspects the method's theoretical basis, highlights its advantages, and depicts its versatility in various disciplines. The reader is also referred to the review article [129] and references therein for more details. Still, the method has been made accessible mainly to solid mechanics.

3.3.2 Theoretical basis

The 2D solid domain Ω is discretized into ne elements so that $\Omega = \Omega_1 \cup \Omega_2 \cup \cdots \cup \Omega_{ne}$ and $\Omega_i \cap \Omega_j = \varnothing$ $(i \neq j)$. For any Q4 element, $\Omega_i = \widetilde{\Omega}_i^1 \cup \widetilde{\Omega}_i^2 \cup \cdots \cup \widetilde{\Omega}_i^{nc}$ where nc is the number of SCs. In an SC (refer to Fig. 3.2), the smoothed gradient of a generic quantity b is approximated at a point $\mathbf{x}_c$

$$\widetilde{\nabla} b(\mathbf{x}_c) = \int_{\widetilde{\Omega}} \nabla b(\mathbf{x}) W(\mathbf{x} - \mathbf{x}_c) \mathrm{d}\Omega, \tag{3.15}$$

where $\widetilde{\nabla}$ means its smoothed gradient operator, $\widetilde{\Omega}$ represents the SC and W is the smoothing function that satisfies [126]

$$W(\mathbf{x} - \mathbf{x}_c) \geqslant 0 \quad \text{and} \quad \int_{\widetilde{\Omega}} W(\mathbf{x} - \mathbf{x}_c) \mathrm{d}\Omega = 1. \tag{3.16}$$

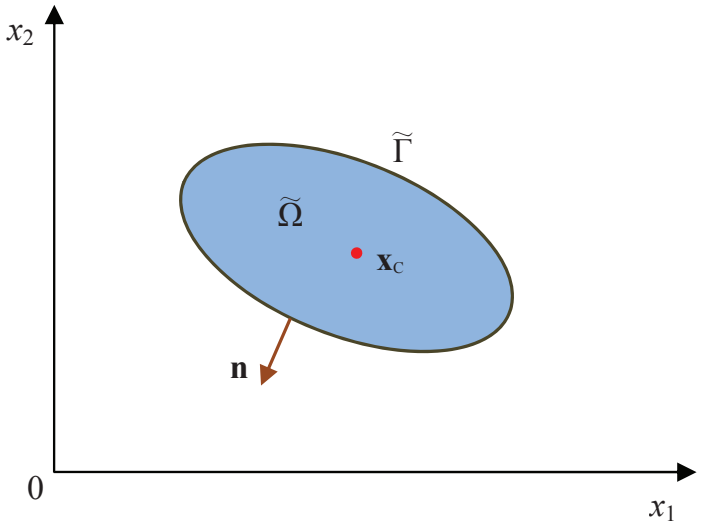

Fig. 3.2 Illustration of an SC

Applying Gauss theorem to Eq. (3.15) yields

$$\widetilde{\nabla} b(\mathbf{x}_c) = \int_{\widetilde{\Gamma}} b(\mathbf{x}) \mathbf{n}(\mathbf{x}) W(\mathbf{x} - \mathbf{x}_c) \mathrm{d}\Gamma - \int_{\widetilde{\Omega}} b(\mathbf{x}) \nabla W(\mathbf{x} - \mathbf{x}_c) \mathrm{d}\Omega, \tag{3.17}$$

where $\widetilde{\Gamma}$ denotes the SC's boundary with the normal $\mathbf{n}$. W is assumed as

$$W(\mathbf{x} - \mathbf{x}_c) = \begin{cases} \dfrac{1}{A_c} & \mathbf{x} \in \widetilde{\Omega}, \\ 0 & \mathbf{x} \notin \widetilde{\Omega}, \end{cases} \tag{3.18}$$

in which $A_c = \int_{\widetilde{\Omega}} d\Omega$. Substituting Eq. (3.18) into Eq. (3.17) leads to

$$\widetilde{\nabla} b(\mathbf{x}_c) = \int_{\widetilde{\Gamma}} b(\mathbf{x})\mathbf{n}(\mathbf{x})W(\mathbf{x}-\mathbf{x}_c)d\Gamma = \frac{1}{A_c}\int_{\widetilde{\Gamma}} b(\mathbf{x})\mathbf{n}(\mathbf{x})d\Gamma, \tag{3.19}$$

which declares that the smoothing operation converts the area integration over each SC into the line integration along the relevant boundaries.

The Galerkin procedure results in the approximation of b below

$$b = N_I \bar{b}_I, \tag{3.20}$$

where N_I denotes the shape function and the bar designates the nodal value. Using Eq. (3.20), Eq. (3.19) is immediately rewritten as

$$\widetilde{\nabla} b(\mathbf{x}_c) = \left(\widetilde{\nabla} N_I(\mathbf{x}_c)\right)\bar{b}_I = \left(\frac{1}{A_c}\int_{\widetilde{\Gamma}} N_I(\mathbf{x})\mathbf{n}(\mathbf{x})d\Gamma\right)\bar{b}_I. \tag{3.21}$$

As one Gaussian point (GP) is used, the item enveloped in external brackets of Eq. (3.21) is transformed into

$$\widetilde{\nabla} N_I(\mathbf{x}_c) = \frac{1}{A_c}\sum_{i=1}^{4} N_I(\mathbf{x}_i^{gp})\mathbf{n}(\mathbf{x}_i^{gp})l_i, \tag{3.22}$$

where $\mathbf{x}_i^{gp}$ is the GP on $\widetilde{\Gamma}_i$ and l_i denotes the length.

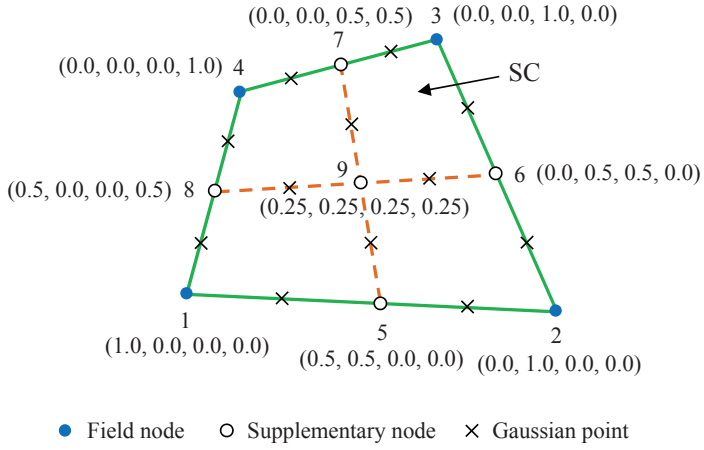

Fig. 3.3 SCs and shape functions

By now, shape functions are needed to construct smoothed gradients for their own sake, without isoparametric mapping. Four SCs are adopted in each element and this division behaves very well in the open literature. The shape functions are built up for the CS-FEM

in Fig. 3.3. Five additional nodes are created for smoothed shape functions via averaging four corners' values[127, 122].

3.4 Time integration algorithms

Time stepping algorithms are widely utilized in the computational structural dynamics. At present, multiple choices are available for temporally advancing the structural motion like the Newmark algorithm [130], Hibert–Hughes–Taylor algorithm [131], Generalized-α algorithm [132] and Bathe algorithm [133–135]. Although the methods listed below have been adpoted by the author for different problems, the Newmark-α method is employed throughout this thesis unless otherwise stated.

3.4.1 Newmark-α scheme

The classical Newmark approximations are given to the structural variables below [130]

$$\dot{\mathbf{d}}^{n+1} = \dot{\mathbf{d}}^{n} + \Delta t((1-\gamma)\ddot{\mathbf{d}}^{n} + \gamma\ddot{\mathbf{d}}^{n+1}), \tag{3.23}$$

$$\mathbf{d}^{n+1} = \mathbf{d}^{n} + \Delta t\dot{\mathbf{d}}^{n} + \Delta t^{2}((\frac{1}{2}-\beta)\ddot{\mathbf{d}}^{n} + \beta\ddot{\mathbf{d}}^{n+1}), \tag{3.24}$$

where $\gamma \geqslant \frac{1}{2}$ and $\beta \geqslant \frac{1}{4}$.

3.4.2 Generalized-α scheme

Here, the structural equation is advance via the Generalized-α method [132] that generally surpasses the Newmark-β method [130]. Therefore, the semi-discrete form of the structural equation at a general midpoint reads

$$\mathbf{M}^{\mathrm{s}}\ddot{\bar{\mathbf{d}}}^{n+1-\alpha_{\mathrm{m}}} + \mathbf{C}\dot{\bar{\mathbf{d}}}^{n+1-\alpha_{\mathrm{f}}} + \mathbf{K}\bar{\mathbf{d}}^{n+1-\alpha_{\mathrm{f}}} = \mathbf{R}^{n+1-\alpha_{\mathrm{f}}}, \tag{3.25}$$

with the damping $\mathbf{C}$ and the stiffness $\mathbf{K}$. It is also dictated that

$$\ddot{\bar{\mathbf{d}}}^{n+1-\alpha_{\mathrm{m}}} = (1-\alpha_{\mathrm{m}})\ddot{\bar{\mathbf{d}}}^{n+1} + \alpha_{\mathrm{m}}\ddot{\bar{\mathbf{d}}}^{n}, \tag{3.26a}$$

$$\dot{\bar{\mathbf{d}}}^{n+1-\alpha_{\mathrm{f}}} = (1-\alpha_{\mathrm{f}})\dot{\bar{\mathbf{d}}}^{n+1} + \alpha_{\mathrm{f}}\dot{\bar{\mathbf{d}}}^{n}, \tag{3.26b}$$

$$\bar{\mathbf{d}}^{n+1-\alpha_\mathrm{f}} = (1-\alpha_\mathrm{f})\bar{\mathbf{d}}^{n+1} + \alpha_\mathrm{f}\bar{\mathbf{d}}^{n}, \tag{3.26c}$$

$$\mathbf{R}^{n+1-\alpha_\mathrm{f}} = (1-\alpha_\mathrm{f})\mathbf{R}^{n+1} + \alpha_\mathrm{f}\mathbf{R}^{n}. \tag{3.26d}$$

At t^{n+1}, acceleration and velocity are given by the Newmark approximations [130]

$$\ddot{\bar{\mathbf{d}}}^{n+1} = \frac{1}{\beta\Delta t^2}(\bar{\mathbf{d}}^{n+1} - \bar{\mathbf{d}}^{n}) - \frac{1}{\beta\Delta t}\dot{\bar{\mathbf{d}}}^{n} - \frac{1-2\beta}{2\beta}\ddot{\bar{\mathbf{d}}}^{n}, \tag{3.27}$$

$$\dot{\bar{\mathbf{d}}}^{n+1} = \frac{\gamma}{\beta\Delta t}(\bar{\mathbf{d}}^{n+1} - \bar{\mathbf{d}}^{n}) - \frac{\gamma-\beta}{\beta}\dot{\bar{\mathbf{d}}}^{n} - \frac{\gamma-2\beta}{2\beta}\Delta t\ddot{\bar{\mathbf{d}}}^{n}. \tag{3.28}$$

At the midpoint, the following equations are obtain

$$\ddot{\bar{\mathbf{d}}}^{n+1-\alpha_\mathrm{m}} = \frac{1-\alpha_\mathrm{m}}{\beta\Delta t^2}(\bar{\mathbf{d}}^{n+1} - \bar{\mathbf{d}}^{n}) - \frac{1-\alpha_\mathrm{m}}{\beta\Delta t}\dot{\bar{\mathbf{d}}}^{n} - \frac{1-\alpha_\mathrm{m}-2\beta}{2\beta}\ddot{\bar{\mathbf{d}}}^{n}, \tag{3.29}$$

$$\dot{\bar{\mathbf{d}}}^{n+1-\alpha_\mathrm{f}} = \frac{(1-\alpha_\mathrm{f})\gamma}{\beta\Delta t}(\bar{\mathbf{d}}^{n+1} - \bar{\mathbf{d}}^{n}) - \frac{(1-\alpha_\mathrm{f})\gamma-\beta}{\beta}\dot{\bar{\mathbf{d}}}^{n} - \frac{(\gamma-2\beta)(1-\alpha_\mathrm{f})}{2\beta}\Delta t\ddot{\bar{\mathbf{d}}}^{n}. \tag{3.30}$$

Integration constants β, γ, α_m and α_f are formulated as [132]

$$\beta = \frac{1}{4}(1-\alpha_\mathrm{m}+\alpha_\mathrm{f})^2,\ \gamma = \frac{1}{2} - \alpha_\mathrm{m} + \alpha_\mathrm{f},\ \alpha_\mathrm{m} = \frac{2\rho_\infty - 1}{\rho_\infty + 1},\ \alpha_\mathrm{f} = \frac{\rho_\infty}{\rho_\infty + 1}, \tag{3.31}$$

where the spectral radius $0 \leqslant \rho_\infty \leqslant 1$ is chosen for numerical dissipation. $\rho_\infty = 0.1$ is specified to the rigid body [136] while $\rho_\infty = 0.5$ to the flexible body [137]. Besides, the internal force is calculated as [138]

$$\widetilde{\mathbf{P}}^{n+1-\alpha_\mathrm{f}} = (1-\alpha_\mathrm{f})\widetilde{\mathbf{P}}^{n+1} + \alpha_\mathrm{f}\widetilde{\mathbf{P}}^{n} = (1-\alpha_\mathrm{f})\widetilde{\mathbf{P}}(\mathbf{d}^{n+1}) + \alpha_\mathrm{f}\widetilde{\mathbf{P}}(\mathbf{d}^{n}). \tag{3.32}$$

3.4.3 Bathe scheme

The Bathe method [133–135, 139] is conserving in momentum and energy without adjustable parameters. The method depends upon the Newmark method for the first substep and the three-point differencing for the second one, respectively. Now $[t, t+\Delta t] = \Delta t[n, n+\alpha] \bigcup \Delta t[n+\alpha, n+1]$ with $0 < \alpha < 1$. The structural equation is integrated within the first substep

$$\mathbf{M}^\mathrm{s}\ddot{\mathbf{d}}^{n+\alpha} + \mathbf{C}\dot{\mathbf{d}}^{n+\alpha} + \mathbf{K}\mathbf{d}^{n+\alpha} = \mathbf{R}^{n+\alpha}. \tag{3.33}$$

If being linearized via the Newmark method, Eq. (3.33) leads to

$$\dot{\mathbf{d}}^{n+\alpha} = \dot{\mathbf{d}}^{n} + (1-\gamma)(\alpha\Delta t)\ddot{\mathbf{d}}^{n} + \gamma(\alpha\Delta t)\ddot{\mathbf{d}}^{n+\alpha}, \tag{3.34}$$

$$\mathbf{d}^{n+\alpha} = \mathbf{d}^{n} + (\alpha\Delta t)\dot{\mathbf{d}}^{n} + (\frac{1}{2}-\beta)(\alpha\Delta t)^2\ddot{\mathbf{d}}^{n} + \beta(\alpha\Delta t)^2\ddot{\mathbf{d}}^{n+\alpha}. \tag{3.35}$$

In light of Eq. (3.35), the intermediate quantity is evaluated as

$$\ddot{\mathbf{d}}^{n+\alpha} = \frac{1}{\beta(\alpha\Delta t)^2}(\mathbf{d}^{n+\alpha} - \mathbf{d}^{n}) - \frac{1}{\beta(\alpha\Delta t)}\dot{\mathbf{d}}^{n} - (\frac{1}{2\beta}-1)\ddot{\mathbf{d}}^{n}. \tag{3.36}$$

Bringing Eqs. (3.34)–(3.36) into Eq. (3.33), the displacement is updated at time $n+\alpha$

$$\begin{aligned}
&\left(\frac{1}{\beta(\alpha\Delta t)^2}\mathbf{M}^{\mathrm{s}} + \frac{\gamma}{\beta(\alpha\Delta t)}\mathbf{C} + \mathbf{K}\right)\mathbf{d}^{n+1} = \mathbf{R}^{n+1} + \\
&\mathbf{M}^{\mathrm{s}}\left(\frac{1}{\beta(\alpha\Delta t)^2}\mathbf{d}^{n} + \frac{1}{\beta(\alpha\Delta t)}\dot{\mathbf{d}}^{n} + (\frac{1}{2\beta}-1)\ddot{\mathbf{d}}^{n}\right) + \\
&\mathbf{C}\left(\frac{\gamma}{\beta(\alpha\Delta t)}\mathbf{d}^{n} + (\frac{\gamma}{\beta}-1)\dot{\mathbf{d}}^{n} + (\frac{\gamma}{2\beta}-1)(\alpha\Delta t)\ddot{\mathbf{d}}^{n}\right).
\end{aligned} \tag{3.37}$$

A general derivative w.r.t. t, $\dot{Q}^{n+1}$, may be written by Q^{n}, $Q^{n+\alpha}$ and Q^{n+1} [140]

$$\dot{Q}^{n+1} = c_1 Q^{n} + c_2 Q^{n+\alpha} + c_3 Q^{n+1}, \tag{3.38}$$

where $c_1 = \frac{1-\alpha}{\alpha\Delta t}$, $c_2 = \frac{1}{(\alpha-1)\alpha\Delta t}$ and $c_3 = \frac{2-\alpha}{(1-\alpha)\Delta t}$. The structural equation discretized at time $n+1$ reads as

$$\mathbf{M}^{\mathrm{s}}\ddot{\mathbf{d}}^{n+1} + \mathbf{C}\dot{\mathbf{d}}^{n+1} + \mathbf{K}\mathbf{d}^{n+1} = \mathbf{R}^{n+1}, \tag{3.39}$$

where according to Eq. (3.38)

$$\dot{\mathbf{d}}^{n+1} = c_1\mathbf{d}^{n} + c_2\mathbf{d}^{n+\alpha} + c_3\mathbf{d}^{n+1}, \tag{3.40}$$

$$\ddot{\mathbf{d}}^{n+1} = c_1\dot{\mathbf{d}}^{n} + c_2\dot{\mathbf{d}}^{n+\alpha} + c_3\dot{\mathbf{d}}^{n+1}, \tag{3.41}$$

Applying Eqs. (3.40) and (3.41) into Eq. (3.39), the following equation is acquired

$$\begin{aligned}
&(c_3c_3\mathbf{M}^{\mathrm{s}} + c_3\mathbf{C} + \mathbf{K})\,\mathbf{d}^{n+1} = \mathbf{R}^{n+1} - \\
&\mathbf{M}^{\mathrm{s}}\left(c_1c_3\mathbf{d}^{n} + c_2c_3\mathbf{d}^{n+\alpha} + c_1\dot{\mathbf{d}}^{n} + c_2\dot{\mathbf{d}}^{n+\alpha}\right) - \mathbf{C}\left(c_1\mathbf{d}^{n} + c_2\mathbf{d}^{n+\alpha}\right),
\end{aligned} \tag{3.42}$$

where $\beta = \frac{1}{4}$ and $\gamma = \frac{1}{2}$ are used for the first substep, whereas $\alpha = \frac{1}{2}$ for the second one. $\mathbf{R}^{n+\alpha}$ may be linearly interpolated between $\mathbf{R}^n$ and $\mathbf{R}^{n+1}$. The Bathe scheme may permit the larger time step that is good for the fluid subcycling [141].

3.5 Validation

The CS-FEM solver is tested through an elastic cantilever being uniformly loading [37], as plotted in Fig. 3.4. The problem properties are specified as: $L = 10$, $H = 1$, $\rho^s = 1.0 \times 10^{-6}$, $E = 1.2 \times 10^4$, $\nu = 0.2$, $\Delta t = 5.0 \times 10^{-5}$ and $tol = 1.0 \times 10^{-8}$. The Newmark method is adopt with $\beta = 0.25$ and $\gamma = 0.5$.

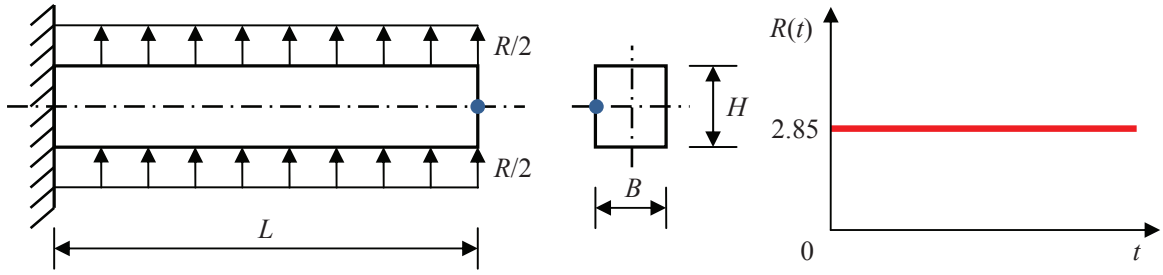

Fig. 3.4 The elastic cantilever under uniformly loading

Three regular Q4 meshes, M1 (2×10 elements), M2 (2×20 elements) and M3 (4×20 elements), are considered. The four SCs are plotted in Fig. 3.3 for each Q4 element. The beam is also meshed with five eight-node quadrilateral (Q8) elements. The TL formulation is utilized to account for the finite deformation.

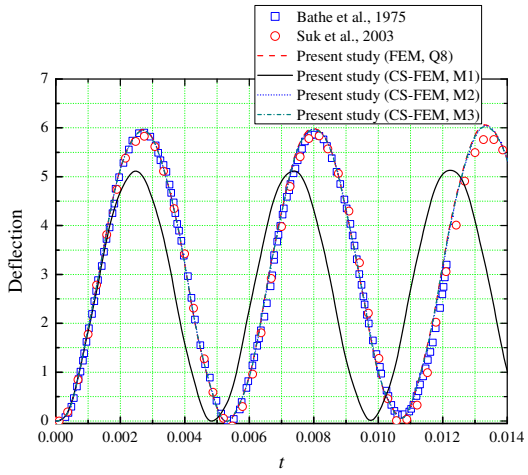

Fig. 3.5 Time histories of beam deflection using different methods

Fig. 3.5 displays dynamic responses using different methods. Only M1 results in the insufficient deflection for the CS-FEM. While utilizing higher mesh resolutions, the obtained results agree well with those of [121, 142]. Fig. 3.6 displays the time history of large deflection on M2. The CS-FEM generates more accurate results [127]. The solver is hence qualified as part of FSI solver.

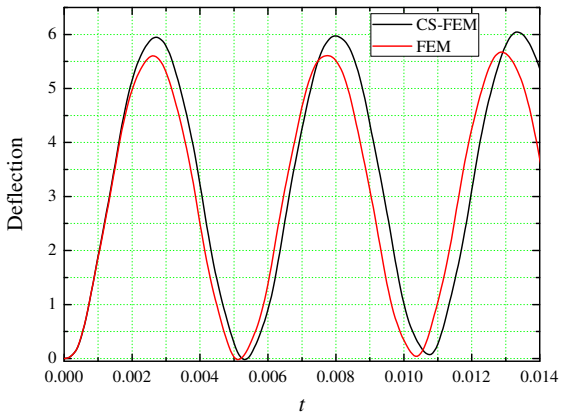

Fig. 3.6 Comparison of large deflection between the CS-FEM and FEM

Chapter 4

Mesh deformation technique

The computation of FSI problems requires the smart and efficient management of moving and deforming spatial domains. To be specific, repositioning moving interface is accurately required for the dynamic domain, with the satisfactory mesh quality. One option is to generate a completely new mesh with the different element connectivity, whenever the domain of interest changes its geometry. This is referred to as *remeshing* [143] or *adaptive meshing* [144]. Normally, the remeshing or adaptive meshing process is a computationally expensive exercise with accuracy loss of field variables due to the interpolation. Alternatively, *mesh moving methods* [145, 146] are used to avoid/minimize such deficiencies. In the mesh moving methods the nodes are relocated to adjust to the new shape of the problem domain, while well retaining their connectivity. This treatment not only saves the cost of generating a new mesh from scratch, but also avoids the afore-mentioned interpolation errors incurred while projecting the data from the old to a new mesh. A good mesh moving scheme should be able to handle fairly large deformations well [1]. It is supposed to maintain the quality of a mesh while deforming it, especially in those critical regions such as those close to a solid wall or high-gradient zones.

4.1 MSA methodology

As indicated above, the mesh deformation is extremely vital to FSI. The present mesh updating combines the MSA (moving submesh approach) [147] with the OST-SAM (ortho-semi-torsional spring analogy method) [148] for time reduction while maintaining the fairly good quality of the updated mesh.

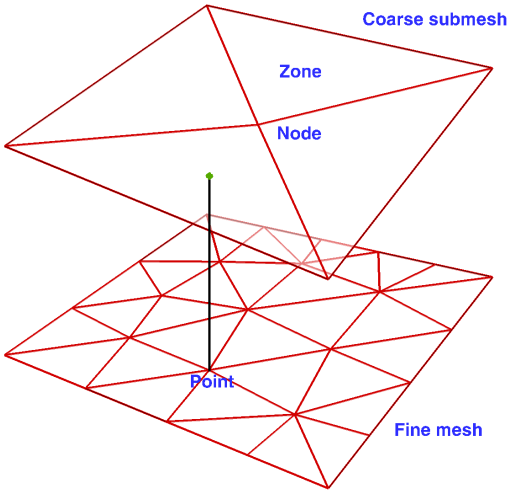

Fig. 4.1 Diagrammatic sketch of the MSA technique

The MSA employs a submesh (*zones*) as background grids in Fig. 4.1. The ALE mesh (*elements*) is re-arranged via the interpolation function. Then the approach is demonstrated below

Step 1: Extract the meshing information
Step 2: Collect points in each zone
Step 3: Compute interpolation formulae for all points
Step 4: Begin the time loops

4.1: Obtain the wall displacement
4.2: Invoke the spring model for interior nodes; otherwise, skip over;
4.3: Renew the submesh
4.4: Update the finite element mesh using interpolation functions
4.5: Examine the meshing quality

Step 5: End the time loops

According to Ref. [147], some key issues ought to be noticed before use. Firstly, only the T3 triangle is available for the submesh, whereas a triangle or quadrangle may be used for the fluid element. Secondly, The resulting interpolation is the T3 element's shape function and only the first three steps are implemented once. Thirdly, the absolute or relative displacement can be used. Finally, a capsule is utilized if encountering a complex structure.

Without interior nodes, any submesh is immediately available (see **Step 4.2**). The pseudo-structural equation due to interior nodes needs to be tackled [145, 149, 150, 146,

148]. The OST-SAM [148] is thus utilized in conjunction with the MSA, which adopts a simple iteration technique [146]. The MSA is far cheaper than the OST-SAM because (i) the MSA is possession of the simple interpolation; (ii) in the MSA the interpolation process is quite fast whereas the SAM requires massive subiterations per time step; (iii) the much fewer subiterations are demanded thanks to interior nodes.

As the MSA preserves the mesh topology very well, smoothing is not needed at all [151]. Actually, the MSA seems a variant of [152] but it is simpler.

4.2 Spring analogy model

The effective treatment of moving submesh due to interior nodes relies upon the OST spring model [148]. The total stiffness of spring analogy model is composed of three parts as follow

$$\tilde{k}_{ij}^{\text{total}} = \tilde{k}_{ij}^{\text{l}} + \tilde{k}_{ij}^{\text{st}} + \tilde{k}_{ij}^{\text{o}}, \tag{4.1}$$

where subscript ij represents the edge i–j of an element in 2D, see Fig. 4.2 for reference.

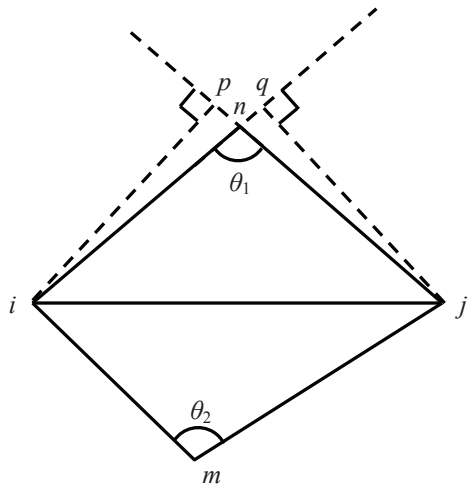

Fig. 4.2 The OST spring analogy model

The specific formulae of the lineal, semi-torsional and orthogonal springs are presented in the following. The lineal spring is calculated by

$$\tilde{k}_{ij}^{\text{l}} = \frac{1}{l_{ij}^{\kappa_{\text{l}}}}, \tag{4.2}$$

where l_{ij} denotes the length of edge i–j and $\kappa_1 = 1$ or 2. In fact, the lineal spring is the scaled model of Batina's spring [145]. The semi-torsional spring is defined in accordance with Zeng and Ethier [146] as follow

$$\tilde{k}_{ij}^{\mathrm{st}} = \kappa_2 \sum_{i=1}^{n_{ij}} \frac{1}{\sin^2 \theta_{ij}}, \tag{4.3}$$

where n_{ij} is the number of opposite angles and $\kappa_2 = 1$. Ultimately, Markou et al. [148] proposed the orthogonal spring in form of

$$\tilde{k}_{ij}^{\mathrm{o}} = \left(\tilde{k}_{ip}^{\mathrm{o}} + \tilde{k}_{jp}^{\mathrm{o}}\right)^{\kappa_3}, \tag{4.4}$$

where

$$\tilde{k}_{ip}^{\mathrm{o}} = \frac{\tilde{k}_{ip}}{\left(\lambda_{ip,1}\right)^{\kappa_4}}, \tag{4.5a}$$

$$\tilde{k}_{jp}^{\mathrm{o}} = \frac{\tilde{k}_{jp}}{\left(\lambda_{jq,1}\right)^{\kappa_4}}, \tag{4.5b}$$

with $\kappa_4 = 2$, $\tilde{k}_{ip} = \frac{1}{l_{ip}}$ and $\tilde{k}_{jq} = \frac{1}{l_{jp}}$.

In Eq. (4.5), the additional allocation coefficients $\lambda_{ip,1}$ and $\lambda_{jq,1}$ are prescribed in terms of the contribution of lineal springs below

$$\lambda_{ip,1} = \frac{l_{in}}{l_{in} + l_{ij}}, \tag{4.6a}$$

$$\lambda_{jq,1} = \frac{l_{jn}}{l_{jn} + l_{ji}}. \tag{4.6b}$$

4.3 Geometric conservation law (GCL)

The GCL is inevitably met in those problems involving moving and/or deformable boundaries. This law states that an ALE simulation duplicates the constant solution of uniform flows exactly [153]. Nevertheless, the existing conclusions drawn in many published papers are controversial regarding the influence of the GCL on time marching. These incompatible statements are compiled by the book chapter [12]. For the present, the majority of researchers believes that the GCL is good for accuracy and stability of the numerical scheme considered.

The popular midpoint rule

$$\mathbf{w}^{n+\frac{1}{2}} = \frac{\mathbf{x}^{n+1} - \mathbf{x}^{n}}{\Delta t}, \tag{4.7}$$

automatically meets the GCL for the 2D stabilized FEM [153]. Though Eq. (4.7) is first-order only, it outperforms the second-order scheme in FSI computation [26].

For a fractional-step-like approach, it is difficult to structure the mesh velocity to satisfy the GCL [154]. To this end, the MST [38] is introduced into the CBS scheme

$$\nabla^2 p^{n+1} = \frac{1}{\Delta t} \nabla \cdot \widetilde{\mathbf{u}} + S_{\text{mst}}^{n+1}, \tag{4.8}$$

with

$$S_{\text{mst}}^{n+1} = \frac{1}{2A_e^{n+1}} \begin{vmatrix} w_1^2 - w_1^1 & w_2^2 - w_2^1 \\ w_1^3 - w_1^1 & w_2^3 - w_2^1 \end{vmatrix}^{n+1} \quad \text{and} \quad \mathbf{w}^{n+1} = \frac{\mathbf{x}^{n+1} - \mathbf{x}^{n}}{\Delta t}, \tag{4.9}$$

where A_e is the element area, the superscript in $\mathbf{w}$ indicates the point number and the subscript the direction.

4.4 Validation

A test is conducted here to reveal the method's efficiency [48]. In Fig. 4.3 the geometry is discretized into 28251 points and 55702 T3 elements. The box is of size 1×1 while the smaller block is 0.2×0.2. The latter moves toward the right wall with a speed of $1/200$. Two different submeshes are considered in Fig. 4.4.

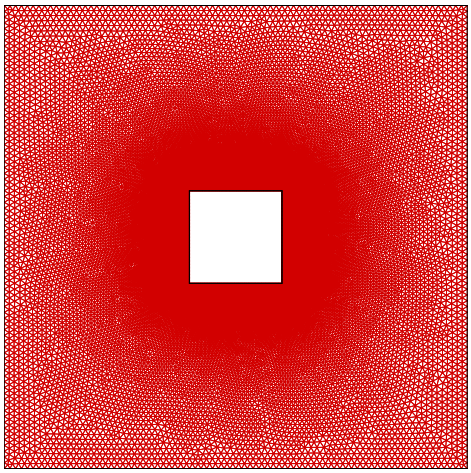

Fig. 4.3 System mesh of the square box

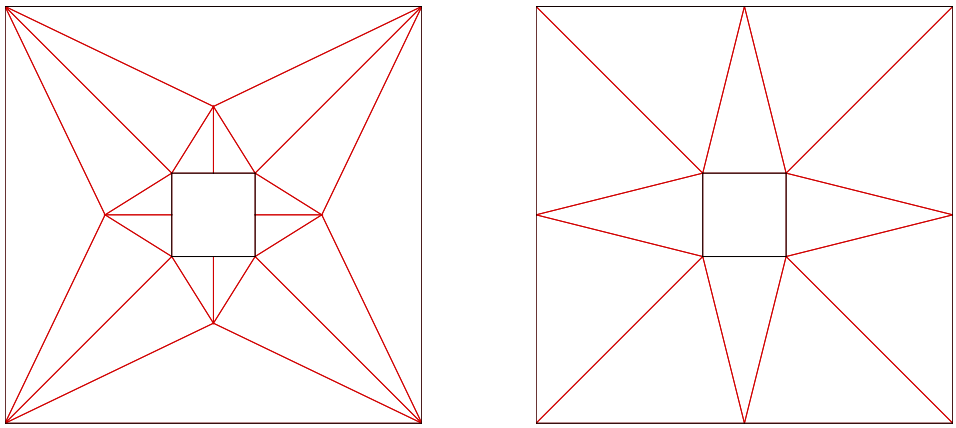

(a) Interior nodes **(b)** No interior nodes

Fig. 4.4 Two submeshes

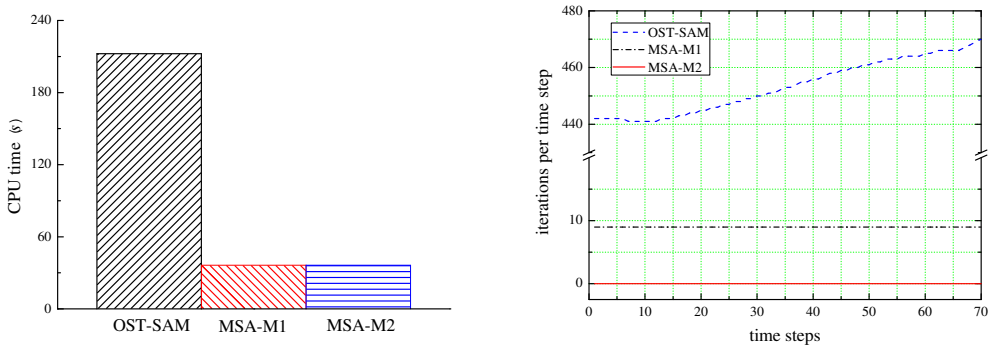

(a) CPU time **(b)** Number of iterations

Fig. 4.5 Comparison of numerical efficiency

The CPU time and iterations are investigated for different dynamic mesh schemes. Fig. 4.5a indicates that this technique significantly saves the cost. The cost of MSA-M1 is almost identical to that of MSA-M2, although the OST-SAM is needed therein. Furthermore, 9 iterations occur in each time step on MSA-M1, seen from Fig. 4.5b. Meanwhile, the OST-SAM asks for over 440 iterations in each time step. It is concluded that the present mesh moving approach holds high efficiency and good accuracy.

Chapter 5

Coupling conditions

5.1 Standard interface conditions

The everlasting interplay of the two media is realized via the two continuity conditions along Σ

$$\mathbf{u} = \dot{\mathbf{d}} \quad \text{and} \quad \mathbf{t}^{\mathrm{f}} = \mathbf{t}^{\mathrm{s}}, \tag{5.1}$$

where $\mathbf{t}^{\mathrm{f}} = \boldsymbol{\sigma}^{\mathrm{f}} \cdot \mathbf{n}^{\mathrm{s}}$ is the fluid traction while $\mathbf{t}^{\mathrm{s}} = \boldsymbol{\sigma}^{\mathrm{s}} \cdot \mathbf{n}^{\mathrm{s}}$ is the structural one, $\mathbf{n}^{\mathrm{s}}$ represents the outward normal on the dry interface and $\mathbf{n}^{\mathrm{f}} = -\mathbf{n}^{\mathrm{s}}$. In addition, the geometric continuity is enforced below

$$\mathbf{x} = \mathbf{d} \quad \text{and} \quad \mathbf{w} = \dot{\mathbf{d}}. \tag{5.2}$$

In numerous partitioned solution approaches, Eq. (5.1) is imposed on Σ directly, or extrapolated [57, 70, 71], or relaxed [17, 66]. Some endeavors are devoted to irregular interface conditions. To respect the GCL accurately, a conserving partitioned algorithm without violating the interfacial continuity is proposed in [16] by staggering half a time step. Braun et al. [124] extended this method to the Generalized-α scheme [132]. Subsequently, the transpiration condition is proposed via Taylor series of flow velocity nearby a predicted interface [155, 156]. Such a temporary interface shapes the frozen boundary where the fluid subsystem is handled efficiently. Bekka et al. [157] utilized the transpiration condition to analyze a rocket nozzle. Apart from the hybrid conditions [1], limited treatments have been designed for interface coupling conditions. In this respect, the Robin transmission condition [62] is a well-known artwork.

Because of the elastic solid, the matching spatial discretizations are produced on the wet and fry interfaces to avoid the accuracy loss. Partially incompatible discretizations are

employed on the interface for a pair of T3 and nine-node quadrilateral (Q9) elements. That is to say, the quantities on the mid-node along each interface edge are simply averaged by those on the two end-nodes of the edge.

5.2 CIBC method

Separately enforcing the interface conditions causes the obvious asynchrony in the partitioned approach. To rule the artifact out, two combined Dirichlet and Neumann residual operators are established below [1, 53]

$$\mathscr{R}_{\mathrm{n/d}}\left(\rho^{\mathrm{f}}\frac{\partial \mathbf{u}^{\mathrm{s}}}{\partial t},\frac{\partial \boldsymbol{\sigma}^{\mathrm{s}}}{\partial t},\frac{\partial \boldsymbol{\sigma}^{\mathrm{f}}}{\partial t},\frac{\partial \boldsymbol{\sigma}^{\mathrm{f}}}{\partial n^{\mathrm{f}}}\right)=\mathbf{0}\quad\text{on}\quad\Sigma, \tag{5.3}$$

inspired by [158, 55]. The idea behind the operators rests with setting up a energy-preserving staggered stencil between two interface PDEs. To this end, a coupling parameter is needed to ally temporal and spatial derivatives in the upcoming CIBC formulae. When $\mathscr{R}_{\mathrm{d}}$ and $\mathscr{R}_{\mathrm{n}}$ are gained, two increments are proposed to amend traditional interface conditions. The derivation will be demonstrated in the following.

It is emphasized that in this section all formulae are dimensional, and the dimensionless formulae are described in Appendix A for the CIBC method [1].

5.2.1 Formulation I

5.2.1.1 Combined interface conditions

For a continuum, the law of momentum conservation may be written as [1]

$$\rho^{\mathrm{i}}\dot{\mathbf{u}}^{\mathrm{i}}=\nabla\cdot\boldsymbol{\sigma}^{\mathrm{i}}+\mathbf{f}^{\mathrm{i}}\quad\text{on}\quad\Omega^{\mathrm{i}}\times(0,\,T), \tag{5.4}$$

where the subscript stands for a fluid or structural variable.

$\mathbf{t}^{\mathrm{f}}=\boldsymbol{\sigma}^{\mathrm{f}}\cdot\mathbf{n}^{\mathrm{f}}$ may be rewritten in light of [54, 52]. Considering Eq. (5.4), the velocity continuity in Eq. (5.1) may be recast as

$$\rho^{\mathrm{f}}\frac{\mathrm{d}\left(\mathbf{u}^{\mathrm{s}}\cdot\mathbf{n}^{\mathrm{s}}\right)}{\mathrm{d}t}=\rho^{\mathrm{f}}\frac{\mathrm{d}\left(\mathbf{u}^{\mathrm{f}}\cdot\mathbf{n}^{\mathrm{f}}\right)}{\mathrm{d}t}=\left(\nabla\cdot\boldsymbol{\sigma}^{\mathrm{f}}\right)\cdot\mathbf{n}^{\mathrm{f}}=\frac{\partial\boldsymbol{\sigma}^{\mathrm{f}}}{\partial n^{\mathrm{f}}}, \tag{5.5}$$

where $\mathbf{f}^{\mathrm{i}}$ is omitted and interface normals remain unchanged for infinitesimal deformation [54]. Then Eq. (5.5) may be simplified to

$$\frac{\partial \boldsymbol{\sigma}^{\mathrm{f}}}{\partial n^{\mathrm{f}}} = \rho^{\mathrm{f}} \dot{\mathbf{u}}^{\mathrm{s}} \cdot \mathbf{n}^{\mathrm{s}}. \tag{5.6}$$

Multiplying on both sides by $\mathbf{u}^{\mathrm{s}}$ and applying $\mathbf{t}^{\mathrm{f}} = \boldsymbol{\sigma}^{\mathrm{f}} \cdot \mathbf{n}^{\mathrm{f}}$, Eq. (5.6) is transformed into

$$\frac{\partial \mathbf{t}^{\mathrm{f}}}{\partial n^{\mathrm{f}}} = \rho^{\mathrm{f}} \dot{\mathbf{u}}^{\mathrm{s}}. \tag{5.7}$$

By differentiating the traction compatibility in Eq. (5.1) in regard to t, the following equation is obtained

$$\dot{\mathbf{t}}^{\mathrm{f}} \cdot \mathbf{n}^{\mathrm{f}} = \dot{\mathbf{t}}^{\mathrm{s}} \cdot \mathbf{n}^{\mathrm{s}}. \tag{5.8}$$

Eqs. (5.7) and (5.8) are the given expressions of $\mathscr{R}_{\mathrm{d}}$ and $\mathscr{R}_{\mathrm{n}}$, respectively. The two equations are considered as the foot-stone of transforming standard interface conditions into the combined ones.

Relating Eqs. (5.7) to (5.8) and $\mathbf{n}^{\mathrm{f}} = -\mathbf{n}^{\mathrm{s}}$, one new velocity relation is obtained on Σ^{s}

$$\rho^{\mathrm{f}} \dot{\mathbf{u}}^{\mathrm{s}} + \omega \dot{\mathbf{t}}^{\mathrm{s}} = \frac{\partial \mathbf{t}^{\mathrm{f}}}{\partial n^{\mathrm{f}}} - \omega \dot{\mathbf{t}}^{\mathrm{f}}, \tag{5.9}$$

and the other one for the traction on Σ^{f}

$$\frac{\partial \mathbf{t}^{\mathrm{f}}}{\partial n^{\mathrm{f}}} + \omega \dot{\mathbf{t}}^{\mathrm{f}} = \rho^{\mathrm{f}} \dot{\mathbf{u}}^{\mathrm{s}} - \omega \dot{\mathbf{t}}^{\mathrm{s}}, \tag{5.10}$$

where ω is positive and keeps the energy stable on the interface [54].

On the ground of the Gauss–Seidel procedure, Eqs. (5.9) and (5.10) may be rewritten on two consecutive time instants below [52]

$$\left(\rho^{\mathrm{f}} \dot{\mathbf{u}}^{\mathrm{s}}\right)^{n} = \left(\frac{\partial \mathbf{t}^{\mathrm{f}}}{\partial n^{\mathrm{f}}}\right)^{n} - \omega \left(\left(\dot{\mathbf{t}}^{\mathrm{f}}\right)^{n} - \left(\dot{\mathbf{t}}^{\mathrm{s}}\right)^{n}\right), \tag{5.11}$$

for velocity along Σ^{s}, while

$$\left(\dot{\mathbf{t}}^{\mathrm{f}}\right)^{n+1} = -\left(\dot{\mathbf{t}}^{\mathrm{s}}\right)^{n+1} + \frac{1}{\omega}\left(\left(\rho^{\mathrm{f}} \dot{\mathbf{u}}^{\mathrm{s}}\right)^{n+1} - \left(\frac{\partial \mathbf{t}^{\mathrm{f}}}{\partial n^{\mathrm{f}}}\right)^{n+1}\right), \tag{5.12}$$

for traction on Σ^{f}. For the constant density, the two corrections are performed below

$$\delta\mathbf{u}^{n}=\frac{\Delta t}{\rho^{\mathrm{f}}}\left(\left(\frac{\partial\mathbf{t}^{\mathrm{f}}}{\partial n^{\mathrm{f}}}\right)^{n}-\omega\left(\left(\dot{\mathbf{t}}^{\mathrm{f}}\right)^{n}-\left(\dot{\mathbf{t}}^{\mathrm{s}}\right)^{n}\right)\right), \tag{5.13}$$

$$\delta\mathbf{t}^{n+1}=\Delta t\left(-\left(\dot{\mathbf{t}}^{\mathrm{s}}\right)^{n+1}+\frac{1}{\omega}\left(\rho^{\mathrm{f}}\left(\dot{\mathbf{u}}^{\mathrm{s}}\right)^{n+1}-\left(\frac{\partial\mathbf{t}^{\mathrm{f}}}{\partial n^{\mathrm{f}}}\right)^{n+1}\right)\right). \tag{5.14}$$

Eq. (5.1) is rectified by the increments (5.13) and (5.14) below

$$\left(\mathbf{u}^{\mathrm{f}}\right)^{n+1}=\left(\mathbf{u}^{\mathrm{s}}\right)^{n+1}+\delta\mathbf{u}^{n}, \tag{5.15}$$

$$\left(\mathbf{t}^{\mathrm{s}}\right)^{n+1}=\left(\mathbf{t}^{\mathrm{f}}\right)^{n+1}+\delta\mathbf{t}^{n+1}. \tag{5.16}$$

Eqs. (5.13) and (5.14) constitute the CIBC method with the parameter ω that offers a proper acceleration-traction combination. Weakly enforcing interface conditions may neglect some physical processes [52]. Therefore, the physical relevance is strengthened for FSI solution, if the corrections are introduced back into traditional interface conditions increases. Once these additional terms are solved, the CIBC method may improve the system's stability and accuracy. Refs. [55, 54] provide the similar process for a simplified FSI model. Eq. (5.14) asks for the structural traction that disappears in rigid-body motion. For this reason, the original CIBC method is not applicable to the interaction between a rigid body and a fluid.

5.2.1.2 Modifications

The latest displacement is applied to the structural traction in [52]. Then it is easy to difference the structural traction for its rate. However, such a process results in a weird reality that the latest structural traction must be used in Eq. (5.14) prior to being corrected. To fixed the defect, a new CIBC formulation [68, 36, 69] is present herein.

The time derivative of Eq. (5.16) is first gained below

$$\left(\dot{\mathbf{t}}^{\mathrm{s}}\right)^{n+1}=\left(\dot{\mathbf{t}}^{\mathrm{f}}\right)^{n+1}+\left(\dot{\delta\mathbf{t}}\right)^{n+1}, \tag{5.17}$$

amounting to

$$\left(\dot{\mathbf{t}}^{\mathrm{s}}\right)^{n}=\left(\dot{\mathbf{t}}^{\mathrm{f}}\right)^{n}+\left(\dot{\delta\mathbf{t}}\right)^{n}. \tag{5.18}$$

Inserting Eq. (5.18) in Eq. (5.11), the velocity increment is obtained by

$$\delta \mathbf{u}^n = \frac{\Delta t}{\rho^{\mathrm{f}}} \left(\left(\frac{\partial \mathbf{t}^{\mathrm{f}}}{\partial n^{\mathrm{f}}} \right)^n + \omega \left(\dot{\delta} \mathbf{t} \right)^n \right), \tag{5.19}$$

where the rate of incremental traction is estimated by

$$\left(\dot{\delta} \mathbf{t} \right)^n = \frac{\delta \mathbf{t}^n - \delta \mathbf{t}^{n-1}}{\Delta t}. \tag{5.20}$$

Likewise, two intermediate equations are obtained via introducing Eq. (5.17) into Eqs. (5.12) and (5.14). With appropriate operations on both equations, the first-order ODEs yield as follow

$$\frac{\mathrm{d}\mathbf{Y}}{\mathrm{d}t} + A\mathbf{Y} = \mathbf{B}, \tag{5.21}$$

along with

$$\mathbf{Y} = \delta \mathbf{t}^{n+1},\ A = \frac{2}{\Delta t},\ \mathbf{B} = \frac{1}{\omega} \left(\rho^{\mathrm{f}} (\dot{\mathbf{u}}^{\mathrm{s}})^{n+1} - \left(\frac{\partial \mathbf{t}^{\mathrm{f}}}{\partial n^{\mathrm{f}}} \right)^{n+1} \right). \tag{5.22}$$

It is easy to know that the general solution of Eq. (5.21) is written as

$$\delta \mathbf{t}^{n+1} = \frac{\Delta t}{2\omega} \left(\rho^{\mathrm{f}} (\dot{\mathbf{u}}^{\mathrm{s}})^{n+1} - \left(\frac{\partial \mathbf{t}^{\mathrm{f}}}{\partial n^{\mathrm{f}}} \right)^{n+1} \right) + \mathbf{C} e^{-\frac{2t}{\Delta t}}, \tag{5.23}$$

where the vector $\mathbf{C}$ is constant and bound. In view of the initial conditions, the following relation is given

$$\mathbf{C} = \frac{2\omega \delta \mathbf{t}^0}{\Delta t \left(\rho^{\mathrm{f}} (\dot{\mathbf{u}}^{\mathrm{s}})^0 - \left(\frac{\partial \mathbf{t}^{\mathrm{f}}}{\partial n^{\mathrm{f}}} \right)^0 \right)}, \tag{5.24}$$

in which all variables are finite at the beginning. As a result, $\mathbf{D} e^{-\frac{2t}{\Delta t}} = \mathbf{0}$ holds when $t \to \infty$. Now the traction increment is obtained below

$$\delta \mathbf{t}^{n+1} = \frac{\Delta t}{2\omega} \left(\rho^{\mathrm{f}} \left(\frac{\partial \mathbf{u}^{\mathrm{s}}}{\partial t} \right)^{n+1} - \left(\frac{\partial \mathbf{t}^{\mathrm{f}}}{\partial n^{\mathrm{f}}} \right)^{n+1} \right), \tag{5.25}$$

As a result, Eqs. (5.19) and (5.25) are the new formulae where $\mathbf{t}^{\mathrm{s}}$ disappears. $(\mathbf{t}^{\mathrm{s}})^{n+1}$ is not needed for traction increment, prior to correcting the traction. This procedure leads to

the non-dimensional CIBC formulae below

$$\delta\mathbf{u}^n = \Delta t \left(\left(\frac{\partial \mathbf{t}^{\mathrm{f}}}{\partial n^{\mathrm{f}}} \right)^n + \omega \left(\dot{\delta}\mathbf{t} \right)^n \right), \tag{5.26}$$

$$\delta\mathbf{t}^{n+1} = \frac{\Delta t}{2\omega} \left((\dot{\mathbf{u}}^{\mathrm{s}})^{n+1} - \left(\frac{\partial \mathbf{t}^{\mathrm{f}}}{\partial n^{\mathrm{f}}} \right)^{n+1} \right). \tag{5.27}$$

Also, the geometric continuity is preserved on Σ as

$$\mathbf{x}_{\Sigma}^{n+1} = \mathbf{d}_{\Sigma}^{n+1} + \delta\mathbf{u}^n \Delta t. \tag{5.28a}$$

Instead, the following equation is derived in view of the relative displacement

$$\Delta\mathbf{x}_{\Sigma}^{n+1} = \Delta\mathbf{d}_{\Sigma}^{n+1} + (\delta\mathbf{u}^n - \delta\mathbf{u}^{n-1})\Delta t. \tag{5.28b}$$

The major differences between new and original CIBC methods are reported below: (i) the structural traction is eliminated before being corrected; (ii) $\omega/\Delta t$ is used to regulate these corrections; (iii) the continuity is maintained for interface displacement; (iv) the present formulation is applied to a rigid body interacting with a fluid.

5.2.2 Formulation II

5.2.2.1 Reformulating combined interface conditions

Original CIBC formulation [54, 52] is based upon $\boldsymbol{\sigma}^{\mathrm{f}} = p\mathbf{I}$, making itself inconvenient for the fluid solver. The fluid stress (2.3) is used to re-formulate a new CIBC formulation [40, 39].

Eq. (5.4) is taken into account here. In consideration of the velocity continuity (5.1), the following equation will be obtained

$$\rho^{\mathrm{f}}\ddot{\mathbf{d}} = \nabla \cdot \boldsymbol{\sigma}^{\mathrm{f}}, \tag{5.29}$$

where no body force occurs on Σ. Differentiating the second equation in Eq. (5.1) in regard to t may gain

$$\dot{\mathbf{t}}^{\mathrm{f}} = \dot{\mathbf{t}}^{\mathrm{s}}. \tag{5.30}$$

Eqs. (5.29) and (5.30) establish the cornerstone of combined interface conditions converted from conventional interface conditions. To this end, the velocity relation on Σ^{s} is illustrated below

$$\rho^{\mathrm{f}}\ddot{\mathbf{d}} + \omega\dot{\mathbf{t}}^{\mathrm{s}} = \nabla\cdot\boldsymbol{\sigma}^{\mathrm{f}} + \omega\dot{\mathbf{t}}^{\mathrm{f}}, \tag{5.31}$$

whereas the other one is written for the traction along Σ^{f} as

$$\omega\dot{\mathbf{t}}^{\mathrm{f}} + \nabla\cdot\boldsymbol{\sigma}^{\mathrm{f}} = \omega\dot{\mathbf{t}}^{\mathrm{s}} + \rho^{\mathrm{f}}\ddot{\mathbf{d}}, \tag{5.32}$$

where ω is the free parameter to ensure the numerical stability.

On the basis of Gauss–Seidel method, Eqs. (5.31) and (5.32) may be recast on two continuous time steps

$$\left(\rho^{\mathrm{f}}\ddot{\mathbf{d}}\right)^{n} = \left(\nabla\cdot\boldsymbol{\sigma}^{\mathrm{f}}\right)^{n} - \omega\left(\left(\dot{\mathbf{t}}^{\mathrm{s}}\right)^{n} - \left(\dot{\mathbf{t}}^{\mathrm{f}}\right)^{n}\right), \tag{5.33}$$

for the velocity on Σ^{s}, and

$$\left(\dot{\mathbf{t}}^{\mathrm{f}}\right)^{n+1} = \left(\dot{\mathbf{t}}^{\mathrm{s}}\right)^{n+1} + \frac{1}{\omega}\left(\left(\rho^{\mathrm{f}}\ddot{\mathbf{d}}\right)^{n+1} - \left(\nabla\cdot\boldsymbol{\sigma}^{\mathrm{f}}\right)^{n+1}\right), \tag{5.34}$$

for the traction on Σ^{f}. For a constant density, the velocity and traction corrections are structured as follows

$$\delta\mathbf{u}^{n} = \frac{\Delta t}{\rho^{\mathrm{f}}}\left(\left(\nabla\cdot\boldsymbol{\sigma}^{\mathrm{f}}\right)^{n} - \omega\left(\left(\dot{\mathbf{t}}^{\mathrm{s}}\right)^{n} - \left(\dot{\mathbf{t}}^{\mathrm{f}}\right)^{n}\right)\right), \tag{5.35}$$

$$\delta\mathbf{t}^{n+1} = \Delta t\left(\left(\dot{\mathbf{t}}^{\mathrm{s}}\right)^{n+1} + \frac{1}{\omega}\left(\rho^{\mathrm{f}}\ddot{\mathbf{d}}^{n+1} - \left(\nabla\cdot\boldsymbol{\sigma}^{\mathrm{f}}\right)^{n+1}\right)\right), \tag{5.36}$$

where ω presents a suitable acceleration-traction joint. The proposed CIBC method contains two increments (5.35) and (5.36) which compensate the interface conditions.

5.2.2.2 A simple revision

Apparently, the lack of consistency is seen when treating the structural traction; namely the traction must be applied into Eq. (5.36) prior to being corrected via Eq. (5.16). Two major deficiencies are hence posed: (i) the failure to handle an oscillating rigid body (ii) the stress prediction may be more complicated [159]. A simple measure is proposed to circumvent the method's restricted use [40, 39].

Replacing Eq. (5.18) in Eq. (5.35) gives the following velocity increment

$$\delta\mathbf{u}^n = \frac{\Delta t}{\rho^{\mathrm{f}}}\left(\left(\nabla\cdot\boldsymbol{\sigma}^{\mathrm{f}}\right)^n - \underline{\omega\delta\dot{\mathbf{t}}^n}\right). \tag{5.37}$$

Inserting Eq. (5.16) into Eq. (5.34), the traction increment may be given by

$$\delta\mathbf{t}^{n+1} = \frac{\Delta t}{\omega}\left(\left(\nabla\cdot\boldsymbol{\sigma}^{\mathrm{f}}\right)^{n+1} - \rho^{\mathrm{f}}\ddot{\mathbf{d}}^{n+1}\right). \tag{5.38}$$

The above two equations are composed of the new CIBC formulae where $\dot{\mathbf{t}}^{\mathrm{s}}$ disappears. The consistency is rescued in traction and the fluid–rigid body interaction can be solved by the new CIBC method. Unlike [68, 36, 69], no ODEs for traction correction are addressed on the interface. In general, Formulation II is more favored.

5.2.2.3 Computational sequence

Eqs. (5.16) and (5.17) are referred to as *Correction I*, whereas the amendments in a reverse order

$$(\mathbf{t}^{\mathrm{s}})^{n+1} = \left(\mathbf{t}^{\mathrm{f}}\right)^{n+1} + \delta\mathbf{t}^n, \tag{5.39}$$

$$\mathbf{u}^{n+1} = \dot{\mathbf{d}}^{n+1} + \delta\mathbf{u}^{n+1}, \tag{5.40}$$

with

$$\delta\mathbf{t}^n = \frac{\Delta t}{\bar{\omega}}\left(\left(\nabla\cdot\boldsymbol{\sigma}^{\mathrm{f}}\right)^n - \ddot{\mathbf{d}}^n\right), \tag{5.41}$$

$$\delta\mathbf{u}^{n+1} = \Delta t\left(\left(\nabla\cdot\boldsymbol{\sigma}^{\mathrm{f}}\right)^{n+1} - \bar{\omega}\dot{\delta}\dot{\mathbf{t}}^n\right). \tag{5.42}$$

are labeled *Correction II* where the displacement is compensated via

$$\mathbf{x}_\Sigma^{n+1} = \mathbf{d}_\Sigma^{n+1} + \delta\mathbf{u}^{n+1}\Delta t. \tag{5.43a}$$

or

$$\Delta\mathbf{x}_\Sigma^{n+1} = \Delta\mathbf{d}_\Sigma^{n+1} + (\delta\mathbf{u}^{n+1} - \delta\mathbf{u}^n)\Delta t. \tag{5.43b}$$

Typically, these two corrections correspond to the predictors used for the partitioned subiterative schemes using force and displacement, respectively. Eq. (5.41) employs $\nabla\cdot\boldsymbol{\sigma}^{\mathrm{f}}$ at time n, though the fluid variables are already renewed. In the meantime, Eq. (5.42) must resort to $\dot{\delta}\dot{\mathbf{t}}^n$ as $\dot{\delta}\dot{\mathbf{t}}^{n+1}$ is not solvable. Hence the computed values in *Correction II* are hysteretic. The difference between these two corrections seems similar to that between

Jacobi and Gauss–Seidel procedures [55]. For the time being, iterating all fields leads the difference towards zero.

5.2.2.4 Weak treatment

Reference [58] shows that correcting two interface conditions is likely to exhibit the worse stability. The reason is not clear yet. The FSI computation will also fail if correcting the two conditions. To fix this issue, limiting the velocity increment seems a good option but hard for evaluating the reduction factor. Herein a weak execution is proposed for the CIBC method [40].

The traction correction may be introduced into the weak form of the elastic solid in order to form the equivalent force below

$$\overline{\mathbf{F}} = \underbrace{\int_{\Omega^{\mathrm{s}}} \mathbf{N}^{\mathrm{T}} \mathbf{f}^{\mathrm{s}} \mathrm{d}\Omega + \int_{\Gamma_{\mathrm{n}}^{\mathrm{s}}} \mathbf{N}^{\mathrm{T}} \mathbf{h}^{\mathrm{s}} \mathrm{d}\Gamma}_{\widetilde{\mathbf{F}}} + \int_{\Sigma} \mathbf{N}^{\mathrm{T}} \mathbf{t}^{\mathrm{s}} \mathrm{d}\Gamma = \widetilde{\mathbf{F}} + \int_{\Sigma} \mathbf{N}^{\mathrm{T}} \left(\mathbf{t}^{\mathrm{f}} + \delta \mathbf{t} \right) \mathrm{d}\Gamma, \tag{5.44}$$

where $\mathbf{N}$ is the shape function and $\Gamma_{\mathrm{n}}^{\mathrm{s}}$ is the Neumann structural boundary. The velocity increment is approximated as

$$\delta \mathbf{u} = \frac{\Delta t}{\rho^{\mathrm{f}}} \nabla \cdot \boldsymbol{\sigma}^{\mathrm{f}}, \tag{5.45}$$

into which Eq. (5.37) may degenerate at convergent state.

5.2.2.5 Source of instability

Two-sided corrections are expected for both velocity and stress continuities on the interface [54, 52]. For the two interface conditions, two modifications may worsen the stability in the coupled thermal simulations [58]. Instead, Roe et al [58] corrected one condition at a time for stable computation. The impact of free parameters on the numerical failure was explained via computer experiments [58, 52]. Here the instability source will be uncovered and then the technically sound CIBC theory, which removes the interface inconsistency, is developed as noticed in Section 5.2.2.4.

In view of Eqs. (5.37) and (5.38), the CIBC corrections is adjusted via ω and $1/\omega$, respectively. It is observed that [39]

$$0 < \omega < 1, \text{ then } \quad \frac{1}{\omega} > 1$$
$$\omega > 1, \text{ then } 0 < \frac{1}{\omega} < 1$$

in which ω and $1/\omega$ are regarded to be amplification factors. In Eq. (5.38) the scope $\omega > 1$ is advocated to prevent possible divergence whereas in Eq. (5.37) it amplifies $\dot{\delta}\mathbf{t}$. It is observed that in Eq. (5.37) the underlined term is the instability source when performing two-sided corrections. To overcome this difficulty, Eq. (5.37) is streamlined into

$$\delta\mathbf{u}^n = \frac{\Delta t}{\rho^{\mathrm{f}}}\left(\nabla\cdot\boldsymbol{\sigma}^{\mathrm{f}}\right)^n. \tag{5.46}$$

$\dot{\delta}\mathbf{t}$ will disappear, provided that the equilibrium is realized. Therefore, the simplification is reasonable. It is stressed that Eq. (5.45) is applied to the elastic solid exclusively but Eq. (5.46) works for rigid or flexible bodies.

5.2.2.6 Application to the rigid body

Fluid–rigid body modeling is intractable as the applied force is a vector which leads the stress equilibrium on Σ to

$$\int_\Sigma \mathbf{t}^{\mathrm{f}}\mathrm{d}\Gamma = \int_\Sigma \mathbf{t}^{\mathrm{s}}\mathrm{d}\Gamma, \tag{5.47a}$$

$$\int_\Sigma \Delta\mathbf{x}\times\mathbf{t}^{\mathrm{f}}\mathrm{d}\Gamma = \int_\Sigma \Delta\mathbf{x}\times\mathbf{t}^{\mathrm{s}}\mathrm{d}\Gamma. \tag{5.47b}$$

If the rotation is omitted, Eqs. (5.30) and (5.31) may be integrated along Σ

$$\int_\Sigma \rho^{\mathrm{f}}\ddot{\mathbf{d}}\mathrm{d}\Gamma = \int_\Sigma \nabla\cdot\boldsymbol{\sigma}^{\mathrm{f}}\mathrm{d}\Gamma \quad \text{and} \quad \int_\Sigma \dot{\mathbf{t}}^{\mathrm{f}}\mathrm{d}\Gamma = \int_\Sigma \dot{\mathbf{t}}^{\mathrm{s}}\mathrm{d}\Gamma. \tag{5.48}$$

Likewise, the following two increments are computed

$$\delta\mathbf{u}^n = \frac{\Delta t}{\rho^{\mathrm{f}} S}\left(\int_\Sigma \nabla\cdot\boldsymbol{\sigma}^{\mathrm{f}}\mathrm{d}\Gamma\right)^n, \tag{5.49a}$$

$$\left(\int_\Sigma \delta\mathbf{t}\mathrm{d}\Gamma\right)^{n+1} = \frac{\Delta t}{\omega}\left(\left(\int_\Sigma \nabla\cdot\boldsymbol{\sigma}^{\mathrm{f}}\mathrm{d}\Gamma\right)^{n+1} - \rho^{\mathrm{f}} S\ddot{\mathbf{d}}^{n+1}\right), \tag{5.49b}$$

where $S = \int_\Sigma \mathrm{d}\Gamma$. Eq. (5.16) gives the velocity correction and the following equation

$$\left(\int_\Sigma \mathbf{t}^{\mathrm{s}}\mathrm{d}\Gamma\right)^{n+1} = \left(\int_\Sigma \mathbf{t}^{\mathrm{f}}\mathrm{d}\Gamma\right)^{n+1} + \left(\int_\Sigma \delta\mathbf{t}\mathrm{d}\Gamma\right)^{n+1}, \tag{5.50}$$

is applied for the traction.

In what follows, Eq. (5.47b) is implicitly corrected [39]. The compatibility condition [118, 20] specifies the relation between $\mathbf{d}^{\mathrm{P}}$ and $\mathbf{d}$ given by Eqs. (3.3) and (3.4). Thus the compact form may be written

$$\dot{\mathbf{d}}^{\mathrm{P}} = \mathbf{T}\dot{\mathbf{d}}, \tag{5.51}$$

where the transformation matrix $\mathbf{T}$ relies on θ as follow

$$\mathbf{T} = \begin{bmatrix} \cos\theta - 1 & -\sin\theta \\ \sin\theta & \cos\theta - 1 \end{bmatrix}. \tag{5.52}$$

In this case, Eq. (5.30) may be rewritten as

$$\rho^{\mathrm{f}}\ddot{\mathbf{d}}^{\mathrm{P}} = \nabla\cdot\boldsymbol{\sigma}^{\mathrm{f}}, \tag{5.53}$$

that is integrated temporally as

$$\rho^{\mathrm{f}}\dot{\mathbf{d}}^{\mathrm{P}} = \Delta t(\nabla\cdot\boldsymbol{\sigma}^{\mathrm{f}}). \tag{5.54}$$

Introducing Eq. (5.52) into Eq. (5.54) will generate

$$\rho^{\mathrm{f}}\mathbf{T}\dot{\mathbf{d}} = \Delta t(\nabla\cdot\boldsymbol{\sigma}^{\mathrm{f}}). \tag{5.55}$$

Now the left inverse matrix $\mathbf{T}_{\mathrm{l}}^{-1}$ is needed so that

$$\rho^{\mathrm{f}}\mathbf{T}_{\mathrm{l}}^{-1}\mathbf{T}\dot{\mathbf{d}} = \rho^{\mathrm{f}}\dot{\mathbf{d}} = \Delta t\mathbf{T}_{\mathrm{l}}^{-1}(\nabla\cdot\boldsymbol{\sigma}^{\mathrm{f}}). \tag{5.56}$$

Unfortunately, $\mathbf{T}_{\mathrm{l}}^{-1}$ does not exist as $\mathbf{T}$ is full-rank in row. This fact can be revealed via the left inverse matrix

$$\mathbf{T}_{\mathrm{l}}^{-1} = (\mathbf{T}^{\mathrm{T}}\mathbf{T})^{-1}\mathbf{T}^{\mathrm{T}}, \tag{5.57}$$

where $|\mathbf{T}^{\mathrm{T}}\mathbf{T}| = 0$. Actually, $\mathbf{T}_{\mathrm{r}}^{-1}$ is attainable. Hence the right inverse matrix is evaluated below

$$\mathbf{T}_{\mathrm{r}}^{-1} = \mathbf{T}^{\mathrm{T}}(\mathbf{T}\mathbf{T}^{\mathrm{T}})^{-1} = \frac{1}{1+(L_1^{\mathrm{P}})^2+(L_2^{\mathrm{P}})^2}\begin{bmatrix} 1+(L_1^{\mathrm{P}})^2 & L_1^{\mathrm{P}}L_2^{\mathrm{P}} \\ L_1^{\mathrm{P}}L_2^{\mathrm{P}} & 1+(L_2^{\mathrm{P}})^2 \\ -L_2^{\mathrm{P}} & L_1^{\mathrm{P}} \end{bmatrix}, \tag{5.58}$$

which implies $\mathbf{T}\mathbf{T}_{\mathrm{r}}^{-1} = \mathbf{I}_{2\times 2}$. Eq. (5.56) is not true. Ultimately, the applied moment is rectified via

$$\begin{aligned}\left(\int_{\Sigma}\Delta\mathbf{x}\times\mathbf{t}^{\mathrm{s}}\mathrm{d}\Gamma\right)^{n+1} &= \left(\int_{\Sigma}\Delta\mathbf{x}\times(\mathbf{t}^{\mathrm{f}}+\delta\mathbf{t})\mathrm{d}\Gamma\right)^{n+1}\\ &= \left(\int_{\Sigma}\Delta\mathbf{x}\times\mathbf{t}^{\mathrm{f}}\mathrm{d}\Gamma\right)^{n+1} + \left(\int_{\Sigma}\Delta\mathbf{x}\times\delta\mathbf{t}\mathrm{d}\Gamma\right)^{n+1}. \end{aligned} \tag{5.59}$$

5.2.2.7 Assessment of free parameter

As we know, ω seems a CFL limit in the staggered velocity-traction joint on Σ, hence playing an crucial role in the global stability and accuracy [68, 40, 39]. To date, evaluating an optimal parameter is nearly impossible in theory. Alternatively, the computer experiment is required to determine the parameter. The author's experience [68] demonstrates that $10 \leqslant \bar{\omega} < +\infty$. This situation partially agrees with the conjugate heat-transfer process [58] in which $10 \leqslant \omega \leqslant 50$ is advocated, but differs from the piston problem [52] where $5.0 \times 10^{-4} \leqslant \omega \leqslant 3.0 \times 10^{-3}$ is numerically attained. Such a difference may rely upon the heat-transfer model which may be suitable to the NS equations [58].

Chapter 6

Partitioned procedures

As mentioned before, partitioned solution strategies involve the explicit, implicit and semi-implicit approaches [1, 77, 160]. The relevant descriptions are provided for all solution algorithms in succedent subsections. Other techniques, such as the structural predictor [57, 71], subcycling [56], interface relaxation [59] and subiteration acceleration [66, 161], can be applied to in these procedures for further improvements.

6.1 Explicit coupling scheme

The partitioned explicit scheme is in favor of the conceptual clarity and simplicity [68]. The staggered solution among all fields is temporally advanced without satisfying the physical conservation. Despite that, this scheme is highly efficient when the oscillating structure is far heavier than the incoming fluid. The overall steps of this scheme are described below and Fig. 6.1 illustrates the flowchart.

Step 1: Guess initial quantities
Step 2: Address the structural problem
Step 3: Correct Dirichlet-type interface variables
Step 4: Deform the ALE fluid mesh
Step 5: Compute mesh velocity and MST
Step 6: Solve the fluid problem
Step 7: Correct Neumann-type interface variables
Step 8: Proceed

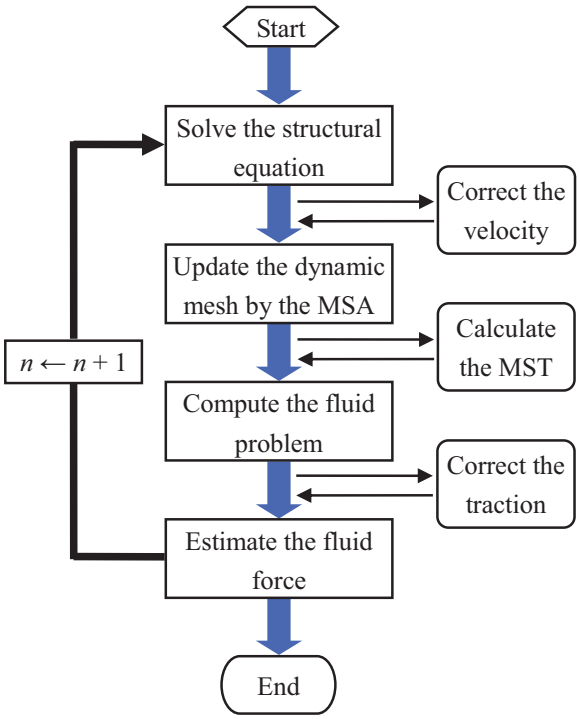

Fig. 6.1 Flowchart of partitioned explicit coupling scheme

6.2 Implicit coupling algorithm

Implicit coupling schemes respect the conservation laws at each time step [36]. It is considerably beneficial to iterate all individual fields when facing outstanding added-mass effect or extremely large deformation of the solid, although the lower efficiency may be gained. The fixed-point method is utilized incorporating the Aitken's Δ^2 technique [65, 66]. The associated procedure is written below and the flowchart is referred to Fig. 6.2.

Step 1: Guess initial values and set $k = 0$
Step 2: Extrapolate the interface

$$(\widetilde{\mathbf{x}}_\Sigma)_k^{n+1} = \mathbf{x}_\Sigma^n + \Delta t \left(\frac{3}{2}\dot{\mathbf{x}}_\Sigma^n - \frac{1}{2}\dot{\mathbf{x}}_\Sigma^{n-1} \right)$$

Step 3: Set $k \leftarrow k+1$
Step 4: Deform the ALE fluid mesh
Step 5: Compute the mesh velocity

$$\mathbf{w}_{k-1}^{n+1} = \frac{\widetilde{\mathbf{x}}_{k-1}^{n+1} - \mathbf{x}^n}{\Delta t}$$

Step 6: Calculate the MST

$$(S_{\mathrm{mst}})_{k-1}^{n+1} = \left(\frac{1}{2A_e} \begin{vmatrix} w_1^2 - w_1^1 & w_2^2 - w_2^1 \\ w_1^3 - w_1^1 & w_2^3 - w_2^1 \end{vmatrix} \right)_{k-1}^{n+1}$$

Step 7: Obtain the auxiliary velocity

$$\widetilde{\mathbf{u}} - \mathbf{u}^n = \Delta t \left(-\mathbf{c}^n \cdot \nabla \mathbf{u}^n + \frac{1}{Re} \nabla^2 \mathbf{u}^n + \frac{\Delta t}{2} \mathbf{c}^n \cdot \nabla (\mathbf{c}^n \cdot \nabla \mathbf{u}^n) \right)$$

Step 8: Update the pressure

$$\nabla^2 p_k^{n+1} = \frac{1}{\Delta t} \nabla \cdot \widetilde{\mathbf{u}} + (S_{\mathrm{mst}})_{k-1}^{n+1}$$

Step 9: Correct the flow velocity

$$\mathbf{u}_k^{n+1} - \widetilde{\mathbf{u}} = -\Delta t \left(\nabla^2 p_k^{n+1} - \frac{\Delta t}{2} \mathbf{c}^n \cdot \nabla^2 p^n \right)$$

Step 10: Evaluate the traction increment for CIBC corrections

Step 11: Solve the structural equation

$$\left(\frac{1}{\beta \Delta t^2} \mathbf{M}^{\mathrm{s}} + \frac{\gamma}{\beta \Delta t} \mathbf{C} + \mathbf{K} \right) \mathbf{d}_k^{n+1} = \mathbf{R}_k^{n+1} + \mathbf{M}^{\mathrm{s}} \left(\frac{1}{\beta \Delta t^2} \mathbf{d}^n + \frac{1}{\beta \Delta t} \dot{\mathbf{d}}^n + \frac{1-2\beta}{2\beta} \ddot{\mathbf{d}}^n \right) + \mathbf{C} \left(\frac{\gamma}{\beta \Delta t} \mathbf{d}^n + \frac{\gamma - \beta}{\beta} \dot{\mathbf{d}}^n + \frac{\gamma - 2\beta}{2\beta} \Delta t \ddot{\mathbf{d}}^n \right)$$

Step 12: Evaluate the velocity increment for CIBC corrections

Step 13: Estimate the interfacial residuals

$$\mathbf{r}_k = \left| (\mathbf{x}_\Sigma)_k^{n+1} - (\widetilde{\mathbf{x}}_\Sigma)_{k-1}^{n+1} \right|$$

Step 14: Go ahead if divergent

Step 15: Re-calculate the relaxation factor λ_k^{n+1}

Step 16: Predict the interface

$$(\widetilde{\mathbf{x}}_\Sigma)_k^{n+1} = \lambda_k^{n+1} (\mathbf{x}_\Sigma)_k^{n+1} + (1 - \lambda_k^{n+1}) (\widetilde{\mathbf{x}}_\Sigma)_{k-1}^{n+1}$$

Step 17: Return

Also, the external force can be predicted for the structural motion [71, 69]. The modifications are trivial to the implicit coupling procedure. As stated in [69], this action prevents the lagged variables from the CIBC formulae, which may be central to accelerating inner-iterations.

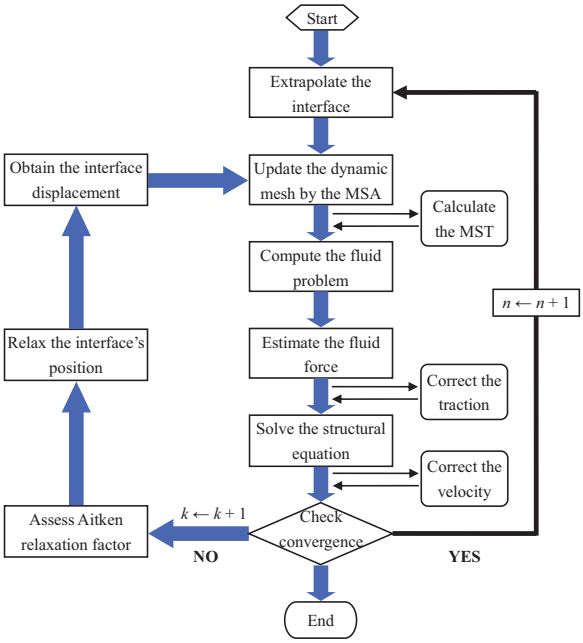

Fig. 6.2 Flowchart of partitioned implicit coupling scheme

6.3 Semi-implicit coupling algorithm

The semi-implicit algorithm is regarded as a balance between explicit and implicit coupling methods. As stated earlier, the work [18] motivates the CBS-based scheme [40, 39]. The CBS scheme is applicable to both the fluid subsystem and global system. The fixed-point method couples the projection step and structural equation via with Aitken's Δ^2 accelerator. The overall algorithm is detailed below.

Step 1: Guess initial values and set $k = 0$

Step 2: Advance the explicit stage

2.1: Extrapolate the interface

$$(\widetilde{\mathbf{x}}_\Sigma)_k^{n+1} = \mathbf{d}_\Sigma^n + \left(\frac{3}{2}\dot{\mathbf{d}}_\Sigma^n - \frac{1}{2}\dot{\mathbf{d}}_\Sigma^{n-1}\right)\Delta t$$

2.2: Deform the ALE fluid mesh

2.3: Compute the mesh velocity

$$\mathbf{w}_k^{n+1} = \frac{\widetilde{\mathbf{x}}_k^{n+1} - \mathbf{x}^n}{\Delta t}$$

2.4: Calculate the MST

$$(S_{\text{mst}})_k^{n+1} = \left(\frac{1}{2A_e} \begin{vmatrix} w_1^2 - w_1^1 & w_2^2 - w_2^1 \\ w_1^3 - w_1^1 & w_2^3 - w_2^1 \end{vmatrix} \right)_k^{n+1}$$

2.5: Obtain the auxiliary velocity

$$\widetilde{\mathbf{u}} - \mathbf{u}^n = \Delta t \left(-\mathbf{c}^n \cdot \nabla \mathbf{u}^n + \frac{1}{Re} \nabla^2 \mathbf{u}^n + \frac{\Delta t}{2} \mathbf{c}^n \cdot \nabla (\mathbf{c}^n \cdot \nabla \mathbf{u}^n) \right)$$

2.6: Correct the traction for the rigid body

Step 3: Advance the implicit stage

3.1: Let $k \leftarrow k+1$

3.2: Update the pressure field

$$\nabla^2 p_k^{n+1} = \frac{1}{\Delta t} \nabla \cdot \widetilde{\mathbf{u}} + (S_{\text{mst}})_{k-1}^{n+1}$$

3.3: Correct the flow velocity

$$\mathbf{u}_k^{n+1} - \widetilde{\mathbf{u}} = -\Delta t \left(\nabla^2 p_k^{n+1} - \frac{\Delta t}{2} \mathbf{c}^n \cdot \nabla^2 p^n \right)$$

3.4: Correct the external force

$$\left(\int_\Sigma \mathbf{t}^{\text{s}} \mathrm{d}\Gamma \right)_k^{n+1} = \left(\int_\Sigma \mathbf{t}^{\text{f}} \mathrm{d}\Gamma \right)_k^{n+1} + \left(\int_\Sigma \delta \mathbf{t} \mathrm{d}\Gamma \right)^n \quad \text{for the rigid body;}$$

$$\overline{\mathbf{F}}_k^{n+1} = \widetilde{\mathbf{R}}_k^{n+1} + \int_\Sigma \left(\left(\mathbf{N}^{\text{T}} \mathbf{t}^{\text{f}} \right)_k^{n+1} + \left(\mathbf{N}^{\text{T}} \right)_k^{n+1} \delta \mathbf{t}^n \right) \mathrm{d}\Gamma \quad \text{for the flexible body}$$

3.5: Solve equation of the structural motion

$$\left(\frac{1}{\beta \Delta t^2} \mathbf{M}^{\text{s}} + \frac{\gamma}{\beta \Delta t} \mathbf{C} + \mathbf{K} \right) \mathbf{d}_k^{n+1} = \mathbf{F}_k^{n+1} + \mathbf{M}^{\text{s}} \left(\frac{1}{\beta \Delta t^2} \mathbf{d}^n + \frac{1}{\beta \Delta t} \dot{\mathbf{d}}^n + \frac{1-2\beta}{2\beta} \ddot{\mathbf{d}}^n \right) + \mathbf{C} \left(\frac{\gamma}{\beta \Delta t} \mathbf{d}^n + \frac{\gamma - \beta}{\beta} \dot{\mathbf{d}}^n + \frac{\gamma - 2\beta}{2\beta} \Delta t \ddot{\mathbf{d}}^n \right)$$

3.6: Evaluate the velocity increment

$$\delta\mathbf{u}_k^{n+1} = \frac{\Delta t}{S}\int_\Sigma \left(\left(\nabla\cdot\boldsymbol{\sigma}^{\mathrm{f}}\right)_k^{n+1} - \bar{\omega}\dot{\delta}\mathbf{t}^n\right)\mathrm{d}\Gamma \quad \text{for the rigid body;}$$

$$\delta\mathbf{u}_k^{n+1} = \Delta t\left(\nabla\cdot\boldsymbol{\sigma}^{\mathrm{f}}\right)_k^{n+1} \quad \text{for the elastic solid}$$

3.7: Restore the displacement continuity

$$(\mathbf{x}_\Sigma)_k^{n+1} = \mathbf{d}_\Sigma^{n+1} + \delta\mathbf{u}_k^{n+1}\Delta t$$

3.8: Estimate the residuals on the interface

$$\mathbf{r}_k = \left|\,(\mathbf{x}_\Sigma)_k^{n+1} - (\widetilde{\mathbf{x}}_\Sigma)_{k-1}^{n+1}\,\right|$$

3.9: Go ahead if divergent

3.10: Determine the relaxation factor λ_k^{n+1}

3.11: Relax the interface

$$(\widetilde{\mathbf{x}}_\Sigma)_k^{n+1} = \lambda_k^{n+1}(\mathbf{x}_\Sigma)_k^{n+1} + (1-\lambda_k^{n+1})(\widetilde{\mathbf{x}}_\Sigma)_{k-1}^{n+1}$$

3.12: Assess the mesh velocity on Σ

$$(\mathbf{w}_\Sigma)_k^{n+1} = \frac{(\widetilde{\mathbf{x}}_\Sigma)_k^{n+1} - \mathbf{x}_\Sigma^n}{\Delta t}$$

3.13: Update the MST for interfacial elements

3.14: Return

The resulting flowchart is demonstrated in Fig. 6.3. In what follows, it is seen that the semi-implicit scheme is cheaper than its implicit counterpart.

6.4 Aitken's Δ^2 relaxation

The Aitken accelerator [162] is useful and simple for subiteration acceleration. The vector extrapolation can be found in [67]. At the k-th iteration per time step, the dynamic relaxation

factor is estimated as [66]

$$\lambda_k^{n+1} = \begin{cases} \max(\lambda_{\max},\ \lambda^n) & k = 1, \\ -\lambda_{k-1}^{n+1} \dfrac{\mathbf{r}_k^{\mathrm{T}}(\mathbf{r}_k - \mathbf{r}_{k-1})}{|\mathbf{r}_k - \mathbf{r}_{k-1}|^2} & k \geqslant 2, \end{cases} \tag{6.1}$$

where $\lambda_{\max} = 0.1$ and $\lambda_1^0 = 0.5$. The Aitken factor may be confined to $(0,\ 1)$ [163].

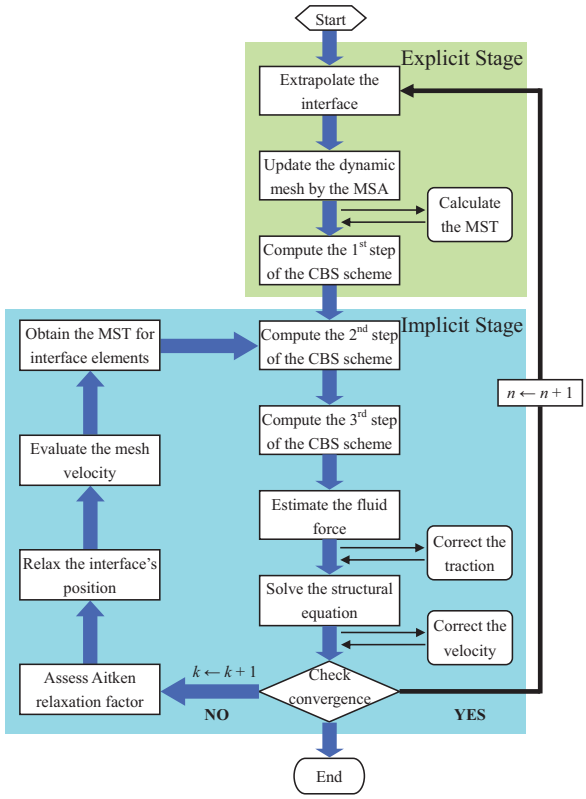

Fig. 6.3 Flowchart of partitioned semi-implicit coupling scheme

Chapter 7

Numerical Examples

This chapter investigates a number of FSI examples by means of the proposed partitioned coupling strategies incorporating the hybrid interface conditions [1]. All examples considered here have long been of scientific and practical importance. Despite relatively simple geometries and low Reynolds numbers, they are associated with rich flow-induced phenomena and are very common to bluff body flows [164].

7.1 Cross-flow vibrations of a circular cylinder

The first test reproduces the well-known experiment in [165], where a circular cylinder can vibrate transversely in Fig. 7.1. The problem properties are given as [165]: $D = 0.16$ cm, $\rho^{\mathrm{f}} = 0.01$ g/(cm $\cdot$ s), $\mu = 1.0$ g/cm^3, $m_2 = 2.979$ g, $k_2 = 5790.9$ g/s^2 and $c_2 = 0.325$ g/s.

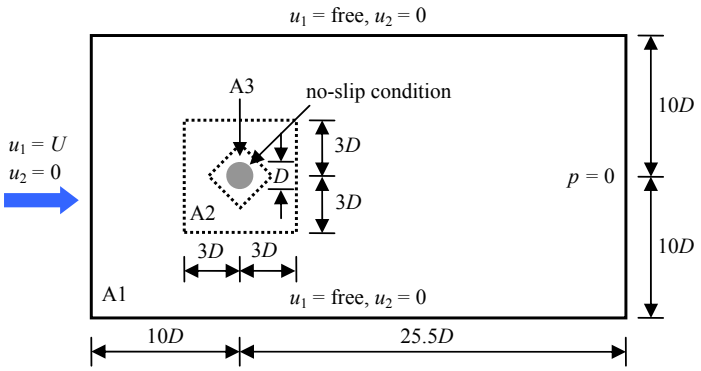

Fig. 7.1 Sketch of the transversely vibrating circular cylinder

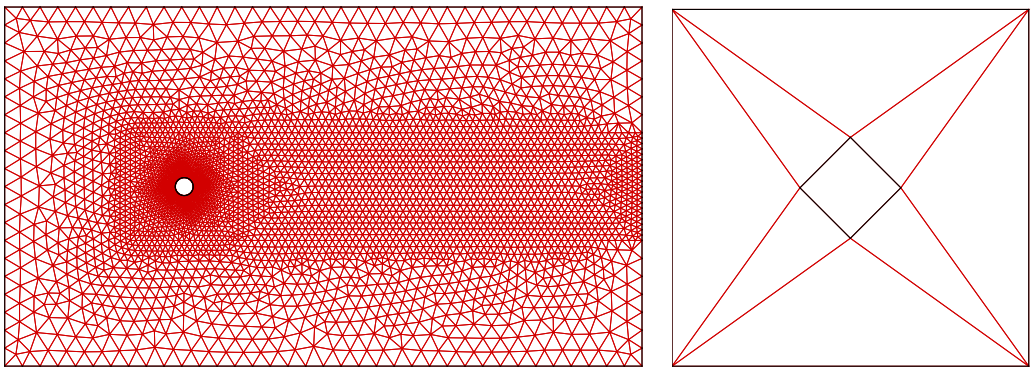

(a) FE mesh for fluid domain **(b)** Submesh for ALE domain

Fig. 7.2 Finite element mesh and MSA submesh

Table 7.1 Numerical results based upon various ϕ

Ratio	$d_{\max 2}$	$C_{\mathrm{d,mean}}$	$C_{\mathrm{d,rms}}$	$C_{\mathrm{l,max}}$	$C_{\mathrm{l,rms}}$	St	$f_{\mathrm{v}}/f_{\mathrm{n}}$
$\phi = 1.0$	0.404	1.8684	0.2505	0.4294	0.2906	0.1793	0.9981
$\phi = 1.5$	0.409	1.8739	0.2541	0.4586	0.3076	0.1793	0.9981
$\phi = 2.0$	0.413	1.8801	0.2580	0.4834	0.3248	0.1793	0.9981
$\phi = 2.5$	0.417	1.8837	0.2603	0.5156	0.3444	0.1793	0.9981
$\phi = 3.0$	0.420	1.8872	0.2626	0.5446	0.3647	0.1790	0.9965

In Fig. 7.1 the domain is grouped into Lagrangian, ALE and Eulerian zones, respectively. Fig. 7.2a comprises 4141 points and 8092 T3 elements, while Fig. 7.2b plots the corresponding submesh. The implicit algorithm is applied with $\Delta t = 1.0 \times 10^{-2}$ and $tol = 1.0 \times 10^{-6}$.

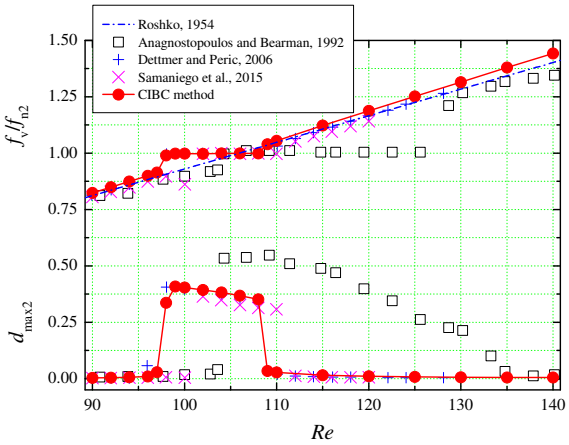

Fig. 7.3 The amplitudes and frequency ratios at different *Re*

As mentioned earlier, dual-time steps [42] seek the optimal steady solution of compressible fluid flow. This technique is used to improve the pressure stabilization for Stokes problems [85, 92]. The second-order terms multiplied by $(\Delta t)^2$ stabilizes the pressure in the AC-CBS scheme. $(\Delta t)^2$ may be written as $\Delta t_{\text{ext}}\Delta t_{\text{int}}$ for stability. The external time step Δt_{ext} is responsible for temporal stability whereas the internal time step Δt_{int} for spatial stability. The ratio $\phi = \Delta t_{\text{int}}/\Delta t_{\text{ext}}$ is defined to quantify the impact of the technique. Since $\phi > 1.0$ is possibly beneficial for the deformable mesh problem [85], dual time steps are adopted as: $\phi = 1.0$ is used for the Eulerian and Lagrangian elements, whereas ϕ varies for the ALE elements. The $Re = 100$ flow is selected for the investigations. Table 7.1 records the obtained results for different ϕ.

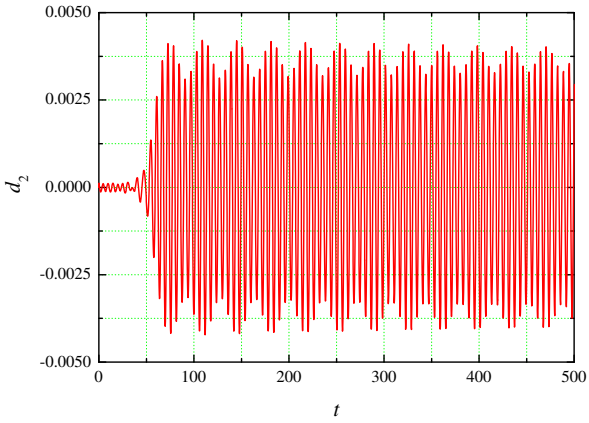

Fig. 7.4 Time history of displacement at $Re = 92$

The slight difference amongst these results are seen from Table 7.1. Generally, a larger ϕ leads to an increase in computed date except St. The large ϕ like $\phi = 3.0$ results in the oscillatory aerodynamic parameters and delays the *lock-in* phenomenon. This is because (1) the Stokes equation is the simplified NS equations; (2) $\Delta t_{\text{ext}}\Delta t_{\text{int}}$ disappears in the current CBS scheme, see Eq. (4.8); (3) enlarging ϕ is equivalent to an improper stabilization that destabilizes the NS solution. Therefore, $\phi = 1.0$ is adopted for further simulations.

The critical parameters are collected among a number of previously published articles [166–169, 136, 170, 143] in Table 7.2 where an agreement between previous and present results is seen. Nevertheless, the lock-in is not aroused in some papers at this Re . Table 7.3 listed the amplitude from those existing papers [165, 171, 108, 166–169, 136, 170, 172, 173]. It is found that, d_{max2} is limited from 0.29 to 0.54 and Re changes from 95 to 115. The present method produces the rational data.

Table 7.2 Comparison of computed results at $Re = 100$

Reference	$d_{\max 2}$	St	f_v/f_n
Wei et al. [166]	0.442	0.1792	0.9979
Schulz and Kallinderis [167]	0.478	0.1773	0.9970
Li et al. [168]	0.420	0.1793	0.9999
Abdullah et al. [169]	0.290	–	–
Dettmer and Perić [136] (3598 elements)	0.403	0.1790	0.9965
Dettmer and Perić [136] (5374 elements)	0.397	0.1794	0.9987
Yang et al. [170]	0.393	0.1777	0.9895
Yang et al. [143]	0.459	0.1791	0.9972
He et al. [68]	0.407	0.1807	1.0060
He et al. [36]	0.404	0.1793	0.9981
He [69]	0.404	0.1793	0.9981

Table 7.3 The amplitude and Re during lock-in

Reference	$d_{\max 2}$	Re
Anagnostopoulos and Bearman [165]	0.54	108.7
Nomura [171]	0.29	110
Anagnostopoulos [108]	0.535	102.7
Wei et al. [166]	0.44	100
Schulz and Kallinderis [167]	0.49	95
Li et al. [168]	0.42	100
Abdullah et al. [169]	0.29	108.5
Dettmer and Perić [136] (1878 elements)	0.407	106
Dettmer and Perić [136] (3598 elements)	0.403	100
Dettmer and Perić [136] (5374 elements)	0.405	98
Yang et al. [170]	0.42	95
Bahmani and Akbari [110]	0.47	115
De Rosis et al. [172]	0.403	98
Samaniego et al. [173]	0.365	102
He et al. [68]	0.411	99
He et al. [36]	0.408	99
He [69]	0.409	99

In Fig. 7.3 $d_{\max 2}$ and $f_{\mathrm{v}}/f_{\mathrm{n}2}$ are examined at different Re. In consideration of the complexity of VIV and different approaches, there may exist some scatter between previous and present data [165, 136, 172, 173]. Fig. 7.3 also plots the well-know Roshko graph [98]

$$St = 0.212 \times (1.0 - \frac{21.2}{Re}). \tag{7.1}$$

The slightly narrower *lock-in* covers $97 \leqslant Re \leqslant 108$ which agrees with [174, 136, 172, 173]. Despite that, the graph trend is identical to the others. Once Re is less than the lower end, the oscillations are faint and the Strouhal frequency is lower than the fundamental frequency. Fig. 7.4 shows that *beating* occurs at $Re = 92$ as the amplitude is modulated. The amplitude reaches to a high level sharply if Re touches the lower end. Overall, the cylinder goes through the strong motions during lock-in, and its amplitude deceases smoothly when Re increases. Meanwhile, $f_{\mathrm{v}}/f_{\mathrm{n}2}$ is roaming around 1, as the oscillation and vortex-shedding frequencies are synchronized. The displacement evolution at $Re = 100$ is depicted in Fig. 7.5, indicating lock-in evidently. The amplitude descends sharply if Re is located outside of the upper end. f_{v} reaches a large value if Re still increases. f_{v} is unlocked again. In Fig. 7.6 the beating is more modulated at $Re = 120$, opposite to [165].

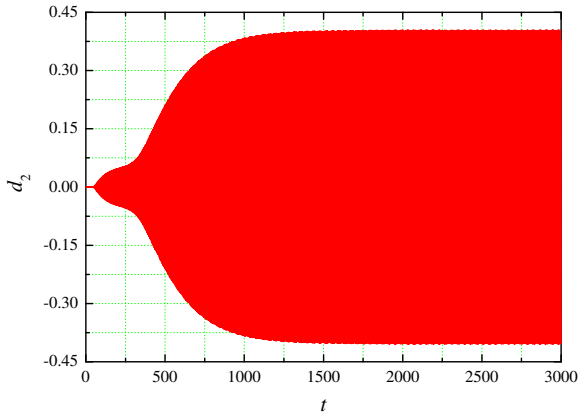

Fig. 7.5 Time history of displacement at $Re = 100$

Vorticity contours are demonstrated in Fig. 7.7 – 7.9, respectively. Low-amplitude oscillations are seen out of the lock-in range, while violent oscillations result from $Re = 100$. Different from [110], the 2S type is observed behind the wake, but the C(2S) type [117] is not exposed. The spacing between two lines of vorticities is somewhat reduced at $Re = 100$.

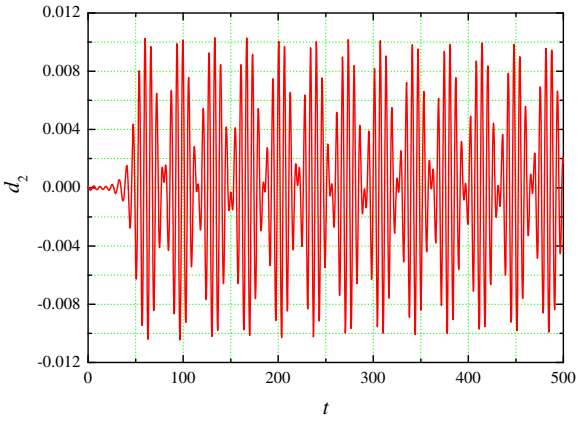

Fig. 7.6 Time history of displacement at $Re = 120$

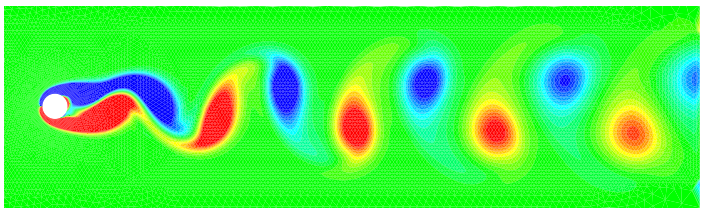

Fig. 7.7 Vorticity field at $Re = 92$

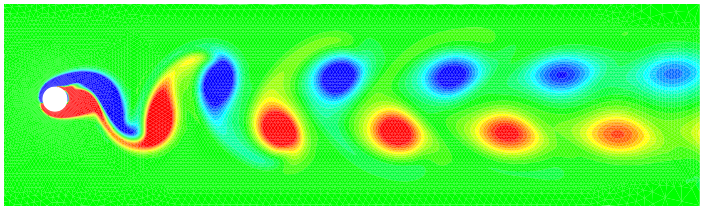

Fig. 7.8 Vorticity field at $Re = 100$

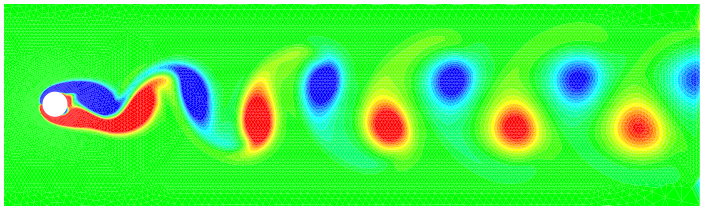

Fig. 7.9 Vorticity field at $Re = 120$

7.2 Free vibration of a circular cylinder

Two-degree-of-freedom oscillation of a flexible cylinder is excited by laminar flows, as shown in last section. The system parameters are set as [164]: $\hat{m} = 2.5\pi$, $\xi = 0$, $f_{\mathrm{r}} = 16.6/Re$, $60 \leqslant Re \leqslant 200$ and $\Delta t = 1.0 \times 10^{-2}$. The problem statement, FEM and MSA meshings are displayed in Figs. 7.1 and 7.2, respectively.

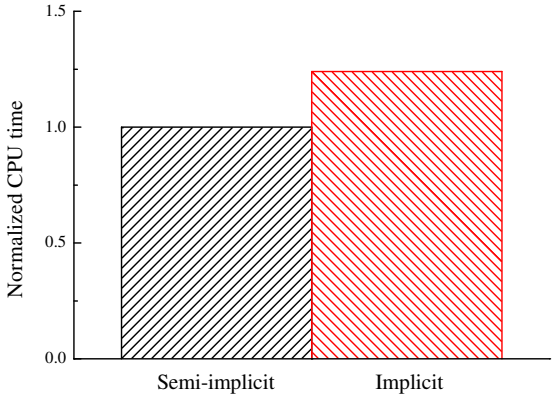

Fig. 7.10 Time consumption of the two coupling methods

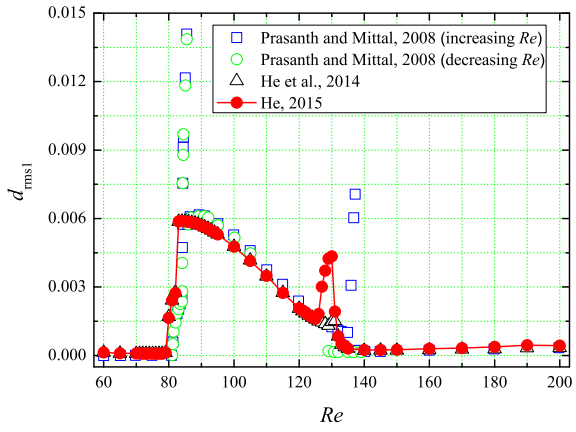

Fig. 7.11 Variation of RMS value of horizontal amplitude with Re

The preliminary study is performed via the $Re = 100$ flow. The obtained data are summarized in Table 7.4. Table 7.4 observes a good agreement among various data [164, 68, 36, 40]. The model problem is also used to examine the efficiency. Time consumptions of implicit and semi-implicit techniques are quantified by Fig. 7.10. It is seen that the former offers

Table 7.4 Comparison of computed results at $Re = 100$

Reference	d_{mean1}	d_{rms1}	d_{max2}	$C_{\text{d,mean}}$	$C_{\text{d,rms}}$	$C_{\text{l,max}}$	St
Prasanth and Mittal [164] (M7k)	0.1115	0.00494	0.516	1.90	0.2486	0.1929	0.1643
Prasanth and Mittal [164] (M15k)	0.1100	0.00484	0.503	1.88	0.2434	0.1900	0.1644
He et al. [68]	0.1082	0.00465	0.515	1.81	0.2244	0.1985	0.1652
He et al. [36] (implicit)	0.1075	0.00477	0.515	1.84	0.2388	0.1887	0.1644
He et al. [36] (semi-implicit)	0.1075	0.00477	0.515	1.84	0.2388	0.1869	0.1644
He [40]	0.1075	0.00477	0.515	1.84	0.2387	0.1870	0.1644

roughly 20% savings. In view of Table 7.4 and Fig. 7.10, the semi-implicit method seems more efficient than its implicit counterpart.

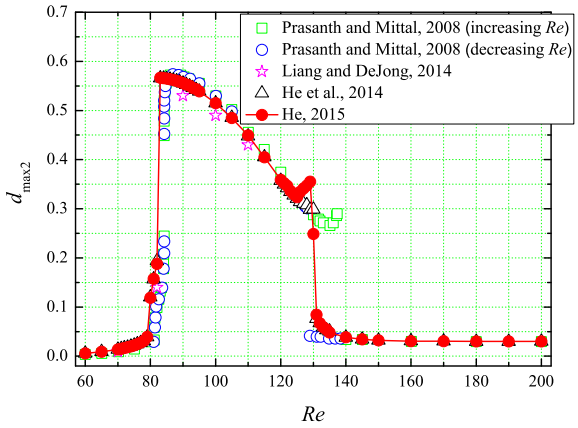

Fig. 7.12 Variation of peak of vertical amplitude with Re

Figs. 7.11 and 7.12 display the variation of d_{rms1} and d_{max2} of the cylinder with Re, respectively. In both pictures, lock-in takes place when $80 \leqslant Re \leqslant 130$ whereas the range in [164] is $81 \leqslant Re \leqslant 137$. Seen from Fig. 7.11, the horizontal oscillations are very weak, compared to the vertical oscillations. The d_{rms1} graph is similar to that of [164]. No peaks are seen near two ends. Possible reasons are given as: (i) the hysteretic effect is yet considered by altering Re; and (ii) the Re resolution is insufficient. The vertical amplitude is up to $0.566D$ in Fig. 7.12, larger than that of [175]. The graphs are accordant with those in [164] at the lower end. Near the upper end, a rebound occurs earlier in Fig. 7.11.

The force coefficients are shown in Figs. 7.13 and 7.14, respectively. The oscillating cylinder sustains larger fluid forces near the lower end. Peaks of force coefficients appear at $Re = 83$, identical with d_{rms1} and d_{max2}. The Re is about 88 in [164], later than the value computed here. The maximum $C_{\text{d,rms}}$ is approximately 0.4, identical to [164]. The rebound

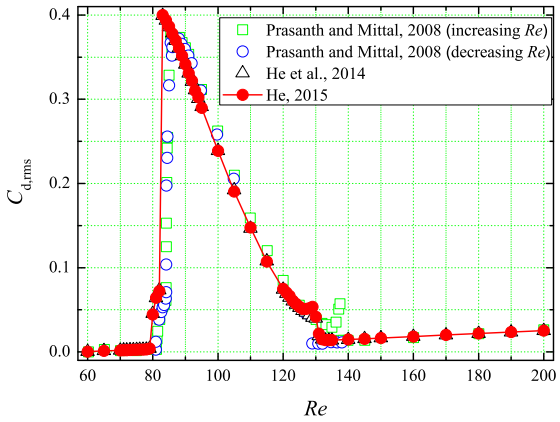

Fig. 7.13 Variation of RMS value of drag coefficient with *Re*

of $C_{\mathrm{d,rms}}$ is faint at the upper limit, but $C_{\mathrm{l,rms}}$ reaches a large scale therein. $C_{\mathrm{d,rms}}$ and $C_{\mathrm{l,rms}}$ go through a slow and smooth growth outside of the upper end.

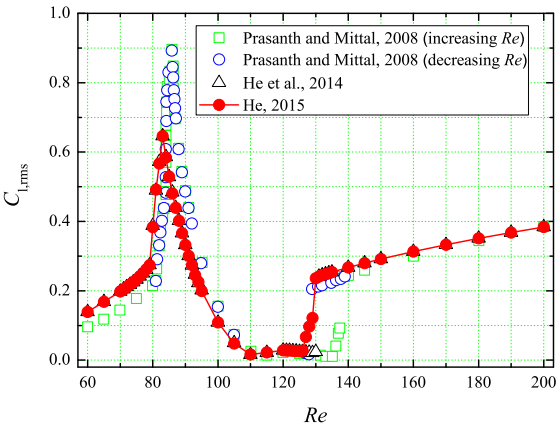

Fig. 7.14 Variation of RMS value of lift coefficient with *Re*

Figs. 7.15 and 7.16 illustrate the variation of *St* and $f_{\mathrm{v}}/f_{\mathrm{n}}$ with *Re*. *St* is strongly affected by *Re* and cylinder oscillations [164]. It is noted that during lock-in *St* deviates from the value for a rigid cylinder. Such a departure significantly reduces if *Re* is not in lock-in. In addition, an offset is observed between *St* and f_{r}. Prasanth and Mittal [164] give the main reason accounting for these phenomena. Fig. 7.16 witnesses two clear jumps of $f_{\mathrm{v}}/f_{\mathrm{n}}$. The first jump arises at $Re = 81$, equal to [164]. The second one takes place at $Re = 83$, earlier that [164]. These two jumps represent the so-called initial and lower branches, respectively

[176]. Figs. 7.11, 7.12, 7.15 and 7.16 apparently state that $81 \leqslant Re \leqslant 130$ is the current lock-in range.

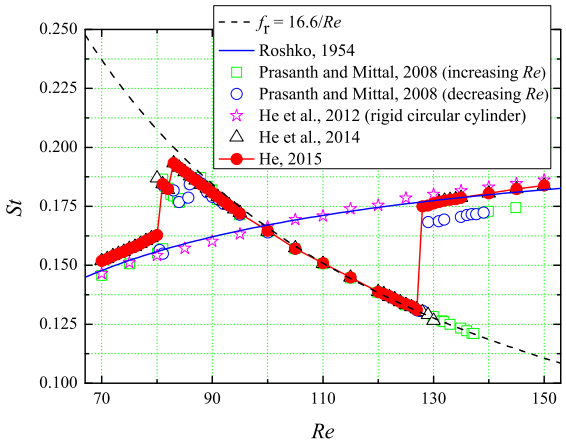

Fig. 7.15 Variation of Strouhal number with Re

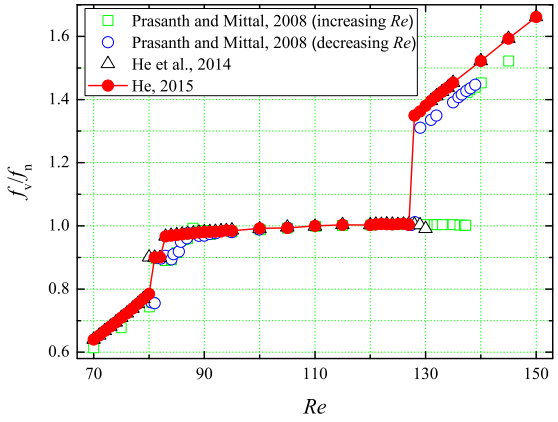

Fig. 7.16 Variation of frequency ratio with Re

Vorticity fields are plotted at two Re in Figs. 7.17 and 7.18. The 2S mode is obtained in Fig. 7.17 as $Re = 75$ inspires low-amplitude vibrations. Though high-amplitude vibrations take place at $Re = 90$, Fig. 7.18 does not witness the C(2S) vorticity street [117].

Next, an oscillating light cylinder due to uniform flows is computed by the semi-implicit method [40]. System properties are taken from [109]: $\hat{m} = 1.0$, $\xi = 3.42849 \times 10^{-3}$, $f_r = 0.24986$, $Re = 200$ and $\Delta t = 5.0 \times 10^{-3}$. 7040 points and 13870 T3 elements are used here. This mass ratio is mainly responsible for added-mass effect of a vibrating bluff body

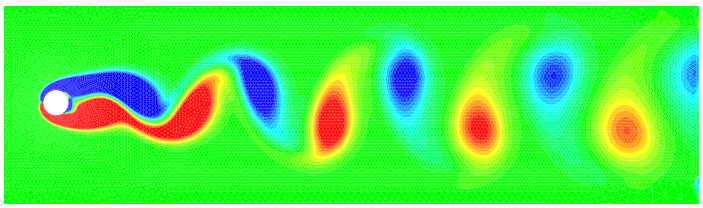

Fig. 7.17 Vorticity field at $Re = 75$

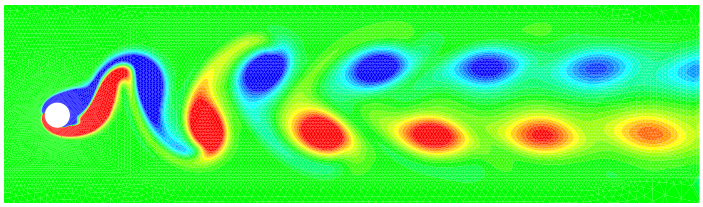

Fig. 7.18 Vorticity field at $Re = 90$

[50]. Fig. 7.19 plots the time evolution of force coefficients and cross-flow displacement, illustrating the feature similar to [109]. In Fig. 7.20 the spacing is enlarged between the shedding vortices, compared to a rigid cylinder.

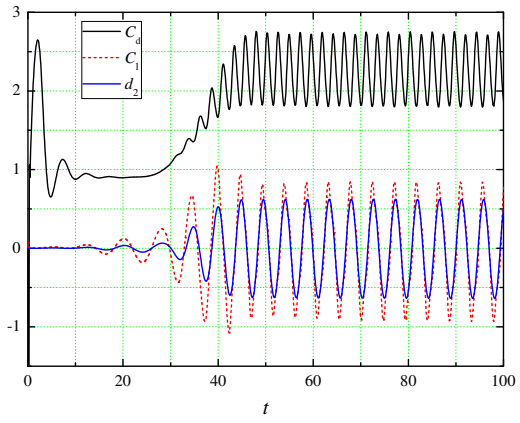

Fig. 7.19 Time curves of force coefficients and vertical amplitude

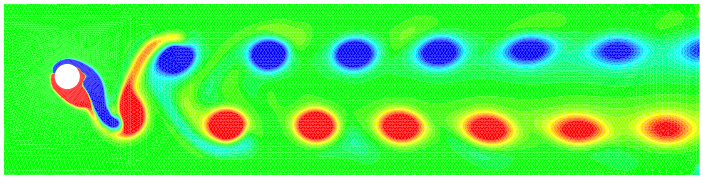

Fig. 7.20 Vorticity contour

7.3 Cross-flow vibration of a square cylinder

The present problem analyzes a transversely vibrating square cylinder for different Re in Fig. 7.21. The parameter conditions are given as [177, 136]: $\hat{m}_2 = 20$, $\xi_2 = 3.7 \times 10^{-3}$, $f_{r2} = 6.25/Re$, $40 \leqslant Re \leqslant 250$ and $\Delta t = 2.0 \times 10^{-2}$. Lock-in and *galloping* will be aroused in the Re range considered. For a non-circular cross section bluff body, galloping is triggered if the incoming velocity exceeds a critical value [178].

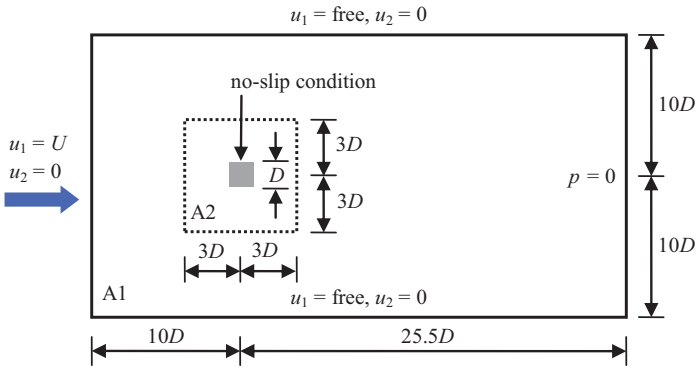

Fig. 7.21 Sketch of the transversely vibrating square cylinder

The fluid domain is divided into A1 and A2 subdomains. Fig. 7.22a encompasses 4061 points and 7932 T3 elements and Fig. 7.22b shows the corresponding submesh.

The $Re = 250$ flow is first analyzed for validation, whose results are summarized and compared in Table 7.5. The explicit scheme in [68] produces the a little larger amplitude but the oscillation frequency remains unchanged. Galloping is fairly activated at this Re. In short, Table 7.5 visualizes the good agreement observed among different approaches.

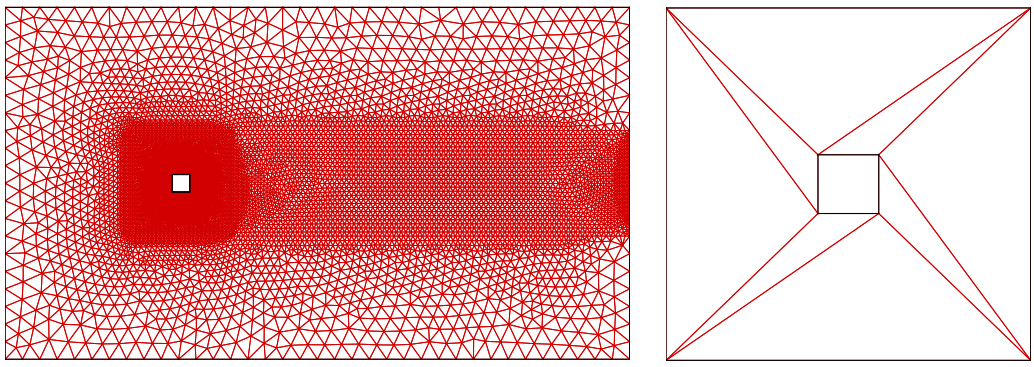

(a) FE mesh for fluid domain **(b)** Submesh for ALE domain

Fig. 7.22 Finite element mesh and MSA submesh

Table 7.5 Comparison of numerical results at $Re = 250$

Reference	d_{mean2}	$f_{\text{v}}/f_{\text{n}}$	$f_{\text{o}}/f_{\text{n}}$
Robertson et al. [177]	1.15	–	0.938
Dettmer and Perić [136]	1.117	6.33	0.943
He et al. [68]	1.2789	6.3672	0.9516
He et al. [36]	1.1596	6.5252	0.9392
He [69]	1.1475	6.4404	0.9516

To take into account the *Re* effect, Figs. 7.23 and 7.24 analyzes the amplitude and two frequency ratios at various *Re*. Overall, the good agreement is revealed among [136, 36, 69] by the pictures. Both lock-in and galloping are evidently captured by Fig. 7.23. Lock-in spans $48 \leqslant Re \leqslant 55$ in this study. The maximum amplitude is 0.23 at $Re = 48$ whereas in [136] the value is 0.186 at $Re = 50$. In quasi-steady theory, the lower limit of *Re* depends upon polynomial coefficients for activating the onset of galloping, but multiple values are possible [179]. For instance, the limit is 158.8 in [179] or 140.3 in [180] for remarkably low elastic properties. However, the critical *Re* is approximately 159.5 or 140.9 in the present case, if the elastic properties are considered. In Fig. 7.24, $f_{\text{v}}/f_{\text{n2}}$ approaches to 1 during the lock-in, but it keeps on ascending as *Re* increases. $f_{\text{o}}/f_{\text{n2}}$ becomes close to 1 once galloping is activated. In this case, $f_{\text{v}}/f_{\text{n2}}$ and the displacement will reach a high level.

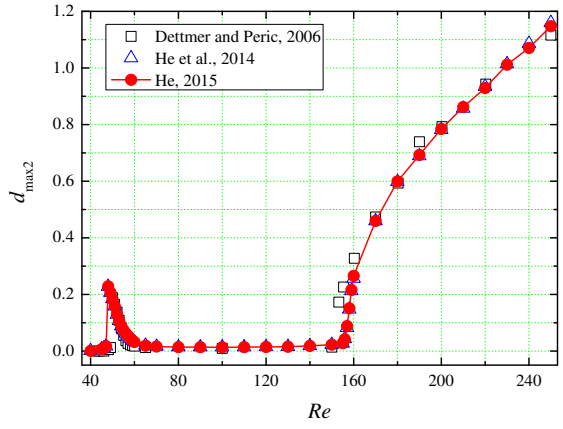

Fig. 7.23 Variation of the cylinder amplitude with *Re*

Figs. 7.25–7.27 plot the displacement histories at $Re = 48,\ 100,$ and 250, respectively. The relevant flow patterns at these *Re* are exhibited in Figs. 7.28–7.30. The vortex-shedding modes are of 2S types at $Re = 48$ and 100. The flow pattern is 2S mode at $Re = 250$ that stimulates galloping. The longitudinal spacing between vortices increases in the third

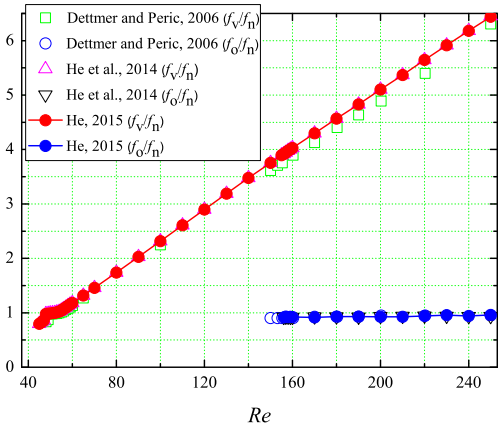

Fig. 7.24 Variation of two frequency ratios with Re

picture, though it decreases near the wake. $Re = 100$ does not inspire lock-in nor galloping, where the vortex looks like that behind the rigid cylinder. For aspect ratio $\Lambda = 1.5$, the numerical analysis is reported in [177].

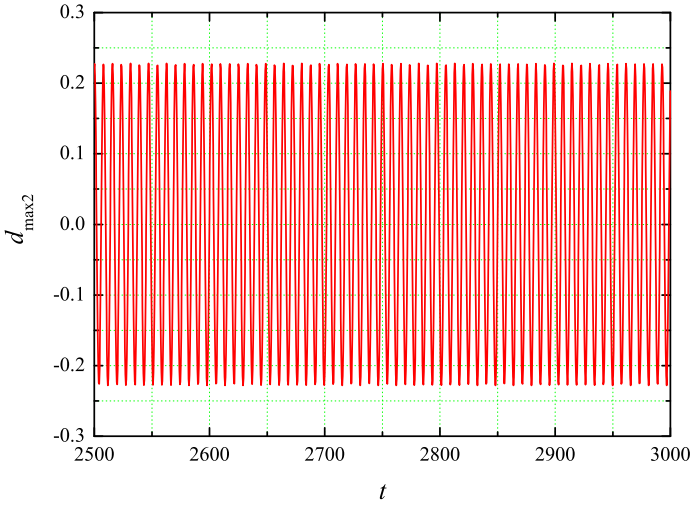

Fig. 7.25 Time history of displacement at $Re = 48$

7.4 Free vibration of a square cylinder

The current section is devoted to free vibrations of a square cylinder. The geometry is identical to last section. System parameters are defined as [181]: $\hat{m} = 10$, $\xi = 0$, $f_r =$

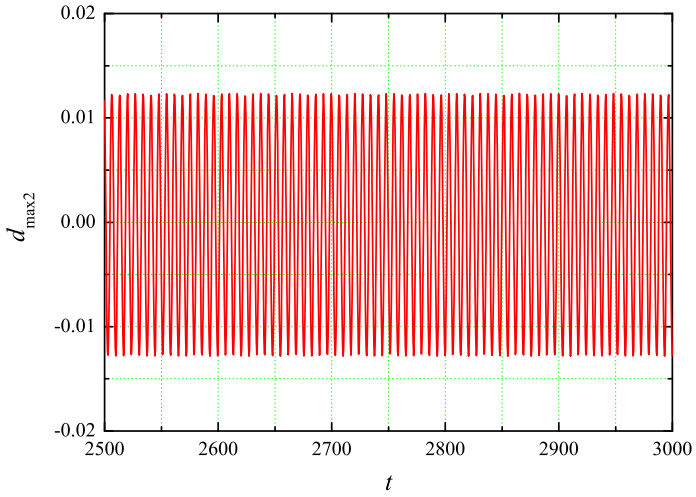

Fig. 7.26 Time history of displacement at $Re = 100$

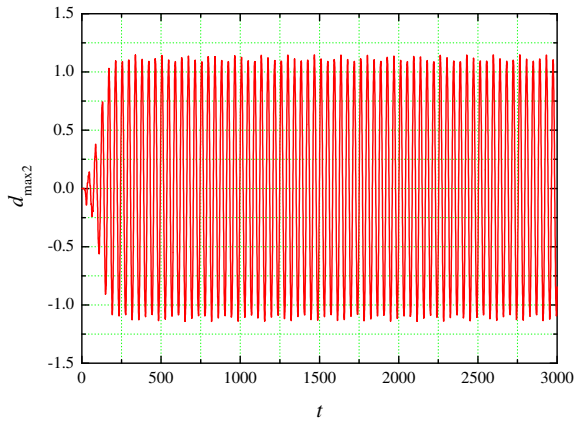

Fig. 7.27 Time history of displacement at $Re = 250$

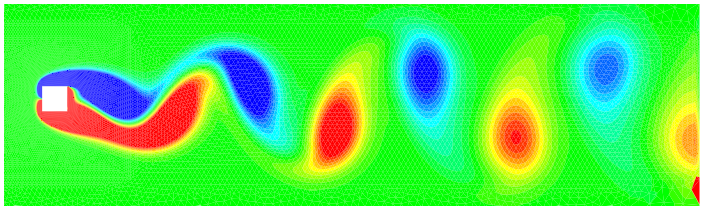

Fig. 7.28 Vorticity field at $Re = 48$

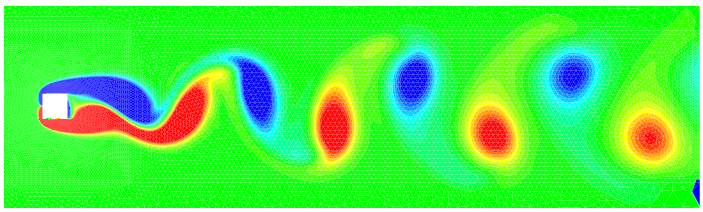

Fig. 7.29 Vorticity field at $Re = 100$

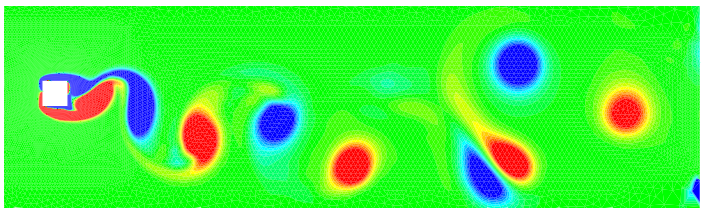

Fig. 7.30 Vorticity field at $Re = 250$

$14.39/Re$, $60 \leqslant Re \leqslant 250$ and $\Delta t = 2.0 \times 10^{-2}$. The fluid discretization is made up of 8232 points and 16254 T3 elements.

The $Re = 90$ flow is simulated first for validation, as compared in Table 7.6. In comparison with Sen and Mittal [181], the developed coupling methods produce the larger $C_{\mathrm{d,mean}}$ but smaller $C_{\mathrm{l,rms}}$. The agreement is however realized in Table 7.6.

Figs. 7.31–7.36 displays the variation of different parameters of the vibrating cylinder with Re, respectively. It is clearly observed that lock-in and galloping take place here.

The cylinder displacement is shown in Figs. 7.31 and 7.32. In general, the tiny deviation is seen among all data. The variation trend in two pictures is dominated by lock-in and galloping largely. In [181] the latter is named *secondary lock-in*. In Fig. 7.31 d_{rms1} is hardly visible before galloping occurs, while in Fig. 7.32 d_{max2} foresees lock-in. The maximum transverse amplitude is listed in Table 7.7 in the lock-in and galloping regions, demonstrating a good agreement between published and obtained results. During lock-in, d_{max2} seems

Table 7.6 Summary of numerical results at $Re = 90$

Reference	d_{mean1}	d_{rms1}	d_{max2}	d_{rms2}	$C_{\mathrm{d,mean}}$	$C_{\mathrm{d,rms}}$	$C_{\mathrm{l,max}}$	St
Sen and Mittal [181] (M1)	0.0907	0.0014	0.1843	0.1303	1.7917	0.0790	0.1082	0.1566
Sen and Mittal [181] (M2)	0.0906	0.0014	0.1822	0.1288	1.7882	0.0779	0.1026	0.1568
He et al. [68]	0.0959	0.0016	0.1998	0.1411	1.8831	0.0953	0.0687	0.1580
He et al. [36]	0.0946	0.00155	0.1970	0.1391	1.8650	0.0905	0.0822	0.1574
He [69]	0.0946	0.00155	0.1973	0.1393	1.8657	0.0907	0.0824	0.1574

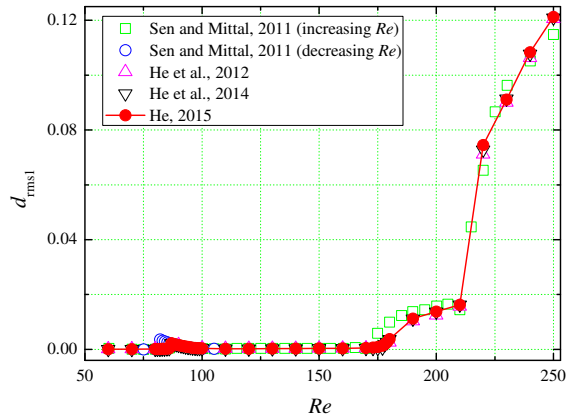

Fig. 7.31 Variation of RMS value of horizontal amplitude with *Re*

closer to the value obtained by increasing *Re* [181]. Meanwhile, d_{max2} reported in [181] is half the value for the flexible circular cylinder [164], but the number is 41.6% herein. The amplitude peak is shown in Fig. 7.32. The partitioned explicit scheme evaluates somewhat larger amplitude when $100 \leqslant Re \leqslant 200$ [68]. It is seen that the second displacement jump happens at $Re = 220$. Namely, galloping is waken once $Re \geqslant 220$ under the given conditions. Galloping increases the displacement significantly since *Re* keeps on raising. This is because the galloping instability is cause by the so-called negative aerodynamic damping [182].

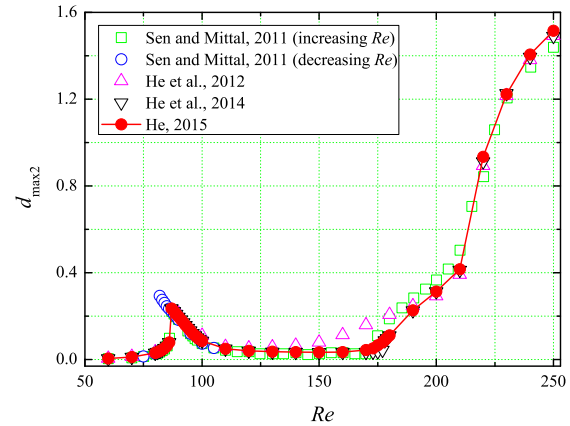

Fig. 7.32 Variation of vertical amplitude with *Re*

$C_{d,mean}$ and $C_{l,rms}$ are displayed in Figs. 7.33 and 7.34, respectively. $C_{d,mean}$ is larger than that of [181] if *Re* is outside of the galloping range, seen from Fig. 7.33. In Fig. 7.34, this

Table 7.7 Vertical amplitude and Re

Reference	Phenomenon	$d_{\max 2}$	Re
Sen and Mittal [181]	Lock-in	0.22/0.29	82/87
	Galloping	1.44	250
He et al. [68]	Lock-in	0.2127	90
	Galloping	1.4923	250
He et al. [36]	Lock-in	0.2353	87
	Galloping	1.4923	250
He [69]	Lock-in	0.2353	87
	Galloping	1.5148	250

situation happens to $C_{\mathrm{l,rms}}$ if $105 \leqslant Re \leqslant 180$. The two curves jump at $Re = 87$, as the same as the variations of the amplitude. The $C_{\mathrm{d,mean}}$ curve shows the first jump at the same Re, as reported in [181]. In Fig. 7.33 $C_{\mathrm{d,mean}}$ slowly climb after a steep drop prior to galloping. It is seen that $C_{\mathrm{l,rms}}$ ascends at $Re = 96$ in Fig. 7.34. Galloping thus causes high-level growth of $C_{\mathrm{d,mean}}$ and $C_{\mathrm{l,rms}}$. $C_{\mathrm{d,mean}}$ decreases slowly and $C_{\mathrm{l,rms}}$ experiences the smooth drop, when Re increases further.

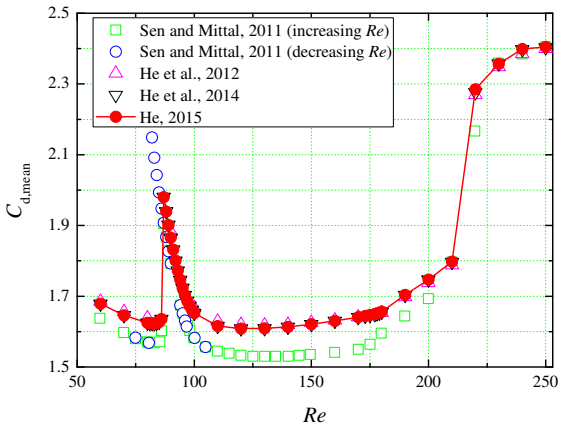

Fig. 7.33 Variation of mean drag coefficient with Re

f_{o} vs. Re is presented in Fig. 7.35, including St for the fixed square cylinder [68, 116] and f_{r}. Lock-in is the first jump that activates at $Re = 87$ and ends at $Re = 100$. While $100 < Re \leqslant 130$, f_{o} approaches to St of a rigid cylinder. Galloping is slightly later than that [181], being motivated from $Re = 179$. Identical to [181], f_{o} experiences a smooth fall after a second decline, and it is close to f_{r}. It is reported in [181] that the lock-in scope is nearly a third of that for the oscillating circular cylinder [164], as confirmed in [36, 69]. $f_{\mathrm{o}}/f_{\mathrm{n}}$ vs. Re

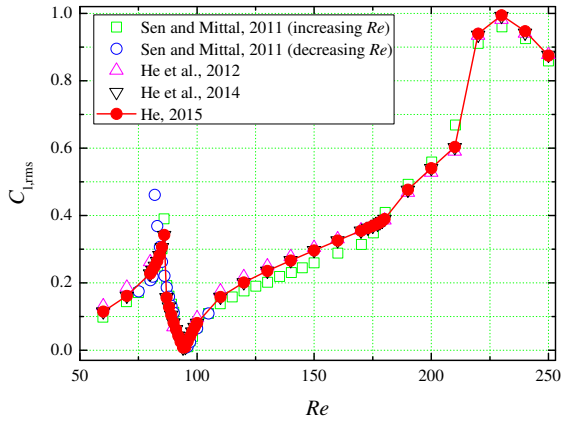

Fig. 7.34 Variation of RMS value of lift coefficient with Re

is illustrated by Fig. 7.36. The ratio is rising until $Re = 178$, and it goes through an abrupt fall then. For $179 \leqslant Re \leqslant 250$, $f_\mathrm{o}/f_\mathrm{n}$ suggests that the galloping appears.

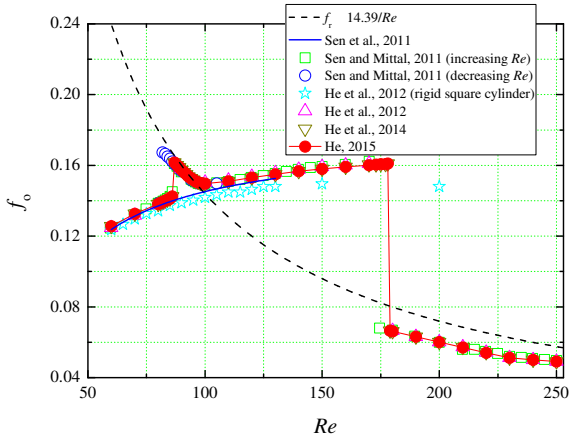

Fig. 7.35 Variation of oscillation frequency with Re

Vortex-shedding modes are plotted for various Re in Figs. 7.37–7.40, respectively. In Fig. 7.37, the cylinder undergoes violent oscillations at $Re = 87$. The mode is 2S rather than C(2S) [117], unlike [181]. Fig. 7.38 indicates that the spacing between shedding vortices decreases at $Re = 150$. The resulting flow pattern is quite similar to the rigid cylinder. Identical to [181], the 2P mode [117] appears for $Re \geqslant 215$ in Fig. 7.39, but [68] reports the mode like the Y-only motion [181]. Fig. 7.40 indicates that the vortex shedding at $Re = 250$ is similar to that at $Re = 230$.

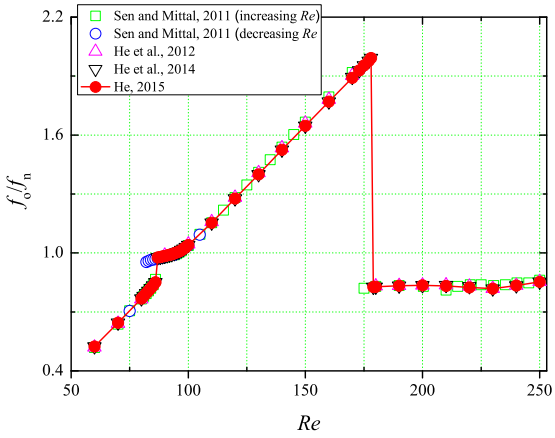

Fig. 7.36 Variation of frequency ratio with Re

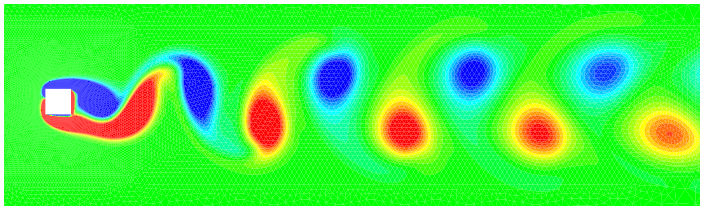

Fig. 7.37 Vorticity field at $Re = 87$

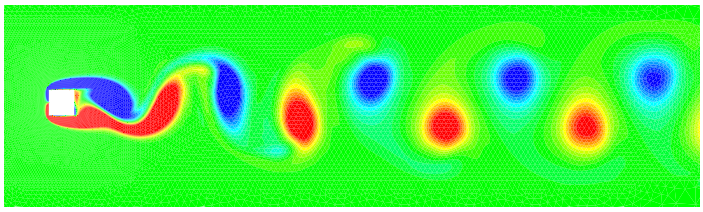

Fig. 7.38 Vorticity field at $Re = 150$

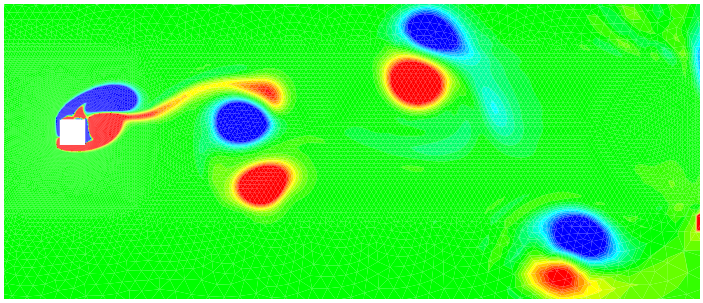

Fig. 7.39 Vorticity field at $Re = 230$

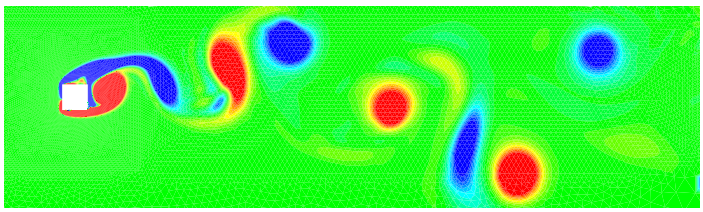

Fig. 7.40 Vorticity field at $Re = 250$

Table 7.8 Comparison of computed results

Reference	$\theta_{\max}$	St	f_v/f_n	f_o/f_n
Robertson et al. [177]	0.262	–	–	0.762
Dettmer and Perić [136]	0.267	0.13	5.2	0.8
He et al. [36]	0.3122	0.1409	5.6364	0.8052
He [69]	0.3128	0.1409	5.6364	0.8052

7.5 Rotations of a rectangular cylinder

The present section calculates flows over a rotating rectangular cylinder in Fig. 7.41. The cylinder's height and depth are designated as $D = 1$ and $B = 4$, respectively. System parameters are [136, 177]: $\hat{m}_\theta = 400$, $\xi_\theta = 0.25$, $f_{r\theta} = 6.25/Re$, $Re = 250$ and $\Delta t = 4.0 \times 10^{-2}$. The finite mesh (4089 points and 7988 T3 elements) and submesh are illustrated in Fig. 7.42.

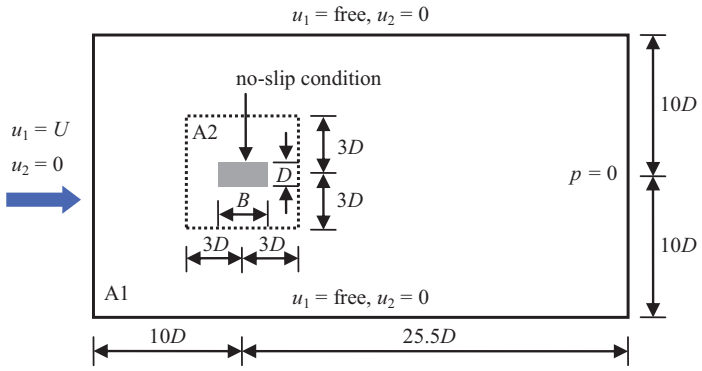

Fig. 7.41 Sketch of the rotating rectangular cylinder

Numerical parameters compared to available data [136, 36, 69, 177] are listed in Table 7.8. An accepted agreement is revealed from this table. Fig. 7.43 plots the time evolution of torsion and the vorticity contour is showed in Fig. 7.44. The above results demonstrate that the torsional galloping is inspired based upon the developed schemes.

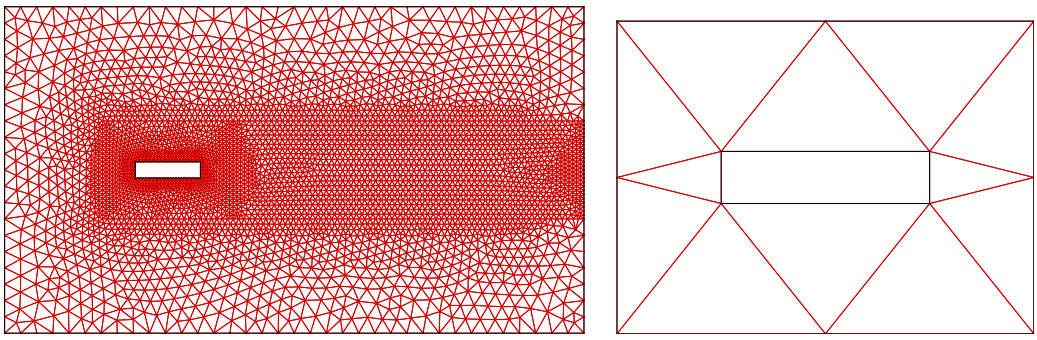

(a) FE mesh for fluid domain **(b)** Submesh for ALE domain

Fig. 7.42 Finite element mesh and MSA submesh

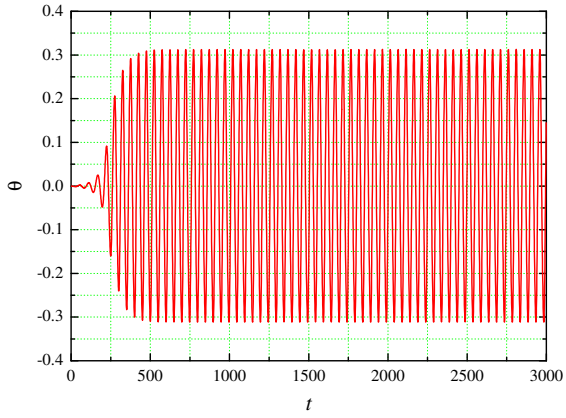

Fig. 7.43 Time history of the rotation

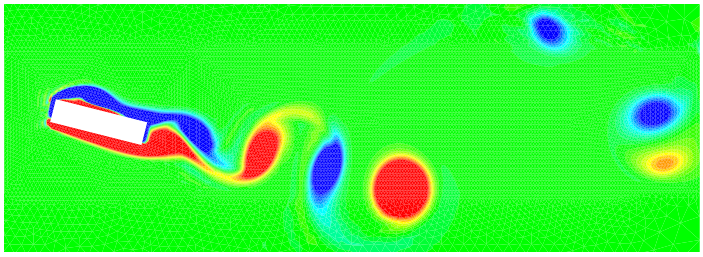

Fig. 7.44 Vorticity contour

7.6 Flutter of a flexible bridge deck

An H-shaped deck mounted with vertical and torsional springs goes through both translation and rotation. Such a problem is presented to demonstrate the flutter failure of Tacoma Narrows Bridge [183]. The vortex shedding is essential to the system behavior and nearly independent of *Re* which is unrealistic, though.

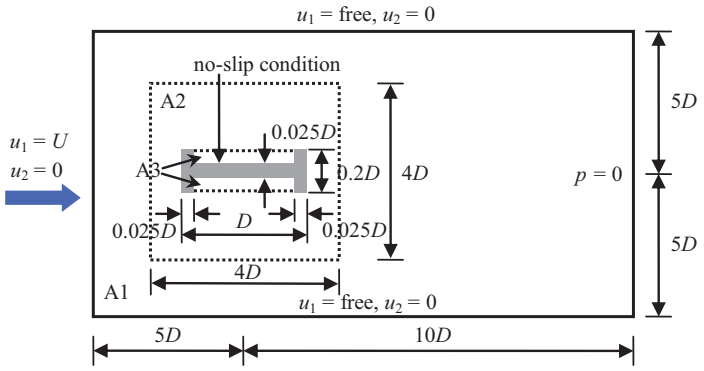

Fig. 7.45 Sketch of the oscillating bridge deck

The problem is defined in Fig. 7.45 and its properties are given as [184]: $\rho^{\mathrm{f}} = 1.25$, $\mu = 0.1$, $m_2 = 3000$, $m_\theta = 25300$, $c_2 = 100$, $c_\theta = 2200$, $k_2 = 2000$, $k_\theta = 40000$, $U = 10$, $D = 12$, $f_{\mathrm{n}2} = 0.1299$ and $f_{\mathrm{n}\theta} = 0.2001$. Other parameters are calculated as: $f_{\mathrm{r}2} = 0.1559$, $f_{\mathrm{r}\theta} = 0.2401$, $\xi_2 = 2.041 \times 10^{-2}$, $\xi_\theta = 3.458 \times 10^{-2}$, $\hat{m}_2 = 16.667$, $\hat{m}_\theta = 0.976$, $Re = 1500$ and $\Delta t = 2.0 \times 10^{-2}$. In Fig. 7.46a the mesh is made up of 3329 points and 6486 T3 elements, and Fig. 7.46b plots the submesh.

The simple geometry never means that comparable data are gained in different researches. The data from [183, 185, 186, 136, 22] remarkably change for null damping. It is seen that, Cebral and Löhner [186] obtained the very small rotation but the large amplitude is gained in [136]. It is noticed in [183] that the simulation even ceases at $t = 55s$. Table 7.9 summarizes $d_{\max 2}$, $f_{\mathrm{o}2}$, $\theta_{\max}$ and $f_{\mathrm{o}\theta}$. It demonstrates that, both amplitudes are larger than those of [184] but almost equal to the data in [83, 39]. In all cases except [184], the oscillation frequency perfectly agrees with its rotational counterpart. Owing to the complexity of flutter, the distinction in translation and torsion is acceptable among available papers. The power spectra applied to the rotation [39] is displayed in Fig. 7.47.

Fig. 7.48 displays the time curves of the two displacement components. A stable pattern of the oscillations very is seen soon. In view of Fig. 7.48 and Table 7.9, the rotational frequency approaches to its natural frequency while the oscillations are significantly week in the vertical direction. The rotation seems the dominant motion, clearly identifying flutter.

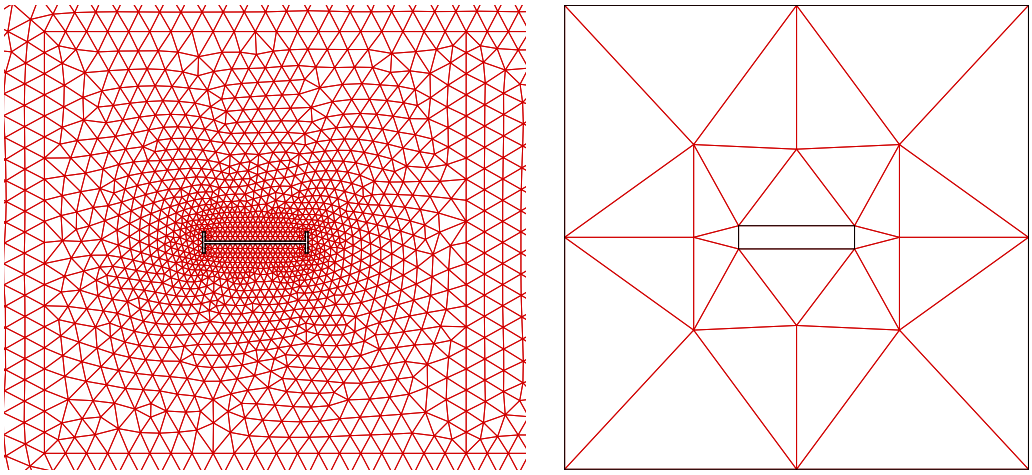

(a) FE mesh for fluid domain **(b)** Submesh for ALE domain

Fig. 7.46 Finite element mesh and MSA submesh

Table 7.9 Comparison of computed results

Reference	$d_{\max 2}$	f_{o2}	$\theta_{\max}$	$f_{o\theta}$
Filippini et al. [184]	$0.0325 \sim 0.035$	–	0.271	–
He [83]	0.0407	0.2136	0.385	0.2136
He and Zhang [39]	0.0434	0.2087	0.398	0.2087

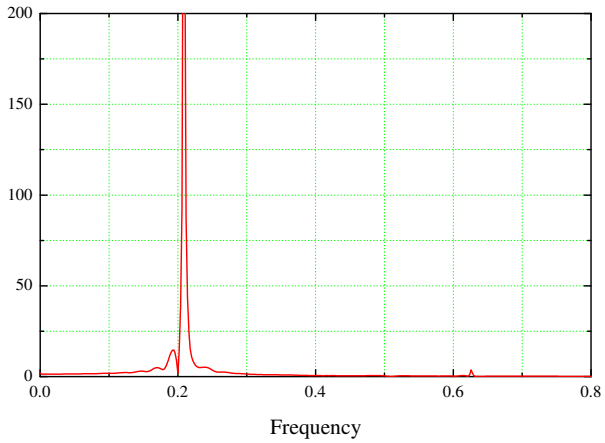

Fig. 7.47 Power spectra of the rotation

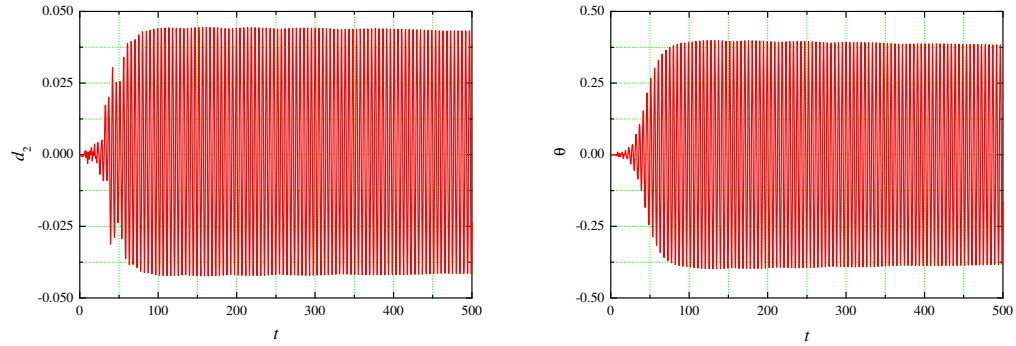

(a) Vertical component **(b)** Rotational component

Fig. 7.48 Time history of the deck displacement

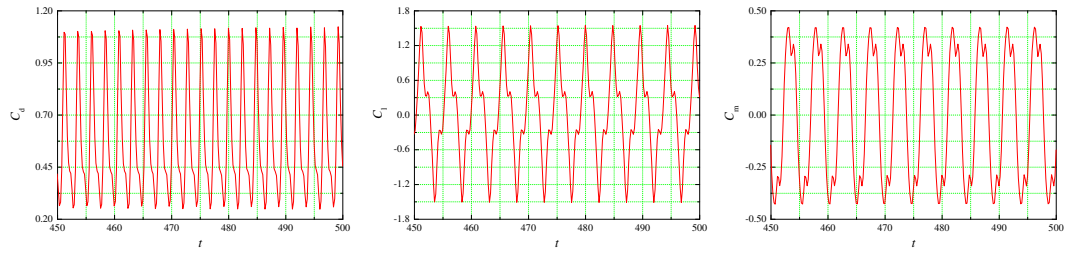

(a) Drag coefficient **(b)** Lift coefficient **(c)** Moment coefficient

Fig. 7.49 Time history of force coefficients

Normally, vibrating bluff bodies shed wake vorticities at oscillation and *St* frequencies. The former dominates strong oscillations [187]. The identical conclusion is drawn by Lee *et al.* [188]. Fig. 7.49 establishes the time evolution of force coefficients. Besides, similar fluid forces are presented in [183]. In what follows, a vorticity contour is typically shown in Fig. 7.50. It is fairly seen that the vortex pattern fully agrees with the previous explanation [187].

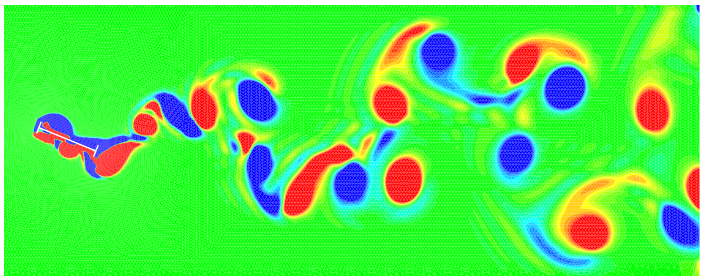

Fig. 7.50 Vorticity field of the deck

Table 7.10 Meshing information

Subproblem	Item	Case 1	Case 2
Fluid	Element	T3	T3
	Number of elements	8789	13962
	Number of points	4508	7155
Solid	Element	Q9	Q4
	Number of elements	20×1	80×2
	Number of points	123	243
MSA	Element	T3	T3
	Number of elements	245	481
	Number of points	171	329

7.7 A cantilever behind a square obstacle

The benchmarking is proposed in [3] to test the capability of a coupling algorithm, as illustrated by Fig. 7.51. The physical parameters are given by [3]: $\rho^{\mathrm{f}} = 1.18 \times 10^{-3}$, $\rho^{\mathrm{s}} = 1.0 \times 10^{-1}$, $\mu = 1.82 \times 10^{-4}$, $E = 2.5 \times 10^{6}$, $\nu = 0.35$, $D = 1$, $U = 51.3$ and $Re = 332.6$.

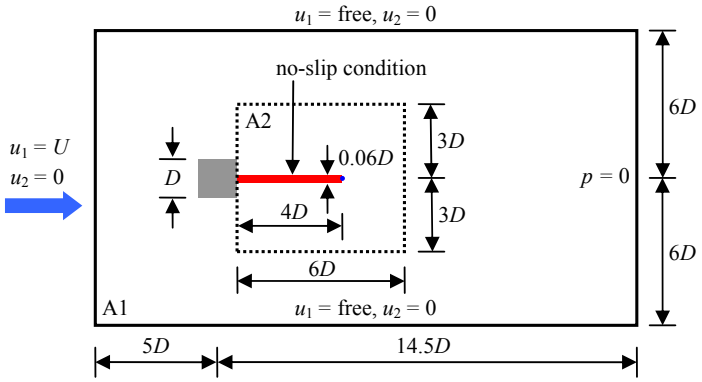

Fig. 7.51 Sketch of the beam behind an obstacle

The beam is meshed into Q4 or Q9 elements for the CS-FEM and FEM. Table 7.10 summarizes the meshing information and Fig. 7.52 shows the fluid mesh and submesh. $\Delta t = 1.0 \times 10^{-2}$ and $tol = 1.0 \times 10^{-6}$, $\beta = 0.5$ and $\gamma = 0.8$ are chosen herein.

Table 7.11 lists d_{mean2} and $f_{\mathrm{o,mean}}$ as well as the documented data [3, 183, 161, 189, 137, 190–192, 124, 193–195]. The data in Case 1 are the same as most available data. $d_{\mathrm{mean2}} = 0.92$ is still acceptable in Case 2, compared to [183, 193, 195]. $f_{\mathrm{o,mean}} = 0.0586$ and $f_{\mathrm{o,mean}} = 0.0622$ in the two cases are close to $f_1^{\mathrm{s}} = 0.0591$. Therefore, a reasonable agreement is gained from Table 7.11. The table and Fig. 7.53 demonstrate that, the semi-implicit scheme leads to the improved efficiency, particularly for the tight tolerance.

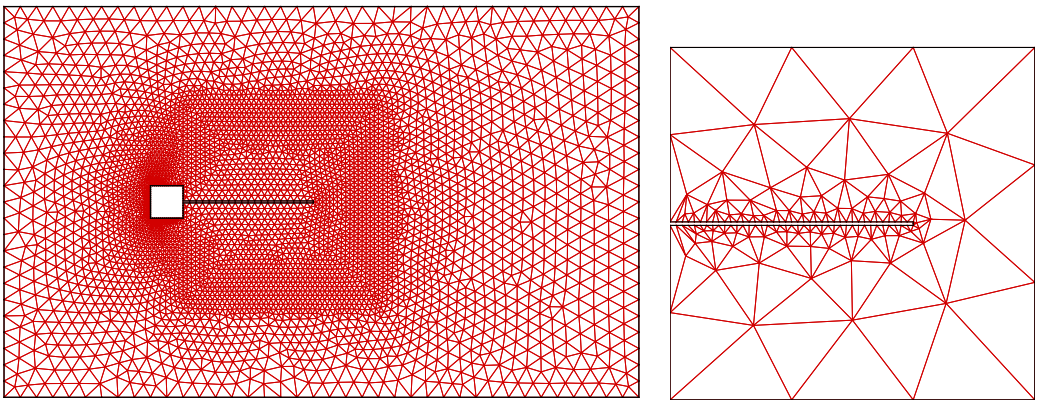

(a) FE mesh for fluid domain **(b)** Submesh for ALE domain

Fig. 7.52 Finite element mesh and MSA submesh

Table 7.11 Comparison of previous and present results

Reference	Dimension	Algorithm	d_{mean2}	$f_{\text{o,mean}}$
Wall and Ramm [3]	Two	Explicit	1.20	0.0604
Hübner et al. [183]	Two	Monolithic	1.08	0.0615
Matthies and Steindorf [161]	Two	Implicit	1.18	0.0610
Teixeira and Awruch [189]	Three	Explicit	1.35	0.0584
Dettmer and Perić [137]	Two	Implicit	1.25	0.0634
Liew et al. [190]	Two	Monolithic	1.34	0.0609
Yamada and Yoshimura [191]	Two	Implicit	1.19	0.0624
Bazilevs et al. [192]	Two	Monolithic	1.21	0.0591
Braun and Awruch [124]	Three	Explicit	$1.181 \sim 1.215$	0.0591
Olivier et al. [193]	Two	Implicit	0.95	0.0618
Wood et al. [194]	Three	Implicit	1.15	0.0573
Habchi et al. [195]	Two	Implicit	1.02	0.0634
He [40] (FEM)	Two	Semi-implicit	1.25	0.0586
He [40] (SFEM)	Two	Semi-implicit	0.92	0.0622

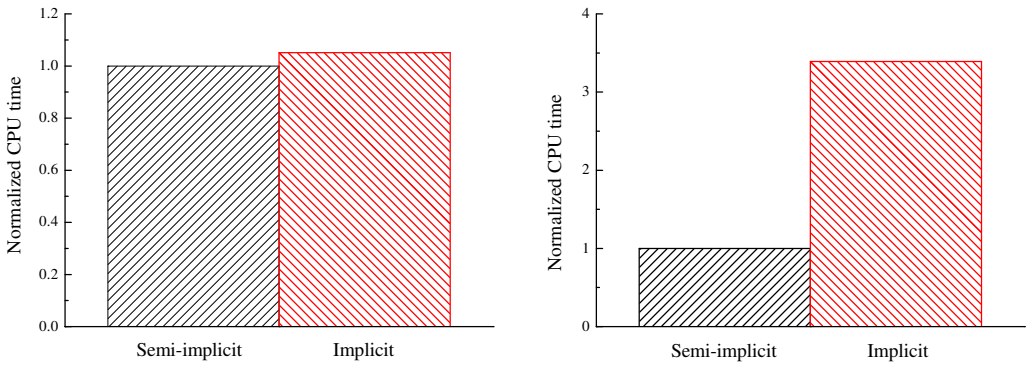

(a) $tol = 1.0 \times 10^{-6}$ **(b)** $tol = 1.0 \times 10^{-7}$

Fig. 7.53 Time consumption of two coupling methods

Figs. 7.54 and 7.55 show the time evolution of tip displacement in the two cases. It is seen that the periodic structural vibrations are established correctly. According to [137, 191], the structural motion commences at $t = 100$. However, the structural response was set up much later in [190]. In view of these two pictures, the first amplitude is lager than the second one, and shorter period is demanded to achieve the amplitude. The underestimated deflection may result from the insufficient Q4 elements and the linear interpolation. It is noticed that [193, 195] produce very small amplitudes, even through denser elements are used for the solid.

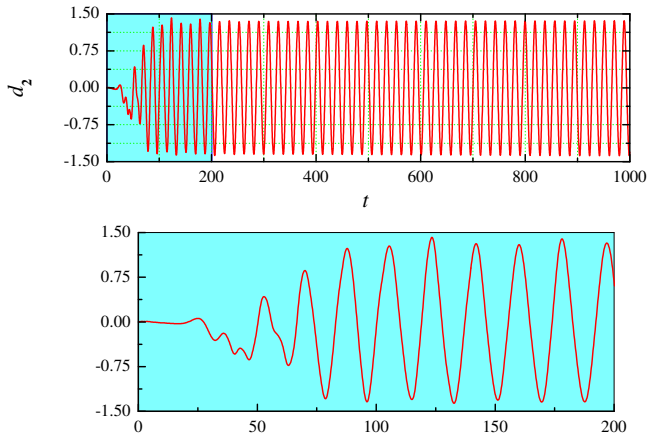

Fig. 7.54 Time history of vertical displacement in Case 1

The obtained time history contains lock-in and beating in the above two figures [190]. At the first stage the tip displacement is amplified gradually. Besides, the oscillation frequency

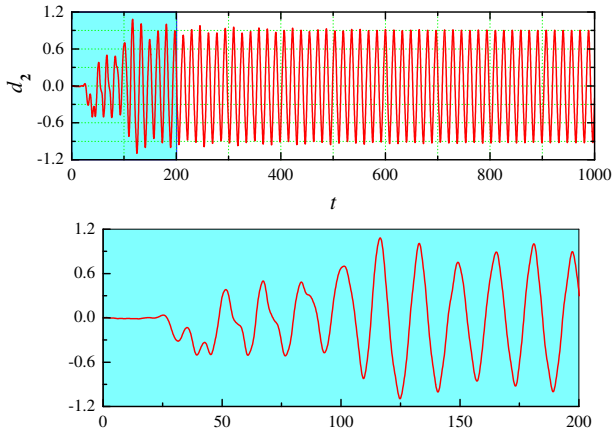

Fig. 7.55 Time history of vertical displacement in Case 2

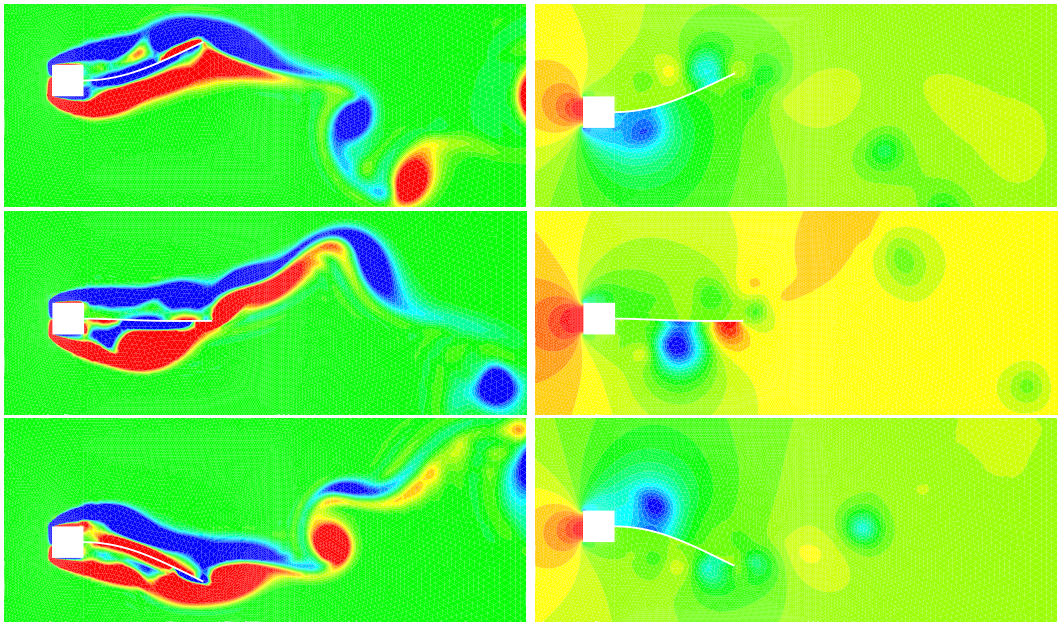

(a) Vorticity **(b)** Pressure

Fig. 7.56 Instantaneous contours of the beam

rather approaches to the first eigenfrequency. The beam response converges to the stable motion at the other stage. Accordingly, the strong vibrations alter flow pattern significantly and its frequency also departs from the first eigenfrequency.

Three snapshots during stable vibrations are depicted in Fig. 7.56 for vorticity and pressure. The flow patterns and beam deflection vary in one oscillation period. The alternatively shedding vortices act on the structural surface in Fig. 7.56a, motivating strong oscillations. The vortices on one side towards which the beam moves are weakened, and in the meatime they are suppressed by the flows nearby and high compression is observed. Howbeit, vortices are strengthened on the opposite side, and further are advecting downstream. The pressure distribution is positive on the frontal side in Fig. 7.56b, since the obstacle is immediately exposed to the flows. The resulting suction is high along lateral sides. With lower suction, the surface pressure distribution is negative opposite to the motion direction.

7.8 A flexible flap subjected to channel flows

The final problem is dedicated to a vibrating flap [193], as pictured in Fig. 7.57. The problem properties are prescribed as: $\rho^{\mathrm{f}} = 1.0$, $\mu = 1.0 \times 10^{-3}$, $\rho^{\mathrm{s}} = 1000$ (Case A therein), $E = 6.0 \times 10^{4}$, $\nu = 0.45$, $U = 1$, $D = 1$ and $Re = 1000$. The flap is meshed with Q8 elements and Table 7.12 lists all mesh information. For Mesh 1, the mesh and submesh are shown in Fig. 7.58. $\Delta t = 5.0 \times 10^{-3}$, $tol = 1.0 \times 10^{-6}$, $\beta = 0.5$ and $\gamma = 0.8$ are adopted here.

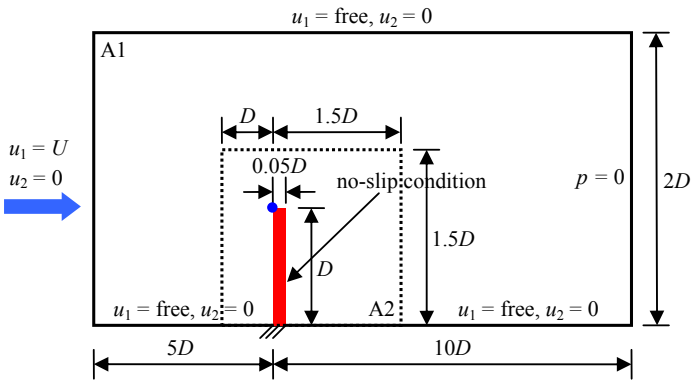

Fig. 7.57 Sketch of the restrictor flap in a channel

Fig. 7.59 depicts the displacement curve in the horizontal direction. The computed magnitudes of tip deflection using two different methods are nearly 0.6, which agree with [193]. The flap motion is excited largely through the structural inertia, if the structural density is rather large. On this occasion, the fluid is deemed to be the damped oscillator. However, the

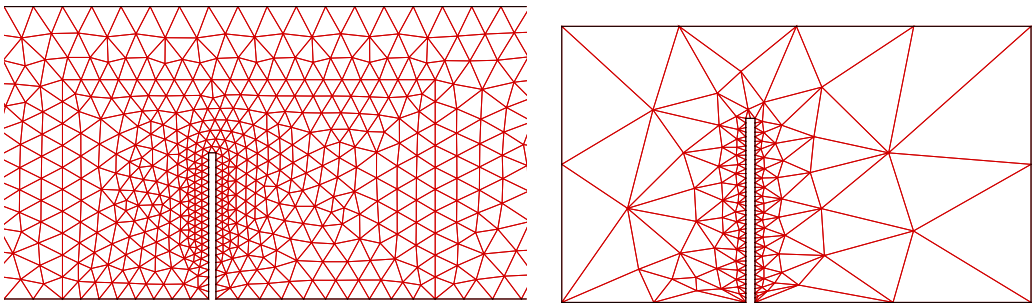

(a) FE mesh for fluid domain **(b)** Submesh for ALE domain

Fig. 7.58 Finite element mesh and MSA submesh

Table 7.12 Meshing information

Subproblem	Item	Mesh 1	Mesh 2
Fluid	Element	T3	T3
	Number of elements	2301	2786
	Number of points	1260	1523
Solid	Element	Q8	Q4
	Number of elements	20×1	40×2
	Number of points	103	123
MSA	Element	T3	T3
	Number of elements	258	258
	Number of points	177	177

flap motion may be sharply damped by the viscous fluid if the structural density decreases [196]. Fig. 7.60 plots different horizontal velocity contours in the case.

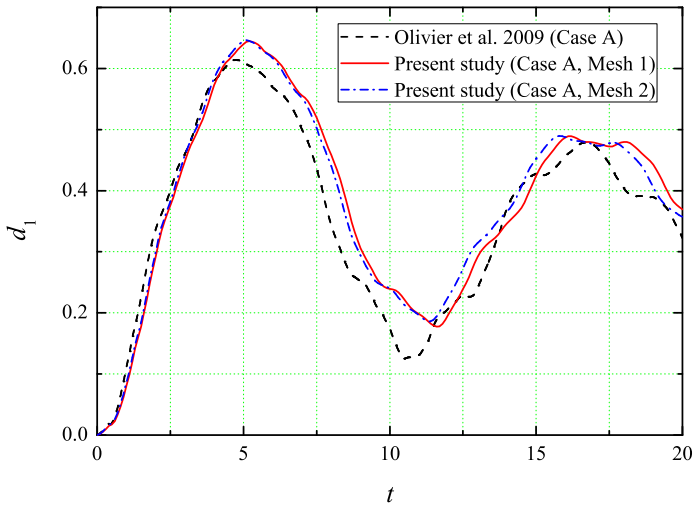

Fig. 7.59 Time history of x_1-displacement

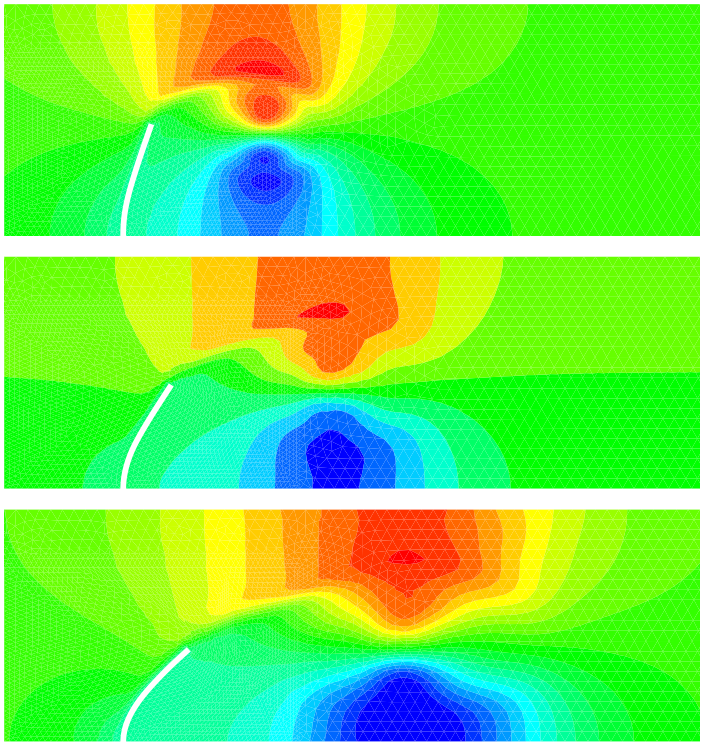

Fig. 7.60 x_1-velocity graphs in Case A

Chapter 8

Conclusions and future work

8.1 Concluding remarks

The CIBC method effectively combines the Dirichlet boundary condition with the Neumann one, in a Robin-like way [1]. Some improvements and extensions of this hybrid method have been presented in this thesis, as an interesting approach to impose interface coupling conditions for FSI simulations. To this end, the merits of the CIBC method are realized from its various applications: (i) the technique probably achieves the global accuracy and stability equal to individual fields; (ii) the small mass ratio is realized for an oscillating bluff body; (iii) the stability is expanded for explicit coupling scheme through the coupled thermal simulations; and (iv) the good adaptability is acquired by equipping useful techniques.

Two improved CIBC methods are developed here to fix those existing shortcomings. In these CIBC formulae, all details are re-derived as exhaustively as possible, with in-depth insights. Before that, the global FSI system has been already set up for the ALE-FEM and all elements have been interpreted in previous chapters. While equipped with different partitioned solution procedures, the present methods are tested via the published data for a number of benchmark problems. In general, the satisfactory agreement is unveiled between the well-documented and present data. In particular, some important flow-induced phenomena are accurately reproduced.

The main contributions are listed below [1]:

1. The CIBC method is throughly re-computed from $\boldsymbol{\sigma}^{\mathrm{f}} = p\mathbf{I}$ or the complete fluid stress, both of which lead to the simpler formulae.

2. In consideration of $\boldsymbol{\sigma}^{\mathrm{f}} = p\mathbf{I}$, Formulation I is proposed to completely remove the structural traction that disables the fluid–rigid structure interplay. The first-order ODEs are solved in tandem with initial conditions after algebraic manipulations. Despite the achievement, the developed method leads to inconvenience of computation in certain situations.
3. Formulation II is proposed based upon the fluid stress to generalize the CIBC method. Its derivation is natrually applicable to various FSI problems where no ODEs appear. The resulting CIBC formulae are of considerable simple form.
4. The two formulations restore the traction consistency and the fluid–rigid body computation. A few details are discussed deeply, such as the sequence of CIBC corrections, the weak execution, the instability source and its reparation, the generalized inverse matrix for correcting rotation, and the free parameter.
5. The method is applied to various partitioned coupling methods in association with other techniques that may improve accuracy and efficiency further.

8.2 Future work

Coupling via the interface among all interacting individual fields (i.e. fluid, solid/structure and moving mesh) is the essential element of FSI. Though this thesis has mainly reported the argumentation of the CIBC method, the future work may be recommended below:

1. To justify the advantages of the CIBC method analytically, a new 1D model that precisely represents convection and diffusion in an incompressible fluid is expected to be proposed. Based upon the above accomplishment, the stabilizing effect and energy conservation are accurately analyzed for multidimensional situations.
2. To manifest its performance, the method needs to be further examined for predicting more challenging situations such as turbulence, non-Newtonian fluids, extremely large structural deformation, in both 2D and 3D.
3. The extension to higher-order finite elements and other spatial presentation (e.g. Finite Volume Method or Finite Difference Method) seem necessary for a variety of problems.

References

[1] He T, Zhang K. An overview of the combined interface boundary condition method for fluid–structure interaction. *Archives of Computational Methods in Engineering* 2017; **24**(4):891–934.

[2] Landajuela M, Vidrascu M, Chapelle D, Fernández MA. Coupling schemes for the FSI forward prediction challenge: comparative study and validation. *International Journal for Numerical Methods in Biomedical Engineering* 2017; **33**(4):e02 813.

[3] Wall WA, Ramm E. Fluid–structure interaction based upon a stabilized (ALE) finite element method. In *Proceedings of the 4th World Congress on Computational Mechanics: New Trends and Applications*, Idelsohn SR, Oñate E, Dvorkin EN (eds.), CIMNE, Barcelona, Spain, 1998; 1–20.

[4] Farhat C, Geuzaine P, Brown G. Application of a three-field nonlinear fluid–structure formulation to the prediction of the aeroelastic parameters of an F-16 fighter. *Computers & Fluids* 2003; **32**(1):3–29.

[5] Felippa CA, Park KC, Farhat C. Partitioned analysis of coupled mechanical systems. *Computer Methods in Applied Mechanics and Engineering* 2001; **190**(24):3247–3270.

[6] Tezduyar TE. Finite elements in fluids: Stabilized formulations and moving boundaries and interfaces. *Computers & Fluids* 2007; **36**(2):191–206.

[7] De Boer A, Van Zuijlen AH, Bijl H. Review of coupling methods for non-matching meshes. *Computer Methods in Applied Mechanics and Engineering* 2007; **196**(8):1515–1525.

[8] Hou G, Wang J, Layton A. Numerical methods for fluid–structure interaction—A review. *Communication in Computational Physics* 2012; **12**(2):337–377.

[9] Takagi S, Sugiyama K, Ii S, Matsumoto Y. A review of full Eulerian methods for fluid structure interaction problems. *Journal of Applied Mechanics–ASME* 2012; **79**(1):010 911.

[10] Surana KS, Blackwell B, Powell M, Reddy JN. Mathematical models for fluid–solid interaction and their numerical solutions. *Journal of Fluids and Structures* 2014; **50**:184–216.

[11] Löhner R, Haug E, Michalski A, Muhammad B, Drego A, Nanjundaiah R, Zarfam R. Recent advances in computational wind engineering and fluid–structure interaction. *Journal of Wind Engineering and Industrial Aerodynamics* 2015; **144**:14–23.

[12] Donea J, Huerta A, Ponthot JP, Rodriguez-Ferran A. Chapter 14: Arbitrary Lagrangian–Eulerian Methods. *Encyclopedia of Computational Mechanics Vol. 1: Fundamentals*, Stein E, de Borst R, Hughes TJR (eds.). John Wiley & Sons: West Sussex, England, 2004; 413–437.

[13] Blom FJ. A monolithical fluid–structure interaction algorithm applied to the piston problem. *Computer Methods in Applied Mechanics and Engineering* 1998; **167**(3):369–391.

[14] Liu J, Jaiman RK, Gurugubelli PS. A stable second-order scheme for fluid–structure interaction with strong added-mass effects. *Journal of Computational Physics* 2014; **270**:687–710.

[15] Hu Z, Tang W, Xue H, Zhang X. A SIMPLE-based monolithic implicit method for strong-coupled fluid–structure interaction problems with free surfaces. *Computer Methods in Applied Mechanics and Engineering* 2016; **299**:90–115.

[16] Farhat C, Lesoinne M. Two efficient staggered algorithms for the serial and parallel solution of three-dimensional nonlinear transient aeroelastic problems. *Computer Methods in Applied Mechanics and Engineering* 2000; **182**(3):499–515.

[17] Le Tallec P, Mouro J. Fluid structure interaction with large structural displacements. *Computer Methods in Applied Mechanics and Engineering* 2001; **190**(24):3039–3067.

[18] Fernández MA, Gerbeau JF, Grandmont C. A projection semi-implicit scheme for the coupling of an elastic structure with an incompressible fluid. *International Journal for Numerical Methods in Engineering* 2007; **69**(4):794–821.

[19] Park KC, Felippa CA, DeRuntz JA. Stabilization of staggered solution procedures for fluid–structure interaction analysis. In *Computational Methods for Fluid–Structure Interaction Problems*, Belytschko T, Geers TL (eds.), New York, USA, 1977; 95–124.

[20] Anju A, Maruoka A, Kawahara M. 2-D fluid–structure interaction problems by an arbitrary Lagrangian–Eulerian finite element method. *International Journal of Computational Fluid Dynamics* 1997; **8**(1):1–9.

[21] Guidoboni G, Glowinski R, Cavallini N, Canic S. Stable loosely-coupled-type algorithm for fluid–structure interaction in blood flow. *Journal of Computational Physics* 2009; **228**(18):6916–6937.

[22] He T. Partitioned coupling strategies for fluid–structure interaction with large displacement: Explicit, implicit and semi-implicit schemes. *Wind & Structures* 2015; **20**(3):423–448.

[23] Dettmer WG, Perić D. A fully implicit computational strategy for strongly coupled fluid–solid interaction. *Archives of Computational Methods in Engineering* 2007; **14**(3):205–247.

[24] Degroote J. Partitioned simulation of fluid–structure interaction. *Archives of Computational Methods in Engineering* 2013; **20**(3):185–238.

[25] Causin P, Gerbeau JF, Nobile F. Added-mass effect in the design of partitioned algorithms for fluid–structure problems. *Computer Methods in Applied Mechanics and Engineering* 2005; **194**(42):4506–4527.

[26] Förster C, Wall WA, Ramm E. Artificial added mass instabilities in sequential staggered coupling of nonlinear structures and incompressible viscous flows. *Computer Methods in Applied Mechanics and Engineering* 2007; **196**(7):1278–1293.

[27] van Brummelen EH. Added mass effects of compressible and incompressible flows in fluid–structure interaction. *Journal of Applied Mechanics–ASME* 2009; **76**(2):021 206.

[28] Badia S, Codina R. On some fluid–structure iterative algorithms using pressure segregation methods. Application to aeroelasticity. *International Journal for Numerical Methods in Engineering* 2007; **72**(1):46–71.

[29] Chorin AJ. Numerical solution of the Navier–Stokes equations. *Mathematics of Computation* 1968; **22**(104):745–762.

[30] Témam R. Une méthode d'approximation de la solution des équations de Navier–Stokes. *Bulletin de la Société Mathématique de France* 1968; **96**:115–152.

[31] Quaini A, Quarteroni A. A semi-implicit approach for fluid–structure interaction based on an algebraic fractional step method. *Mathematical Models and Methods in Applied Sciences* 2007; **17**(6):957–983.

[32] Badia S, Quaini A, Quarteroni A. Splitting methods based on algebraic factorization for fluid–structure interaction. *SIAM Journal on Scientific Computing* 2008; **30**(4):1778–1805.

[33] Astorino M, Chouly F, Fernández MA. Robin based semi-implicit coupling in fluid–structure interaction: stability analysis and numerics. *SIAM Journal on Scientific Computing* 2009; **31**(6):4041–4065.

[34] Astorino M, Grandmont C. Convergence analysis of a projection semi-implicit coupling scheme for fluid–structure interaction problems. *Numerische Mathematik* 2010; **116**(4):721–767.

[35] Fernández MA. Coupling schemes for incompressible fluid–structure interaction: implicit, semi-implicit and explicit. *SeMa Journal* 2011; **55**(1):59–108.

[36] He T, Zhou D, Han Z, Tu J, Ma J. Partitioned subiterative coupling schemes for aeroelasticity using combined interface boundary condition method. *International Journal of Computational Fluid Dynamics* 2014; **28**(6-10):272–300.

[37] He T. Semi-implicit coupling of CS-FEM and FEM for the interaction between a geometrically nonlinear solid and an incompressible fluid. *International Journal of Computational Methods* 2015; **12**(5):1550 025.

[38] Jan YJ, Sheu TWH. Finite element analysis of vortex shedding oscillations from cylinders in the straight channel. *Computational Mechanics* 2004; **33**(2):81–94.

[39] He T, Zhang K. Combined interface boundary condition method for fluid–structure interaction: Some improvements and extensions. *Ocean Engineering* 2015; **109**:243–255.

[40] He T. A CBS-based partitioned semi-implicit coupling algorithm for fluid–structure interaction using MCIBC method. *Computer Methods in Applied Mechanics and Engineering* 2016; **298**:252–278.

[41] Zienkiewicz OC, Codina R. A general algorithm for compressible and incompressible flow. Part I: The split, characteristic-based scheme. *International Journal for Numerical Methods in Fluids* 1995; **20**(8-9):869–885.

[42] Zienkiewicz OC, Morgan K, Sai BVK, Codina R, Vasquez M. A general algorithm for compressible and incompressible flow. Part II: Tests on the explicit form. *International Journal for Numerical Methods in Fluids* 1995; **20**(8-9):887–913.

[43] Codina R, Vázquez M, Zienkiewicz OC. A general algorithm for compressible and incompressible flows. Part III: The semi-implicit form. *International Journal for Numerical Methods in Fluids* 1998; **27**(1-4):13–32.

[44] Sy S, Murea CM. A stable time advancing scheme for solving fluid–structure interaction problem at small structural displacements. *Computer Methods in Applied Mechanics and Engineering* 2008; **198**(2):210–222.

[45] Murea CM, Sy S. A fast method for solving fluid–structure interaction problems numerically. *International Journal for Numerical Methods in Fluids* 2009; **60**(10):1149–1172.

[46] Breuer M, De Nayer G, Münsch M, Gallinger T, Wüchner R. Fluid–structure interaction using a partitioned semi-implicit predictor-corrector coupling scheme for the application of large-eddy simulation. *Journal of Fluids and Structures* 2012; **29**:107–130.

[47] He T, Zhang K, Wang T. AC-CBS-based partitioned semi-implicit coupling algorithm for fluid–structure interaction using stabilized second-order pressure scheme. *Communications in Computational Physics* 2017; **21**(5):1449–1474.

[48] He T, Wang T, Zhang H. The use of artificial compressibility to improve partitioned semi-implicit FSI coupling within the classical Chorin–Témam projection framework. *Computers & Fluids* 2018; **166**:64–77.

[49] Chorin AJ. A numerical method for solving incompressible viscous flow problems. *Journal of Computational Physics* 1967; **2**(1):12–26.

[50] Lefrançois E. How an added mass matrix estimation may dramatically improve FSI calculations for moving foils. *Applied Mathematical Modelling* 2017; **51**:655–668.

[51] Jaiman R, Geubelle P, Loth E, Jiao X. Stable and accurate loosely-coupled scheme for unsteady fluid–structure interaction. In *Proceedings of the 45th AIAA Aerospace Sciences Meeting and Exhibit*, American Institute of Aeronautics and Astronautics: Reno, Nevada, USA, 2007; 1–28.

[52] Jaiman R, Geubelle P, Loth E, Jiao X. Combined interface boundary condition method for unsteady fluid–structure interaction. *Computer Methods in Applied Mechanics and Engineering* 2011; **200**(1):27–39.

[53] Jaiman R, Geubelle P, Loth E, Jiao X. Transient fluid–structure interaction with non-matching spatial and temporal discretizations. *Computers & Fluids* 2011; **50**(1):120–135.

[54] Jaiman RK, Jiao X, Geubelle PH, Loth E. Conservative load transfer along curved fluid–solid interface with non-matching meshes. *Journal of Computational Physics* 2006; **218**(1):372–397.

[55] Feng X. Analysis of finite element methods and domain decomposition algorithms for a fluid–solid interaction problem. *SIAM Journal on Numerical Analysis* 2000; **38**(4):1312–1336.

[56] Farhat C, Lesoinne M, Maman N. Mixed explicit/implicit time integration of coupled aeroelastic problems: Three-field formulation, geometric conservation and distributed solution. *International Journal for Numerical Methods in Fluids* 1995; **21**(10):807–835.

[57] Piperno S. Explicit/implicit fluid/structure staggered procedures with a structural predictor and fluid subcycling for 2D inviscid aeroelastic simulations. *International Journal for Numerical Methods in Fluids* 1997; **25**(10):1207–1226.

[58] Roe B, Jaiman R, Haselbacher A, Geubelle PH. Combined interface boundary condition method for coupled thermal simulations. *International Journal for Numerical Methods in Fluids* 2008; **57**(3):329–354.

[59] Rice JR, Tsompanopoulou P, Vavalis E. Interface relaxation methods for elliptic differential equations. *Applied Numerical Mathematics* 2000; **32**(2):219–245.

[60] Tsompanopoulou P, Vavalis E. An experimental study of interface relaxation methods for composite elliptic differential equations. *Applied Mathematical Modelling* 2008; **32**(8):1620–1641.

[61] Jaiman RK, Shakib F, Oakley OH, Constantinides Y. Fully coupled fluid–structure interaction for offshore applications. In *Proceedings of the 28th International Conference on Ocean, Offshore and Arctic Engineering*, American Society of Mechanical Engineers: Honolulu, Hawaii, USA, 2009; 757–765.

[62] Badia S, Nobile F, Vergara C. Fluid–structure partitioned procedures based on Robin transmission conditions. *Journal of Computational Physics* 2008; **227**(14):7027–7051.

[63] Jaiman RK. Advances in ALE based fluid–structure interaction modeling for offshore engineering applications. In *Proceedings of the 6th European Congress on Computational Methods in Applied Sciences and Engineering (ECCOMAS 2012)*, Eberhardsteiner J, Böhm H, Rammerstorfer F (eds.), Vienna, Austria, 2012; 1–11.

[64] Jaiman RK, Pillalamarri NR, Guan MZ. A stable second-order partitioned iterative scheme for freely vibrating low-mass bluff bodies in a uniform flow. *Computer Methods in Applied Mechanics and Engineering* 2016; **301**:187–215.

[65] Mok DP, Wall WA. Partitioned analysis schemes for the transient interaction of incompressible flows and nonlinear flexible structures. In *Trends in Computational Structural Mechanics*, Wall WA, Bletzinger KU, Schweizerhof K (eds.), CIMNE: Barcelona, Spain, 2001; 689–698.

[66] Küttler U, Wall WA. Fixed-point fluid–structure interaction solvers with dynamic relaxation. *Computational Mechanics* 2008; **43**(1):61–72.

[67] Küttler U, Wall WA. Vector extrapolation for strong coupling fluid–structure interaction solvers. *Journal of Applied Mechanics–ASME* 2009; **76**(2):021 205.

[68] He T, Zhou D, Bao Y. Combined interface boundary condition method for fluid–rigid body interaction. *Computer Methods in Applied Mechanics and Engineering* 2012; **223**:81–102.

[69] He T. A partitioned implicit coupling strategy for incompressible flow past an oscillating cylinder. *International Journal of Computational Methods* 2015; **12**(2):1550 012.

[70] Rossi R, Oñate E. Analysis of some partitioned algorithms for fluid–structure interaction. *Engineering Computations* 2010; **27**(1):20–56.

[71] Dettmer WG, Perić D. A new staggered scheme for fluid–structure interaction. *International Journal for Numerical Methods in Engineering* 2013; **93**(1):1–22.

[72] Jaiman RK, Guan MZ, Miyanawala TP. Partitioned iterative and dynamic subgrid-scale methods for freely vibrating square-section structures at subcritical Reynolds number. *Computers & Fluids* 2016; **133**:68–89.

[73] Cervera M, Codina R, Galindo M. On the computational efficiency and implementation of block-iterative algorithms for nonlinear coupled problems. *Engineering Computations* 1996; **13**(6):4–30.

[74] Afrasiab H, Movahhedy MR, Assempour A. Fluid–structure interaction analysis in microfluidic devices: A dimensionless finite element approach. *International Journal for Numerical Methods in Fluids* 2012; **68**(9):1073–1086.

[75] Zienkiewicz OC, Nithiarasu P, Codina R, Vazquez M, Ortiz P. The characteristic-based-split procedure: An efficient and accurate algorithm for fluid problems. *International Journal for Numerical Methods in Fluids* 1999; **31**(1):359–392.

[76] Löhner R, Morgan K, Zienkiewicz OC. The solution of non-linear hyperbolic equation systems by the finite element method. *International Journal for Numerical Methods in Fluids* 1984; **4**(11):1043–1063.

[77] He T, Zhang H, Zhang K. A smoothed finite element approach for computational fluid dynamics: applications to incompressible flows and fluid–structure interaction. *Computational Mechanics* 2018; **1–21**: doi: 10.1007/s00 466–018–1549–x.

[78] Nithiarasu P. An arbitrary Lagrangian Eulerian (ALE) formulation for free surface flows using the characteristic-based split (CBS) scheme. *International Journal for Numerical Methods in Fluids* 2005; **48**(12):1415–1428.

[79] Nobari MRH, Naderan H. A numerical study of flow past a cylinder with cross flow and inline oscillation. *Computers & Fluids* 2006; **35**(4):393–415.

[80] Klettner CA, Eames I. Viscous free surface simulations with the characteristic based split scheme. *Computers & Fluids* 2013; **71**:487–495.

[81] Kang W, Zhang J, Lei P, Xu M. Computation of unsteady viscous flow around a locally flexible airfoil at low Reynolds number. *Journal of Fluids and Structures* 2014; **46**:42–58.

[82] He T. A partitioned implicit coupling strategy for incompressible flow past an oscillating cylinder. *International Journal of Computational Methods* 2015; **12**(2):1550 012.

[83] He T. On a partitioned strong coupling algorithm for modeling fluid–structure interaction. *International Journal of Applied Mechanics* 2015; **7**(2):1550 021.

[84] Han Z, Zhou D, He T, Tu J, Li C, Kwok KC, Fang C. Flow-induced vibrations of four circular cylinders with square arrangement at low Reynolds numbers. *Ocean Engineering* 2015; **96**:21–33.

[85] Nithiarasu P, Zienkiewicz OC. On stabilization of the CBS algorithm: Internal and external time steps. *International Journal for Numerical Methods in Engineering* 2000; **48**(6):875–880.

[86] Han Z, Zhou D, Tu J, Fang C, He T. Flow over two side-by-side square cylinders by CBS finite element scheme of Spalart–Allmaras model. *Ocean Engineering* 2014; **87**:40–49.

[87] Duan Q, Li X. An ALE based iterative CBS algorithm for non-isothermal non-Newtonian flow with adaptive coupled finite element and meshfree method. *Computer Methods in Applied Mechanics and Engineering* 2007; **196**(49):4911–4933.

[88] Zhang XH, Ouyang J, Zhang L. The characteristic-based split (CBS) meshfree method for free surface flow problems in ALE formulation. *International Journal for Numerical Methods in Fluids* 2011; **65**(7):798–811.

[89] Zhang ZQ, Liu GR, Khoo BC. Immersed smoothed finite element method for two dimensional fluid–structure interaction problems. *International Journal for Numerical Methods in Engineering* 2012; **90**(10):1292–1320.

[90] Nithiarasu P. On boundary conditions of the characteristic based split (CBS) algorithm for fluid dynamics. *International Journal for Numerical Methods in Engineering* 2002; **54**(4):523–536.

[91] Codina R, Zienkiewicz OC. CBS versus GLS stabilization of the incompressible Navier–Stokes equations and the role of the time step as stabilization parameter. *Communications in Numerical Methods in Engineering* 2002; **18**(2):99–112.

[92] Nithiarasu P. A matrix free fractional step method for static and dynamic incompressible solid mechanics. *International Journal for Computational Methods in Engineering Science and Mechanics* 2006; **7**(5):369–380.

[93] Zienkiewicz OC, Taylor RL, Nithiarasu P. *The Finite Element Method for Fluid Dynamics*. 6th edn., Butterworth–Heinemann: Oxford, UK, 2005.

[94] Nithiarasu P, Codina R, Zienkiewicz OC. The Characteristic-Based Split (CBS) scheme—a unified approach to fluid dynamics. *International Journal for Numerical Methods in Engineering* 2006; **66**(10):1514–1546.

[95] Bevan RLT, Boileau E, van Loon R, Lewis RW, Nithiarasu P. A comparative study of fractional step method in its quasi-implicit, semi-implicit and fully-explicit forms for incompressible flows. *International Journal of Numerical Methods for Heat & Fluid Flow* 2016; **26**(3/4):595–623.

[96] Nithiarasu P. A fully explicit characteristic based split (CBS) scheme for viscoelastic flow calculations. *International Journal for Numerical Methods in Engineering* 2004; **60**(5):949–978.

[97] Zienkiewicz OC, Taylor RL, Zhu JZ. *The Finite Element Method: Its Basis and Fundamentals*. 6th edn., Butterworth–Heinemann: Oxford, UK, 2005.

[98] Roshko A. On the development of turbulent wakes from vortex streets. *Technical Report NACA TN 1191*, National Advisory Committee for Aeronautics 1954.

[99] Williamson CHK. Oblique and parallel modes of vortex shedding in the wake of a circular cylinder at low Reynolds numbers. *Journal of Fluid Mechanics* 1989; **206**:579–627.

[100] Norberg C. An experimental investigation of the flow around a circular cylinder: influence of aspect ratio. *Journal of Fluid Mechanics* 1994; **258**:287–316.

[101] Fey U, König M, Eckelmann H. A new Strouhal–Reynolds-number relationship for the circular cylinder in the range $47 < Re < 2 \times 10^5$. *Physics of Fluids* 1998; **10**(7):1547–1549.

[102] Williamson CHK, Brown GL. A series in $1/\sqrt{Re}$ to represent the Strouhal–Reynolds number relationship of the cylinder wake. *Journal of Fluids and Structures* 1998; **12**(8):1073–1085.

[103] Norberg C. Fluctuating lift on a circular cylinder: review and new measurements. *Journal of Fluids and Structures* 2003; **17**(1):57–96.

[104] Thom A. The flow past circular cylinders at low speeds. *Proceedings of the Royal Society of London. Series A, Containing Papers of a Mathematical and Physical Character* 1933; **141**(845):651–669.

[105] Wieselsberger C. New data on the laws of fluid resistance. *Physikalische Zeitschrift* 1921; **22**:321–328.

[106] Graham JMR. Comparing computation of flow past circular cylinders with experimental data. In *Bluff-Body Wakes, Dynamics and Instabilities: IUTAM Symposium*, Eckelmann H, Graham JMR, Huerre P, Monkewitz PA (eds.), Springer-Verlag Belin Heidelberg: Göttingen, Germany, 1993; 317–324.

[107] Bearman PW. Developments in the understanding of bluff body flows. *JSME International Journal Series B Fluids and Thermal Engineering* 1998; **41**(1):103–114.

[108] Anagnostopoulos P. Numerical investigation of response and wake characteristics of a vortex-excited cylinder in a uniform stream. *Journal of Fluids and Structures* 1994; **8**(4):367–390.

[109] Zhou CY, So RMC, Lam K. Vortex-induced vibrations of an elastic circular cylinder. *Journal of Fluids and Structures* 1999; **13**(2):165–189.

[110] Bahmani MH, Akbari MH. Effects of mass and damping ratios on VIV of a circular cylinder. *Ocean Engineering* 2010; **37**(5):511–519.

[111] Okajima A. Strouhal numbers of rectangular cylinders. *Journal of Fluid Mechanics* 1982; **123**:379–398.

[112] Sohankar A, Norbergb C, Davidson L. Numerical simulation of unsteady low-Reynolds number flow around rectangular cylinders at incidence. *Journal of Wind Engineering and Industrial Aerodynamics* 1997; **69**:189–201.

[113] Breuer M, Bernsdorf J, Zeiser T, Durst F. Accurate computations of the laminar flow past a square cylinder based on two different methods: lattice-Boltzmann and finite-volume. *International Journal of Heat and Fluid Flow* 2000; **21**(2):186–196.

[114] Galletti B, Bruneau CH, Zannetti L, Iollo A. Low-order modelling of laminar flow regimes past a confined square cylinder. *Journal of Fluid Mechanics* 2004; **503**:161–170.

[115] Sharma A, Eswaran V. Heat and fluid flow across a square cylinder in the two-dimensional laminar flow regime. *Numerical Heat Transfer, Part A: Applications* 2004; **45**(3):247–269.

[116] Sen S, Mittal S, Biswas G. Flow past a square cylinder at low Reynolds numbers. *International Journal for Numerical Methods in Fluids* 2011; **67**(9):1160–1174.

[117] Williamson CHK, Roshko A. Vortex formation in the wake of an oscillating cylinder. *Journal of Fluids and Structures* 1988; **2**(4):355–381.

[118] Nomura T, Hughes TJR. An arbitrary Lagrangian–Eulerian finite element method for interaction of fluid and a rigid body. *Computer Methods in Applied Mechanics and Engineering* 1992; **95**(1):115–138.

[119] Sarrate J, Huerta A, Donea J. Arbitrary Lagrangian–Eulerian formulation for fluid–rigid body interaction. *Computer Methods in Applied Mechanics and Engineering* 2001; **190**(24):3171–3188.

[120] Cori JF, Etienne S, Garon A, Pelletier D. High-order implicit Runge–Kutta time integrators for fluid–structure interactions. *International Journal for Numerical Methods in Fluids* 2015; **78**(7):385–412.

[121] Bathe KJ, Ramm E, Wilson EL. Finite element formulations for large deformation dynamic analysis. *International Journal for Numerical Methods in Engineering* 1975; **9**(2):353–386.

[122] Dai KY, Liu GR. Free and forced vibration analysis using the smoothed finite element method (SFEM). *Journal of Sound and Vibration* 2007; **301**(3):803–820.

[123] Cui XY, Liu GR, Li GY, Zhao X, Nguyen TT, Sun GY. A smoothed finite element method (SFEM) for linear and geometrically nonlinear analysis of plates and shells. *CMES: Computer Modeling in Engineering & Sciences* 2008; **28**(2):109–126.

[124] Braun AL, Awruch AM. A partitioned model for fluid–structure interaction problems using hexahedral finite elements with one-point quadrature. *International Journal for Numerical Methods in Engineering* 2009; **79**(5):505–549.

[125] Chen JS, Wu CT, Yoon S, You Y. A stabilized conforming nodal integration for Galerkin mesh-free methods. *International Journal for Numerical Methods in Engineering* 2001; **50**(2):435–466.

[126] Yoo JW, Moran B, Chen JS. Stabilized conforming nodal integration in the natural-element method. *International Journal for Numerical Methods in Engineering* 2004; **60**(5):861–890.

[127] Liu GR, Dai KY, Nguyen TT. A smoothed finite element method for mechanics problems. *Computational Mechanics* 2007; **39**(6):859–877.

[128] Liu GR, Nguyen TT. *Smoothed Finite Element Methods*. CRC Press, 2010.

[129] Zeng W, Liu GR. Smoothed finite element methods (S-FEM): An overview and recent developments. *Archives of Computational Methods in Engineering* 2018; **25**(2):397–435.

[130] Newmark NM. A method of computation for structural dynamics. *Journal of Engineering Mechanics–ASCE* 1959; **85**(3):67–94.

[131] Hilber HM, Hughes TJ, Taylor RL. Improved numerical dissipation for time integration algorithms in structural dynamics. *Earthquake Engineering & Structural Dynamics* 1977; **5**(3):283–292.

[132] Chung J, Hulbert GM. A time integration algorithm for structural dynamics with improved numerical dissipation: The Generalized-α method. *Journal of Applied Mechanics–ASME* 1993; **60**(2):371–375.

[133] Bathe KJ, Baig MMI. On a composite implicit time integration procedure for nonlinear dynamics. *Computers & Structures* 2005; **83**(31):2513–2524.

[134] Bathe KJ. Conserving energy and momentum in nonlinear dynamics: A simple implicit time integration scheme. *Computers & Structures* 2007; **85**(7):437–445.

[135] Bathe KJ, Noh G. Insight into an implicit time integration scheme for structural dynamics. *Computers & Structures* 2012; **98**:1–6.

[136] Dettmer W, Perić D. A computational framework for fluid–rigid body interaction: Finite element formulation and applications. *Computer Methods in Applied Mechanics and Engineering* 2006; **195**(13):1633–1666.

[137] Dettmer W, Perić D. A computational framework for fluid–structure interaction: Finite element formulation and applications. *Computer Methods in Applied Mechanics and Engineering* 2006; **195**(41):5754–5779.

[138] Kuhl D, Crisfield MA. Energy-conserving and decaying algorithms in non-linear structural dynamics. *International Journal for Numerical Methods in Engineering* 1999; **45**(5):569–599.

[139] Zhang J, Liu Y, Liu D. Accuracy of a composite implicit time integration scheme for structural dynamics. *International Journal for Numerical Methods in Engineering* 2017; **109**(3):368–406.

[140] Collatz L. *The Numerical Treatment of Differential Equations*. Springer–Verlag: New York, 1960.

[141] Piperno S, Farhat C, Larrouturou B. Partitioned procedures for the transient solution of coupled aroelastic problems - Part I: Model problem, theory and two-dimensional application. *Computer Methods in Applied Mechanics and Engineering* 1995; **124**(1):79–112.

[142] Suk JW, Kim JH, Kim YH. A predictor algorithm for fast geometrically-nonlinear dynamic analysis. *Computer Methods in Applied Mechanics and Engineering* 2003; **192**(22):2521–2538.

[143] Yang FL, Chen CH, Young DL. A novel mesh regeneration algorithm for 2D FEM simulations of flows with moving boundary. *Journal of Computational Physics* 2011; **230**(9):3276–3301.

[144] Kanchi H, Masud A. A 3D adaptive mesh moving scheme. *International Journal for Numerical Methods in Fluids* 2007; **54**(6-8):923–944.

[145] Batina JT. Unsteady Euler airfoil solutions using unstructured dynamic meshes. *AIAA Journal* 1990; **28**(8):1381–1388.

[146] Zeng D, Ethier CR. A semi-torsional spring analogy model for updating unstructured meshes in 3D moving domains. *Finite Elements in Analysis and Design* 2005; **41**(11):1118–1139.

[147] Lefrançois E. A simple mesh deformation technique for fluid–structure interaction based on a submesh approach. *International Journal for Numerical Methods in Engineering* 2008; **75**(9):1085–1101.

[148] Markou GA, Mouroutis ZS, Charmpis DC, Papadrakakis M. The ortho-semi-torsional (OST) spring analogy method for 3D mesh moving boundary problems. *Computer Methods in Applied Mechanics and Engineering* 2007; **196**(4):747–765.

[149] Farhat C, Degand C, Koobus B, Lesoinne M. Torsional springs for two-dimensional dynamic unstructured fluid meshes. *Computer Methods in Applied Mechanics and Engineering* 1998; **163**(1-4):231–245.

[150] Blom FJ. Considerations on the spring analogy. *International Journal for Numerical Methods in Fluids* 2000; **32**(6):647–668.

[151] Souli M, Ouahsine A, Lewin L. ALE formulation for fluid–structure interaction problems. *Computer Methods in Applied Mechanics and Engineering* 2000; **190**(5):659–675.

[152] Liu X, Qin N, Xia H. Fast dynamic grid deformation based on Delaunay graph mapping. *Journal of Computational Physics* 2006; **211**(2):405–423.

[153] Lesoinne M, Farhat C. Geometric conservation laws for flow problems with moving boundaries and deformable meshes, and their impact on aeroelastic computations. *Computer Methods in Applied Mechanics and Engineering* 1996; **134**(1):71–90.

[154] Étienne S, Garon A, Pelletier D. Perspective on the geometric conservation law and finite element methods for ALE simulations of incompressible flow. *Journal of Computational Physics* 2009; **228**(7):2313–2333.

[155] Fanion T, Fernández M, Le Tallec P. Deriving adequate formulations for fluid–structure interaction problems: from ALE to transpiration. *Revue Européenne des Éléments* 2000; **9**(6-7):681–708.

[156] Deparis S, Fernández MA, Formaggia L. Acceleration of a fixed point algorithm for fluid–structure interaction using transpiration conditions. *ESAIM: Mathematical Modelling and Numerical Analysis* 2003; **37**(4):601–616.

[157] Bekka N, Sellam M, Chpoun A. Aeroelastic stability analysis of a flexible over-expanded rocket nozzle using numerical coupling by the method of transpiration. *Journal of Fluids and Structures* 2015; **56**:89–106.

[158] Bridges TJ. Multi-symplectic structures and wave propagation. *Mathematical Proceedings of the Cambridge Philosophical Society* 1997; **121**(1):147–190.

[159] Payen DJ, Bathe KJ. A stress improvement procedure. *Computers & Structures* 2012; **112-113**:311–326.

[160] He T, Yang J, Baniotopoulos C. Improving the cbs-based partitioned semi-implicit coupling algorithm for fluid–structure interaction. *International Journal for Numerical Methods in Fluids* 2018; **87**:463–486.

[161] Matthies HG, Steindorf J. Partitioned strong coupling algorithms for fluid–structure interaction. *Computers & Structures* 2003; **81**(8):805–812.

[162] Irons BM, Tuck RC. A version of the Aitken accelerator for computer iteration. *International Journal for Numerical Methods in Engineering* 1969; **1**(3):275–277.

[163] Baek H, Karniadakis GE. A convergence study of a new partitioned fluid–structure interaction algorithm based on fictitious mass and damping. *Journal of Computational Physics* 2012; **231**(2):629–652.

[164] Prasanth TK, Mittal S. Vortex-induced vibrations of a circular cylinder at low Reynolds numbers. *Journal of Fluid Mechanics* 2008; **594**:463–491.

[165] Anagnostopoulos P, Bearman PW. Response characteristics of a vortex-excited cylinder at low Reynolds numbers. *Journal of Fluids and Structures* 1992; **6**(1):39–50.

[166] Wei R, Sekine A, Shimura M. Numerical analysis of 2D vortex-induced oscillations of a circular cylinder. *International Journal for Numerical Methods in Fluids* 1995; **21**(10):993–1005.

[167] Schulz KW, Kallinderis Y. Unsteady flow structure interaction for incompressible flows using deformable hybrid grids. *Journal of Computational Physics* 1998; **143**(2):569–597.

[168] Li L, Sherwin S, Bearman PW. A moving frame of reference algorithm for fluid/structure interaction of rotating and translating bodies. *International Journal for Numerical Methods in Fluids* 2002; **38**(2):187–206.

[169] Abdullah MM, Walsh KK, Grady S, Wesson GD. Modeling flow around bluff bodies. *Journal of Computing in Civil Engineering–ASCE* 2005; **19**(1):104–107.

[170] Yang J, Preidikman S, Balaras E. A strongly coupled, embedded-boundary method for fluid–structure interactions of elastically mounted rigid bodies. *Journal of Fluids and Structures* 2008; **24**(2):167–182.

[171] Nomura T. Finite element analysis of vortex-induced vibrations of bluff cylinders. *Journal of Wind Engineering and Industrial Aerodynamics* 1993; **46**:587–594.

[172] De Rosis A, Falcucci G, Ubertini S, Ubertini F, Succi S. Lattice Boltzmann analysis of fluid–structure interaction with moving boundaries. *Communications in Computational Physics* 2013; **13**(3):823–834.

[173] Samaniego C, Houzeaux G, Samaniego E, Vázquez M. Parallel embedded boundary methods for fluid and rigid–body interaction. *Computer Methods in Applied Mechanics and Engineering* 2015; **290**:387–419.

[174] Young DL, Chang JT, Eldho TI. A coupled BEM and arbitrary Lagrangian–Eulerian FEM model for the solution of two-dimensional laminar flows in external flow fields. *International Journal for Numerical Methods in Engineering* 2001; **51**(9):1053–1077.

[175] DeJong A, Liang C. Parallel spectral difference method for predicting 3D vortex-induced vibrations. *Computers & Fluids* 2014; **98**:17–26.

[176] Govardhan R, Williamson CHK. Modes of vortex formation and frequency response of a freely vibrating cylinder. *Journal of Fluid Mechanics* 2000; **420**:85–130.

[177] Robertson I, Li L, Sherwin SJ, Bearman PW. A numerical study of rotational and transverse galloping rectangular bodies. *Journal of Fluids and Structures* 2003; **17**(5):681–699.

[178] Blevins RD. *Flow-Induced Vibration*. 2nd edn., Van Nostrand Reinhold Co., Inc.: New York,USA, 1990.

[179] Barrero-Gil A, Sanz-Andres A, Roura M. Transverse galloping at low Reynolds numbers. *Journal of Fluids and Structures* 2009; **25**(7):1236–1242.

[180] Joly A, Etienne S, Pelletier D. Galloping of square cylinders in cross-flow at low Reynolds numbers. *Journal of Fluids and Structures* 2012; **28**:232–243.

[181] Sen S, Mittal S. Free vibration of a square cylinder at low Reynolds numbers. *Journal of Fluids and Structures* 2011; **27**(5):875–884.

[182] Parkinson GV, Smith JD. The square prism as an aeroelastic non-linear oscillator. *The Quarterly Journal of Mechanics and Applied Mathematics* 1964; **17**(2):225–239.

[183] Hübner B, Walhorn E, Dinkier D. Strongly coupled analysis of fluid–structure interaction using space-time finite elements. In *Proceedings of the 2nd European Conference on Computational Mechanics*, Cracow, Poland, 2001; 546–547.

[184] Filippini G, Dalcin L, Nigro N, M S. Fluid–rigid body interaction by PETs-FEM driven by Python. *Mecánica Computacional* 2008; **XXVII**(8):489–504.

[185] Fourestey G, Piperno S. A second-order time-accurate ALE Lagrange–Galerkin method applied to wind engineering and control of bridge profiles. *Computer Methods in Applied Mechanics and Engineering* 2004; **193**(39):4117–4137.

[186] Cebral JR, Löhner R. On the loose coupling of implicit time-marching codes. In *Proceedings of the 43th AIAA Aerospace Sciences Meeting and Exhibit*, American Institute of Aeronautics and Astronautics: Reno, Nevada, USA, 2005; 1–15.

[187] Billah KY, Scanlan RH. Resonance, Tacoma Narrows bridge failure, and undergraduate physics textbooks. *American Journal of Physics* 1991; **59**(2):118–124.

[188] Lee N, Lee H, Baek C, Lee S. Aeroelastic analysis of bridge deck flutter with modified implicit coupling method. *Journal of Wind Engineering and Industrial Aerodynamics* 2016; **155**:11–22.

[189] Teixeira PRF, Awruch AM. Numerical simulation of fluid–structure interaction using the finite element method. *Computers & Fluids* 2005; **34**(2):249–273.

[190] Liew KM, Wang WQ, Zhang LX, He XQ. A computational approach for predicting the hydroelasticity of flexible structures based on the pressure Poisson equation. *International Journal for Numerical Methods in Engineering* 2007; **72**(13):1560–1583.

[191] Yamada T, Yoshimura S. Line search partitioned approach for fluid–structure interaction analysis of flapping wing. *CMES: Computer Modeling in Engineering & Sciences* 2008; **24**(1):51–60.

[192] Bazilevs Y, Calo VM, Hughes TJR, Zhang Y. Isogeometric fluid–structure interaction: theory, algorithms, and computations. *Computational Mechanics* 2008; **43**(1):3–37.

[193] Olivier M, Dumas G, Morissette J. A fluid–structure interaction solver for nano-air-vehicle flapping wings. In *Proceedings of the 19th AIAA Computational Fluid Dynamics Conference*, American Institute of Aeronautics and Astronautics: San Antonio, Texas, USA, 2009; 1–15.

[194] Wood C, Gil AJ, Hassan O, Bonet J. Partitioned block-Gauss–Seidel coupling for dynamic fluid–structure interaction. *Computers & Structures* 2010; **88**(23):1367–1382.

[195] Habchi C, Russeil S, Bougeard D, Harion JL, Lemenand T, Ghanem A, Valle DD, Peerhossaini H. Partitioned solver for strongly coupled fluid–structure interaction. *Computers & Fluids* 2013; **71**:306–319.

[196] Baiges J, Codina R. The fixed-mesh ALE approach applied to solid mechanics and fluid–structure interaction problems. *International Journal for Numerical Methods in Engineering* 2010; **81**(12):1529–1557.

Appendix A

Nondimensionalization of the CIBC formulation

We nondimensionalize the CIBC formulae in this appendix [1, 40].

Rigid–body case

It is apparent to know from Eqs. (3.1) and (3.6) that

$$\begin{aligned}
\begin{bmatrix} \frac{D}{m_1U^2} & \\ & \frac{D}{m_2U^2} \end{bmatrix} \begin{Bmatrix} R_1 \\ R_2 \end{Bmatrix} &= \begin{bmatrix} \frac{D}{m_1U^2} & \\ & \frac{D}{m_2U^2} \end{bmatrix} \begin{Bmatrix} F_\mathrm{d} \\ F_\mathrm{l} \end{Bmatrix} + \begin{bmatrix} \frac{D}{m_1U^2} & \\ & \frac{D}{m_2U^2} \end{bmatrix} \begin{Bmatrix} \delta t_1 \\ \delta t_2 \end{Bmatrix} \\
&= \begin{bmatrix} \frac{D}{m_1U^2} & \\ & \frac{D}{m_2U^2} \end{bmatrix} \frac{1}{2}\rho^\mathrm{f}U^2D \begin{Bmatrix} C_\mathrm{d} \\ C_\mathrm{l} \end{Bmatrix} + \begin{bmatrix} \frac{D}{m_1U^2} & \\ & \frac{D}{m_2U^2} \end{bmatrix} \rho^\mathrm{f}U^2D \begin{Bmatrix} \delta\hat{t}_1 \\ \delta\hat{t}_2 \end{Bmatrix} \\
&= \begin{bmatrix} \frac{1}{2\hat{m}_1} & \\ & \frac{1}{2\hat{m}_2} \end{bmatrix} \begin{Bmatrix} C_\mathrm{d} \\ C_\mathrm{l} \end{Bmatrix} + \begin{bmatrix} \frac{1}{\hat{m}_1} & \\ & \frac{1}{\hat{m}_2} \end{bmatrix} \begin{Bmatrix} \delta\hat{t}_1 \\ \delta\hat{t}_2 \end{Bmatrix}, \qquad \text{(A.1a)}
\end{aligned}$$

$$\begin{aligned}
\frac{D^2}{m_\theta U^2}R_\theta &= \frac{D^2}{m_\theta U^2}F_\mathrm{m} + \frac{D^2}{m_\theta U^2}\delta t_\theta \\
&= \frac{D^2}{m_\theta U^2}\cdot\frac{1}{2}\rho^\mathrm{f}U^2D^2\cdot C_\mathrm{m} + \frac{D^2}{m_\theta U^2}\cdot\frac{1}{2}\rho^\mathrm{f}U^2L^2\cdot\delta\hat{t}_\theta \\
&= \frac{1}{2\hat{m}_\theta}C_\mathrm{m} + \frac{1}{\hat{m}_\theta}\delta\hat{t}_\theta, \qquad \text{(A.1b)}
\end{aligned}$$

where $\mathbf{R} = \{\delta R_1,\ \delta R_2,\ \delta R_\theta\}^{\mathrm{T}}$ means the external force and $\{\delta t_1,\ \delta t_2,\ \delta t_\theta\}^{\mathrm{T}}$ denotes the traction increment.

Substitution of the nondimensional scales and $\hat{\Gamma} = \frac{\Gamma}{D}$ into Eq. (5.49b) yields

$$\begin{aligned}\begin{Bmatrix}\delta t_1\\ \delta t_2\end{Bmatrix} &= \int_\Sigma \delta\mathbf{t}\mathrm{d}\Gamma = \rho^{\mathrm{f}} U D\cdot\frac{\Delta\hat{t}}{\omega}\int_\Sigma\left(\left(\hat{\nabla}\cdot\hat{\boldsymbol{\sigma}}^{\mathrm{f}}\right)-\hat{\ddot{\mathbf{d}}}\right)\mathrm{d}\hat{\Gamma}\\ &= \rho^{\mathrm{f}} U^2 D\cdot\frac{\Delta\hat{t}}{U\omega}\left(\int_\Sigma\left(\hat{\nabla}\cdot\hat{\boldsymbol{\sigma}}^{\mathrm{f}}\right)\mathrm{d}\hat{\Gamma}-\hat{S}\hat{\ddot{\mathbf{d}}}\right),\end{aligned} \tag{A.2}$$

which is nondimensionalized as

$$\begin{Bmatrix}\delta t_1\\ \delta t_2\end{Bmatrix} = \frac{\Delta t}{\bar{\omega}}\left(\int_\Sigma \nabla\cdot\boldsymbol{\sigma}^{\mathrm{f}}\mathrm{d}\Gamma - S\ddot{\mathbf{d}}\right), \tag{A.3a}$$

it is trivial to nondimensionalize δt_θ using Eq. (A.3a) and $\Delta\hat{\mathbf{x}} = \Delta\mathbf{x}/D$ below

$$\delta t_\theta = \Delta x_1\delta t_2 - \Delta x_2\delta t_1. \tag{A.3b}$$

We derive the following relation for the velocity increment

$$\delta\mathbf{u} = \frac{\Delta t}{\rho^{\mathrm{f}} S}\int_\Sigma\left(\nabla\cdot\boldsymbol{\sigma}^{\mathrm{f}} - \omega\dot{\delta\mathbf{t}}\right)\mathrm{d}\Gamma = U\cdot\frac{\Delta\hat{t}}{\hat{S}}\int_\Sigma\left(\left(\hat{\nabla}\cdot\hat{\boldsymbol{\sigma}}^{\mathrm{f}}\right) - U\omega\dot{\hat{\delta\mathbf{t}}}\right)\mathrm{d}\hat{\Gamma}, \tag{A.4}$$

which is reduced to

$$\delta\mathbf{u} = \frac{\Delta t}{S}\int_\Sigma\left(\nabla\cdot\boldsymbol{\sigma}^{\mathrm{f}} - \bar{\omega}\dot{\delta\mathbf{t}}\right)\mathrm{d}\Gamma \approx \frac{\Delta t}{S}\int_\Sigma\nabla\cdot\boldsymbol{\sigma}^{\mathrm{f}}\mathrm{d}\Gamma. \tag{A.5}$$

Flexible–body case

The velocity is nondimensionalized by U while the Cauchy stress by $\rho^{\mathrm{f}}U^2$. Hence, the increment is formulated for the traction as follow

$$\begin{aligned}\delta\mathbf{t} &= \frac{\Delta t}{\omega}\left(\nabla\cdot\boldsymbol{\sigma}^{\mathrm{f}} - \rho^{\mathrm{f}}\ddot{\mathbf{d}}\right) = \rho^{\mathrm{f}} U\cdot\frac{\Delta\hat{t}}{\omega}\left(\left(\hat{\nabla}\cdot\hat{\boldsymbol{\sigma}}^{\mathrm{f}}\right) - \hat{\ddot{\mathbf{d}}}\right)\\ &= \rho^{\mathrm{f}} U^2\cdot\frac{\Delta t^*}{U\omega}\left(\left(\hat{\nabla}\cdot\hat{\boldsymbol{\sigma}}^{\mathrm{f}}\right) - \hat{\ddot{\mathbf{d}}}\right),\end{aligned} \tag{A.6}$$

which gives the dimensionless form

$$\delta \mathbf{t} = \frac{\Delta t}{\bar{\omega}} \left(\nabla \cdot \boldsymbol{\sigma}^{\mathrm{f}} - \ddot{\mathbf{d}} \right), \tag{A.7}$$

in which $\bar{\omega} = U\omega$.

Equally, the increment may be written for the velocity as follow

$$\delta \mathbf{u} = \frac{\Delta t}{\rho^{\mathrm{f}}} \left(\nabla \cdot \boldsymbol{\sigma}^{\mathrm{f}} - \omega \dot{\delta} \mathbf{t} \right) = U \cdot \Delta \hat{t} \left(\left(\hat{\nabla} \cdot \hat{\boldsymbol{\sigma}}^{\mathrm{f}} \right) - U\omega \dot{\hat{\delta}} \hat{\mathbf{t}} \right), \tag{A.8}$$

implying

$$\delta \mathbf{u} = \Delta t \left(\nabla \cdot \boldsymbol{\sigma}^{\mathrm{f}} - \bar{\omega} \dot{\delta} \mathbf{t} \right) \approx \Delta t \nabla \cdot \boldsymbol{\sigma}^{\mathrm{f}}. \tag{A.9}$$

Appendix B

Publication list

[1] He T, Yang J, Baniotopoulos C. Improving the CBS-based partitioned semi-implicit coupling algorithm for fluid–structure interaction. *International Journal for Numerical Methods in Fluids* 2018; 87(9):463–486.

[2] He T, Zhang K. An overview of the combined interface boundary condition method for fluid–structure interaction. *Archives of Computational Methods in Engineering* 2017; 24(4):891–934.

[3] He T. A CBS-based partitioned semi-implicit coupling scheme for fluid–structure interaction using MCIBC method. *Computer Methods in Applied Mechanics and Engineering* 2016; 298:252–278.

[4] He T, Zhang K. Combined interface boundary condition method for fluid–structure interaction: Some improvements and extensions. *Ocean Engineering* 2015; 109:243–255.